Rheology of twist-bend and ferroelectric nematic liquid crystals

A Thesis submitted for the award of the degree of

Doctor of Philosophy in Physics

by

M Praveen Kumar

16PHPH07

Supervisor: Prof. Surajit Dhara

School of Physics

University of Hyderabad

Hyderabad, India

May 2023

To

My Family

Declaration

I, **Mylapalli Praveen Kumar**, hereby declare that this thesis entitled **"Rheology of twist-bend and ferroelectric nematic liquid crystals "** submitted by me under the supervision of **Prof. Surajit Dhara**, School of Physics, University of Hyderabad, Hyderabad, is a bonafide research work and also free from plagiarism. I hereby declare that it has not been submitted previously in part or in full to this University or any other University or Institution for the award of any degree or diploma.

M. Praveen Kumar

(M Praveen Kumar)

Reg. No: 16PHPH07.

Date: 23/5/23

Place: Hyderabad

Certificate

This is to certify that the thesis entitled **"Rheology of twist-bend and ferroelectric nematic liquid crystals"** bearing Reg. No. 16PHPH07, in fulfilment of the requirements for the award of Doctor of Philosophy in Physics is a bonafide work carried out by her under my supervision and guidance.

This thesis is free from plagiarism and has not been submitted previously in part or in full to this University or any other University or Institution for the award of any degree or diploma. Further, the student has the following publications before the submission of the thesis for adjudication.

1. M. Praveen Kumar, P. Kula and Surajit Dhara, *Phys. Rev. Materials* **4**, 115601 (2020). Chapter-3.

2. M. Praveen Kumar, J. Karcz, P. Kula and Surajit Dhara, *Phys. Rev. Materials* **5**, 115605 (2021). Chapter-4.

3. M. Praveen Kumar, J. Karcz, P. Kula, S. Karmakar and Surajit Dhara, *Phys. Rev. Applied.* **19**, 044082 (2023). Chapter-5

4. M. Praveen Kumar, D. Venkata sai and Surajit Dhara, *Physical Review E* **93**, 062701 (2018). Chapter-6.

Further, the student has passed the following course towards the fulfilment of coursework required for Ph.D.

SN	Course Code	Name	Credits	Pass/Fail
1)	PY801	Advanced Quantum Mechanics	4	Pass
2)	PY60309	Advanced Mathematical Methods	4	Pass
3)	PY60305	Advanced Experimental Techniques	4	Pass
4)	PY601	Research Methodology	4	Pass

Sdhara

Prof.Surajit Dhara

Thesis Supervisor,

School Of Physics,

University of Hyderabad.

Hyderabad–500046

Dr. Surajit Dhara
Professor
School of Physics
University of Hyderabad
Hyderabad-500 046, INDIA.

23/5/2023

Dean.

School Of Physics,

University of Hyderabad.

DEAN
School of Physics
Uuiversity of Hyderabad
HYDERABAD - 500 046

Acknowledgement

It's my pleasure to express my sincere gratitude to the people who supported me during the course of my doctoral thesis.

Firstly, my deep gratitude goes to my thesis advisor, Prof. Surajit Dhara, for his enduring guidance. His insistence on excellency, discipline and sincerity always influenced me towards new research ideas. His care, motivation and kindness will be remembered forever.

I would like to thank my Ph.D. Doctoral Committee members, Prof. S. Srinath, Prof. B. V. R Tata and Dr. Y. Ramachandra Rao for their discussions and suggestions throughout my research work. I am also thankful to the collaborators Prof. P. Kula for providing the samples from time to time.

Further, I am grateful to the former Deans, Prof. Bindu A. Bambah, Prof. R. Singh, Prof. Shashu Bhai and present Dean, Prof. K.C. James Raju, for providing me with all the school-level facilities and also all the other faculty members of School of Physics for their valuable suggestions at appropriate times. I am thankful to the current staff Sudharshan, Shashikala, Mahesh, Dileep, Santhosh, Udhay and former staff T. Abraham, shailaja, Prasad, Deepika and all the non-teaching staffs for their help and support in the department. In addition, I thank UOH administrative sections. I thank the University of Hyderabad and UGC-JRF for their financial assistance during my PhD course. Overall I express my heartiest thanks to the School of Physics, University of Hyderabad, for giving me the opportunity to accomplish my PhD.

I am very much thankful to my seniors, Dr Rasmitha Sahoo and Dr J. Ananthaiah, for helping me to learn all the rheometry techniques. My earnest gratitude to all other seniors, Dr P. Sathyanarayana, Dr J. Ananthaiah Dr D. Venkata Sai, Dr Rasna, Dr K. P Zuhail, Dr. Rasi, and Dr. Junaid for their help and support during my research work. I earnestly thank Anton Paar service providers Pramod and Prabhakar for their assistance. I wish all the best to the juniors Devika, Abinash, Archana, Kamakya, Saikath, Anaswara, Bidisha and Project students Rizwana, hemanth. I en-

joyed their company. It was very nice to work with them. I sincerely thank Dr. Ravi Pujala, Dr. Dinesh Sahu, devika and Sharif. They guided me through hard times.

My heartiest thanks to B.Srinubabu, Ashish Joe, Archana Kumari, Sravani, Hemanth, Dr Pradeep Chakravarthi, Naveen, Banda and many others who gave moral support that helped me to overcome my hardest times in the University.

My heartiest thanks to my batch mates, Atasi ray, Vinod, Dinesh, Pooja and Kuntal they are always there for any support in the University.

Undoubtedly, I miss my mother and her unconditional love and support, I am indebted to my father, without whom reaching to this height would not have been impossible. I am very much grateful to my parents for giving freedom and helping me to fulfil all my desires at each and every step of my life. I feel blessed to have sister Pallavi, who has always believed in me and encouraged me to go on any adventure. I express my heartfelt thanks to my childhood teacher, Barathratna sir. I am thankful to all my University friends for their continuous love and care. I am thankful to all my other relatives and family members for their love.

Beyond everything, I am highly grateful to God, the omnipresent, for blessing me throughout my life.

Preface

Nematic liquid crystals (NLCs) exhibit long-range orientational but no positional order. Recently, some new nematic LCs with a nano and micro scale modulation of director such as twist-bend nematic (N_{TB}) and splay nematic (N_S) have been discovered. The N_{TB} phase was theoretically proposed by Dozov where the director exhibits a periodic twist and bend deformations as shown schematically in. The constituting molecules have two mesogenic dimers connected with an odd number of flexible alkane spacers. Although the molecules are achiral the director forms an oblique helicoid ($0 < \theta < \frac{\pi}{2}$) with a nanoscale periodicity, where θ is the tilt angle with respect to the director. The structure of this phase is very different from that of chiral nematic (cholesteric) LCs made of chiral molecules. The heliconical pitch (p) of the N_{TB} phase is of the order of a few molecular lengths ($\sim$ 10 nm) and can be regarded as "pseudolayers" without a true mass density wave, unlike smectics. Nontheless, the N_{TB} phase shows focal conic defects similar to the ordinary smectics.

The splay nematic is found to be a ferroelectric and is denoted as N_F. The idea that a nematic phase could be ferroelectric was first suggested by Max Born in 1916, and it was followed up decades later by Frank *et al.* , who discussed the consequence of polar order on elastic free energy density and showed that, in this case, the director lacked head-tail symmetry. But this phase remained unidentified. Only very recently did Nishikawa *et al.* report that a molecule having a $1,3-dioxane$ unit in the mesogenic core exhibits a polar arrangement of molecules, later Mandle *et al.* designed a family of rod-like molecules with a terminal nitro group and alkyloxy side group, which exhibit nonpolar nematic to polar nematic phase (N_F) transition. The molecules are wedge or pear-shaped because the NO_2 group at the terminal have a large axial dipole moment (11.3D) and exhibits spontaneous splay with a large spontaneous electric polarization **P**.

The N_{TB} phase shows pseudolayer structure, whereas the N_F phase has a splay structure with spontaneous polarization parallel to the director. The discovery of these phases has created immense interest because of the potential application and intriguing fundamental science. Although many studies have been reported, their

rheological properties remain unexplored. In this thesis, we mainly investigate the rheological properties of these new nematic phases.

This PhD thesis is composed of six chapters. Chapter 1 provides an introduction. Chapter 2 deals with the experimental setup and the remaining five chapters present the research work carried out.

The **first chapter** gives a brief introduction to different thermotropic liquid crystals (LCs), especially the new nematic phases, like N_{TB} and N_F. We also, discuss about different rheological properties and measuring methods.

In the **second chapter**, we discuss experimental techniques used in this thesis. We used Anton Paar strain-controlled rheometer (MCR-501), it has several attachments like rheomicroscopy, rheodielectric, megnetorheology, and rheo-sals. It has an inbuilt Peltier temperature controller with an accuracy of 0.1°C. Finally, we present the experimental procedure of cell preparation for measuring some physical properties.

In **third chapter**, we study the rheological properties of N_{TB} phase and compare the results with those of an ordinary SmA phase. Our results show that the structural rheology of N_{TB} phase is strikingly similar to that of the ordinary smectic LCs. Analysing the shear response and adapting a simplified physical model for rheology of defect-mediated lamellar systems, we measure the pseudolayer compression elastic constant B_{eff} of N_{TB} phase from the measurements of dynamic modulus $G^*(\omega)$. We find that B_{eff} of the N_{TB} phase increases with decreasing temperature, and it follows a temperature dependence, $B_{eff} \sim (T_{TB} - T)^2$ as predicted by the recent coarse-grained elastic theory. Thus our results provide a valuable test of the validity of the proposed theoretical models. This experiment also offer perspectives on N_{TB} LCs and opens unexplored aspects of the rheology of nematic LCs with nanoscale modulation of director.

The **fourth chapter** focuses on the study of shear dynamics of a twist-bend nematic (N_{TB}) liquid crystal. The chemical structure and phase transition temperatures are shown in. We measure shear stress (σ) as a function of shear rate ($\dot{\gamma}$) at different temperatures. It shows three distinct shear stress (σ) responses in a certain

range of temperature and shear rate ($\dot{\gamma}$). In Region-I, $\sigma \sim \sqrt{\dot{\gamma}}$, in region-II, the stress shows a plateau, characterised by a power law $\sigma \sim \dot{\gamma}^{\alpha}$, where $\alpha \sim 0.1 - 0.4$ and in region-III, $\sigma \sim \dot{\gamma}$. With increasing shear rate, σ changes continuously from region-I to II, whereas it changes discontinuously with a hysteresis from region-II to III. In the plateau (region-II), we observe a dynamic stress fluctuations, exhibiting regular, periodic and quasiperiodic oscillations under the application of steady shear. It appears that with increasing temperature, our system moves from a regular periodic to quasiperiodic state. Our experiments show some striking similarities with the dynamic stress response of nematogenic fluids predicted recently. Our study unveils the flow dynamics of twist-bend nematic liquid crystals, which are promising for further experimental and theoretical studies

In the **fifth chapter**, we study the electroviscous effects which deals with the change in the viscosity of fluids due to the external electric field. Here, we report experimental studies on the electroviscous effects in a ferroelectric nematic liquid crystal. We measure electric field-dependent viscosity under a steady shear rate at different temperatures. In the low field range, the increase in viscosity ($\Delta\eta$) is proportional to E^2 and the corresponding viscoelectric coefficient (f) is two orders of magnitude larger in ferroelectric nematic than the conventional nonpolar nematic liquid crystals. The apparent viscosity measured under high electric field shows a power-law divergence $\eta \sim (T - T_c)^{-0.7\pm0.05}$, followed by a drastic decrease below the $N - N_F$ phase transition temperature. Experimental results within the dynamical scaling approximation demonstrate rapid growth of elongated polar domains under applied electric field which suppresses the $N - N_F$ phase transition temperature significantly. We envisage that pretransitional growth of polar domains and their dynamic response should be manifested in many other measurements. These new results should be of interest for most of the physical as well as electrooptical studies on ferroelectric nematic LCs which involve electric fields.

In the **sixth chapter**, we study temperature-dependent translational and rotational viscosities of a few nematic liquid crystals made of highly polar molecules. Cyanobiphenyl (nCB) with logitudinal and cyanobicyclohexane molecules (CCN-mn) with transverse dipole moments were chosen and the measurements were made in the

nematic phase. The translational viscosity (shear viscosity) is measured by using a rheometer and the rotational viscosity is measured from the dynamics of the Freedericksz transition by measuring the optical phase-retardation decay of the sample. The associated activation energies are obtained from the fitting of the Arrhenius equation in the nematic phase. Only 8CB and CCN-47 exhibits N to SmA phase transition and their activation energies of translational and rotational viscosities are larger compared to the shortest homologs in the respective series. Both activation energies of 8CB are significantly larger than that of CCN-47. The temperature-dependent steady states of the director distribution under shear are comprehensibly reflected in the rheodielectric measurements of 8CB than that of CCN-47. The results are explained based on the differences in the SmA short-range orders and the critical slowing down of the order parameter fluctuations. We present a simple physical model of molecular association that gives rise to different SmA short-range orders in both classes of compounds. We emphasize that, rheodielectric experiments are very useful to probe the effect of smectic short-range order and critical slowing down of the SmA order parameter fluctuation as the N-SmA transition is approached in highly polar compounds with both longitudinal and transverse dipole moments. Such studies also have important relevancy on our understanding of the phase transitions in liquid crystals away from equilibrium.

Contents

List of Abbreviations and Symbols

MCR	:	Modular compact rheometer
CP	:	Cone-and-plate
PP	:	Parallel-plate
σ	:	Shear stress
γ	:	Strain
$\dot{\gamma}$	:	Shear rate
G	:	Shear modulus
G_o	:	Plateau modulus
η	:	Shear viscosity
G^*	:	Complex modulus
G'	:	Storage modulus
G''	:	Loss modulus
η'	:	Dynamic viscosity
ω	:	Angular frequency
q	:	Scattering vector
λ	:	Wavelength
θ	:	Scattering angle
I	:	Intensity
N	:	Nematic Phase
SmA	:	Smectic-A phase
SmC	:	Smectic-C phase
N^*	:	Cholesteric phase
$\mathrm{N_{TB}}$	:	Nematic Twist Bend Phase

N_F	:	Ferroelectric nematic Phase
$\hat{n}$	:	Liquid Crystal Director
ψ	:	Smectic order parameter
ITO	:	Indium tin oxide
$\epsilon_{\|\|}$	:	Dielectric constant parallel to $\hat{n}$
$\epsilon_{\perp}$	:	Dielectric constant perpendicular to $\hat{n}$
$\Delta\epsilon$=$\epsilon_{\|\|} - \epsilon_{\perp}$	:	Dielectric anisotropy
K_{11}, K_{22}, K_{33}	:	Splay, twist and bend elastic constant
γ_1	:	Rotational viscosity
η_1, η_2, η_3	:	Miesowicz viscosity coefficients
$\alpha_1.....\alpha_6$	:	Leslie coefficients
T_{NI}	:	Nematic-isotropic phase transition temperature

1

Introduction

1.1 Abstract

Soft condensed matter are ubiquitous in our daily life. The size of the molecules in soft materials are mostly midway between atomic and microscopic scales. Even though they are larger than atomic size brownian motion occurs in them. They create self-assembling systems by balancing of energy and entropy, which takes place at the level of molecules to reach equilibrium. They can be easily deformed by applying small external forces. This thesis focuses on the rheology of a special class of soft matter called liquid crystals (LC), whose properties lies between solids and liquids. Liquid crystals are responsive to external electric and magnetic fields and hence exhibit electro-optic effects which are exploited in liquid crystal displays.

1.2 Overview

The traditional condensed matter are solids, whereas "soft condensed matter" like glue, soap, tomato ketchup, gel, paste, liquid crystal, paints etc., are neither solid nor liquid. They show a complex visco-elastic response under external forces. First, we discuss rheological measurements such as oscillatory and rotational tests of soft materials. Thereafter we discuss some theoretical models to characterize their flow behaviour. Then, we briefly introduce liquid crystals and some phases, including two new nematic phases such as nematic-twist bend (N_{TB}) and ferroelectric nematic (N_F) phases which show pseudolayer structure, and spontaneous polarization (P), respectively. The discovery of these phases particularly the ferroelectric nematic has created

immense interest because of the potential application and intriguing fundamental science. Although many studies have been reported on these two phases, their rheological properties are yet unexplored. This thesis mainly reports on the rheological properties of above mentioned new nematic phases. Before we discuss the actual experiments we introduce some physical properties of liquid crystals like dielectric, elastic, electro-optic and viscosity which are relevant to the subsequent chapters.

1.3 Rheology

Rheology originates from the Greek word: "rheos" means "streaming" and "logy" means "science". Thus, rheology deals with the science of flow. In general rheological properties reveal the hardness or softness of a material, indicating its fluid-like or solid-like character. The rheological properties of complex fluids are measured through a rheometer as a function of rate or frequency of deformation. The storage, loss moduli and shear viscosity are important parameters to characterise the visco-elastic properties of soft materials. Several standard tests like creep test, relaxation test, oscillatory and rotational tests are performed to investigate mechanical behaviour. Generally, all fluids are categorized into two: namely, Newtonian and non-Newtonian. Newtonian fluids are simple fluids where stress (σ) is proportional to the shear rate ($\dot{\gamma}$) and are given by

$$\sigma = \eta\dot{\gamma} \tag{1.1}$$

where η is the viscosity. Fluids which doesn't follow the above equation are called non-Newtonian fluids.

1.3.1 Viscoelastic materials

The materials whose properties are neither classical materials like solids nor liquids are called viscoelastic materials. They show both elastic and viscous properties., e.g. food materials, polymers, biological tissues, blood, oils, creams, rubber, pastes, ketchup, liquid crystals etc. Their properties depend largely on the rate of deformation or frequency. When the stress is applied to these materials, they will deform and do not revert to their original state even after the removal of the applied stress. They exhibit

solid-like behavior below some frequency. At higher frequencies, mostly they exhibit liquid-like behavior. They store and dissipate a part of supplied energy. Viscoelastic fluids are characterized by the complex shear modulus $G^*(\omega) = G^{'}(\omega) + iG^{''}(\omega)$, the real part ($G^{'}$), signifies as energy storage and the imaginary part ($G^{''}$) as energy loss.

1.3.2 Viscoelastic model

The viscoelastic response can be described by adapting appropriate models, which consists of two components, one describes the elastic part represented by a spring and the other describes viscous behavior represented by a dashpot as shown in Fig. 1.1. These components can be combined in many ways to develop the constitutive

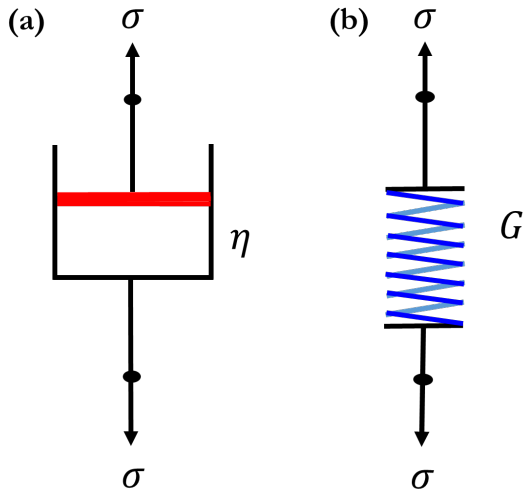

Figure 1.1: (a) A dashpot: mechanical analog to liquid behavior (b) A spring: mechanical analog to elastic behavior.

equations for viscoelastic materials. One such model is Maxwell's model [1].

1.3.2.1 Maxwell Model

In this simple model (Fig.1.2), the stress for both the dashpot and the spring is considered to be the same ($\sigma_s = \sigma_v = \sigma$). The deformation (strain) of the Maxwell model is equal to the sum of the individual deformations of the spring and dashpot. i.e., $\gamma = \gamma_s + \gamma_d$ where γ_s and γ_d represents the strain in spring and dashpot, respectively. By considering the time derivative of strain. we can write

$$\dot{\gamma} = \dot{\gamma_s} + \dot{\gamma_d} \tag{1.2}$$

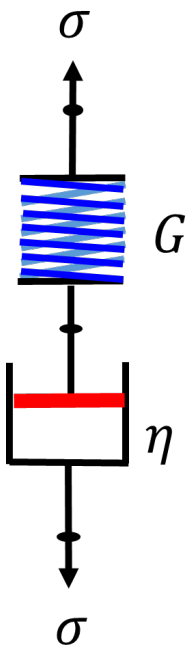

Figure 1.2: Maxwell model of mechanical analog consists of a spring and a dashpot connected in series.

For Hookean solids we expect ideal elastic response in which shear stress is proportional to the shear strain.

$$\sigma = G\gamma, \tag{1.3}$$

where G is the storage modulus. Similarly, for ideal Newtonian fluids shear stress is proportional to the shear rate hence

$$\sigma = \eta\dot{\gamma} \tag{1.4}$$

where η is the viscosity.

By substituting Eq.1.3 and Eq.1.4 in Eq.1.2 we get

$$\dot{\gamma} = \frac{\dot{\sigma}}{G} + \frac{\sigma}{\eta} \tag{1.5}$$

or

$$\eta\dot{\gamma} = \frac{\eta}{G}\dot{\sigma} + \sigma \tag{1.6}$$

This standard representation of the Maxwell model shows the relationship between stress and strain as an ordinary differential equation (Eq.1.6). By solving the above differential equation we get,

$$\sigma = \eta\dot{\gamma}\left[1 - \exp\left(\frac{-t}{\tau_M}\right)\right] \tag{1.7}$$

where $\tau_M = \eta/G$ is the Maxwell relaxation time.

1.3.2.2 Kelvin-Voigt model

There are other models like **Kelvin-Voigt** model for viscoelastic materials where dashpot and spring are connected in parallel as shown in Fig.1.3. However, in this model strain in the spring and dashpot are same, $(\gamma = \gamma_s = \gamma_d)$, whereas stresses are

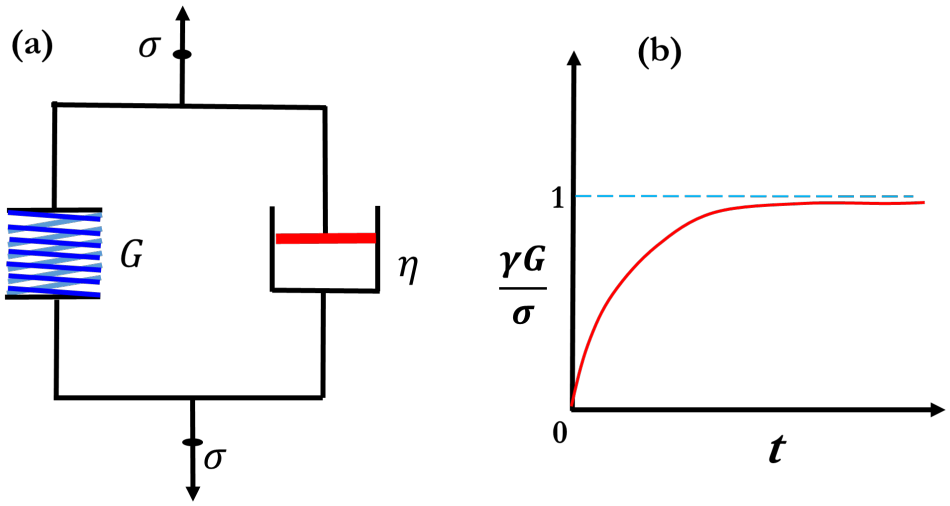

Figure 1.3: (a) Kelvin-Voigt model of mechanical analog consists of a spring and a dashpot connected in parallel. (b) Growth of strain with time in Kelvin-Voigt model

additive, i.e.,

$$\sigma = \sigma_s + \sigma_d \tag{1.8}$$

By substituting Eq.1.3, and Eq.1.4 in the above equation. we get,

$$\sigma = G\gamma + \eta\dot{\gamma} \tag{1.9}$$

i.e,

$$\frac{\sigma}{G} = \gamma + \frac{\eta}{G}\dot{\gamma} \tag{1.10}$$

The above equation is known as the Kelvin-Voigt equation. By solving the above differential equation we get,

$$\gamma = \frac{\sigma}{G}\left[1 - \exp\left(\frac{-t}{\tau_K}\right)\right] \tag{1.11}$$

where $\tau_K = \eta/G$ is called Kelvin retardation time. It characterises the retarded response to the material as shown in Fig.1.3(b).

There are other complex models (Burgers, standard linear solid model etc) which are the combination of these two models.

1.3.3 Linear Oscillatory measurements

Oscillatory tests are done to examine all kinds of viscoelastic materials. They are useful for characterizing structures. Generally, two important measurements are performed under oscillatory test, namely, amplitude sweep and frequency sweep.

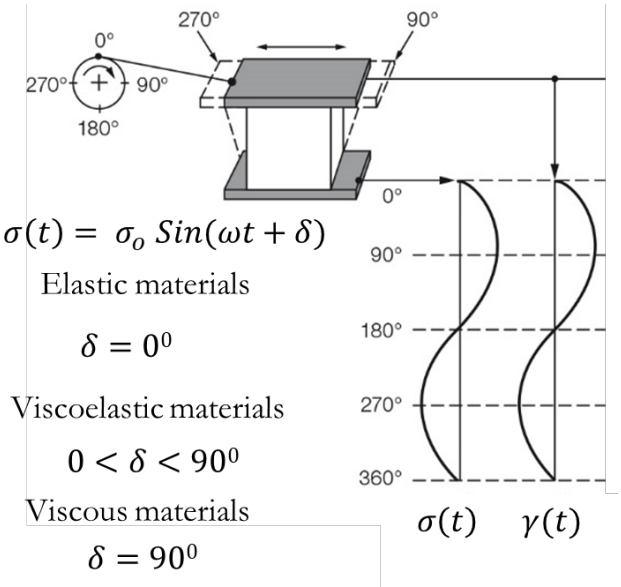

Figure 1.4: Oscillatory test with the two-plates model, the time-dependent sine curves of the preset shear strain $\gamma(t)$ and the resulting shear stress $\sigma(t) = \sigma_o \sin(\omega t + \delta)$. For ideal elastic behavior $\gamma(t) \propto \sigma(t)$ that is δ =0° whereas for viscoelastic materials δ is in between 0 to 90° as there is a time lag between the $\gamma(t)$ and $\sigma(t)$ whereas for ideally viscous fluids $\delta = 90°$.

To explain, we use a two-plate model here. The oscillation of the upper plate is

produced by a turning wheel on which the lower plate is stationary, whereas the upper plate moves back and forth, driven by a wheel with an eccentrically mounted push rod. As shown in Fig.1.4, at 90° and 270° deflections, the upper plate reaches its maximum amplitude. The torque required to move the upper plate divided by the area of the plate results in the applied shear stress (σ). The rate of structural rearrangement within a complex fluid can be understood by applying a small-amplitude oscillatory shearing on the material. This kind of deformation can be performed by the oscillatory test in the rheometer.

The underlying principle of an oscillatory test is to induce a sinusoidal shear deformation in the sample, called strain and measure the corresponding storage ($G^{'}(\omega)$) and loss moduli ($G^{''}(\omega)$). Here ω is the frequency of oscillation. In our experiments, the bottom plate is stationary and the top plate is movable. The top plate provides a time-dependent strain (sinusoidal strain) to the sample, and it can be defined as:

$$\gamma(t) = \gamma_o \sin(\omega t) \tag{1.12}$$

where γ_o is the strain amplitude. So, for an ideal elastic material, the shear stress is always in phase with respect to the applied shear strain. In contrast, if a material is a purely viscous fluid, the applied shear strain and measured stress are out of phase with a phase angle $\delta = \pi/2$. For a visco-elastic material, the shear deformation and stress show both in-phase and out-phase components. So the shear stress can be defined as [42]:

$$\sigma(t) = \sigma_o \sin(\omega t + \delta) \tag{1.13}$$

where σ_o is the shear stress amplitude and δ is the phase lag. Hence, the time-dependent shear stress ($\sigma(t)$) can be determined simultaneously from the measured torque that the sample imposes on the top plate. This time-dependent stress response, at a constant angular frequency provides the elastic response of the materials. For harmonic strain $\gamma(t) = \gamma_o e^{i\omega t}$, and the stress becomes $\sigma(t) = \sigma_o e^{i\omega(t+\delta)}$ where ω is the angular frequency and δ is the phase angle between the applied strain and the resulting stress can be written as [4]

$$\sigma(t) = \left(\frac{G\eta^2\omega^2 + iG^2\omega\eta}{G^2 + \omega^2\eta^2} \right) \cdot \gamma(t) \tag{1.14}$$

where τ is the relaxation time. The above equation can be expressed as

$$\sigma(t) = \left(\frac{\eta\tau\omega^2}{1+(\omega\tau)^2} + i\frac{\omega\eta}{1+(\omega\tau)^2} \right) \cdot \gamma(t) \tag{1.15}$$

or

$$\sigma(t) = G^*(\omega) \cdot \gamma(t) \tag{1.16}$$

where G^* is the complex shear modulus, which can be written as

$$G^* = G^{'} + iG^{''} \tag{1.17}$$

Here G^* signifies the overall shear modulus, which resists the deformation of the complex fluid under applied shear strain. The real and imaginary components are given by [9]

$$G'(\omega) = \frac{\eta\tau\omega^2}{1+(\omega\tau)^2} \tag{1.18}$$

$$G''(\omega) = \frac{\omega\eta}{1+(\omega\tau)^2} \tag{1.19}$$

1.3.3.1 Frequency sweep

The angular frequency dependent $G^{'}$ and $G^{''}$ are measured at a constant shear strain in the frequency sweep measurement. This experiment is performed to study the dynamic behaviour of the materials. The visco-elastic behaviour of the system can be characterised by the storage modulus ($G^{'}$) and the loss modulus ($G^{''}$), which signifies solid-like and fluid-like behaviour to the measured stress. For $\omega\tau \ll 1$, in the above Equations (Eq.1.18 and Eq.1.19) gives $G^{'} \propto \omega^2$ and $G^{''} \propto \omega$, then it shows a Maxwell-fluid like behavior. If $G^{'}$, $G^{''} \propto \omega$, then it is called a soft-glass behavior [43]. At low frequency if $G^{'} > G^{''}$, the material shows a gel-like behavior.

For a sinusoidal shear deformation, the shear stress response of a visco-elastic material can be expanded as:

$$\sigma(t) = G^{'}(\omega)\gamma_o \sin(\omega t) + G^{''}(\omega)\gamma_o \cos(\omega t) \tag{1.20}$$

where

$$G^{'} = \frac{\sigma_o}{\gamma_o}\cos\delta, \quad G^{''} = \frac{\sigma_o}{\gamma_o}\sin\delta \tag{1.21}$$

The ratio of G''/G' gives $\tan(\delta)$ and is called the loss tangent. The fluid characteristics can be determined from this $\tan(\delta)$ value. If $G' > G''$, and $\tan(\delta) << 1$, then the elastic behaviour dominates over the viscous behaviour signifying a solid-like response. If G'' $> G'$ and $\tan(\delta) >> 1$, then the viscous behaviour dominates over the elastic behaviour indicating a liquid-like response.

1.3.3.2 Amplitude sweep

In the amplitude sweep measurement, the strain-dependent G' and G'' are measured at a constant angular frequency ω. The region up to which both G' and G'' remain constant with applied shear strain is called the "linear visco-elastic" (LVE) range. Beyond this range, both the shear moduli start decreasing and usually show a crossover called strain-induced yielding or the critical strain (γ_c), above which the fluidization occurs.

1.3.4 Rotational measurements

Rotational measurements are performed to characterize the flow behaviour of the sample. Mainly, three types of steady-state flow behaviour observed. These are called Newtonian, shear thinning and shear thickening behaviours. If the viscosity remains constant with the shear rate, it is called Newtonian flow behaviour. If the viscosity decreases with increasing shear rate, it is called shear-thinning flow behaviour. If the viscosity increases with increasing shear rate, it is called shear-thickening flow behaviour. Fig.1.5 shows these three different types of the flow behaviour of fluids schematically.

There are different "power-law" models to characterise the flow behaviours of the complex fluids. One of the popular models is the Sisko model. In the Sisko model, the viscosity η varies as [9]

$$\eta = \eta_\infty + K\dot{\gamma}^{n-1} \tag{1.22}$$

where n is called the power-law index, K is called the "consistency".

The flow curve of viscoelastic fluids exhibits Newtonian behavior above the yield stress σ_y, called a Bingham plastic fluid. According to this definition, the model of

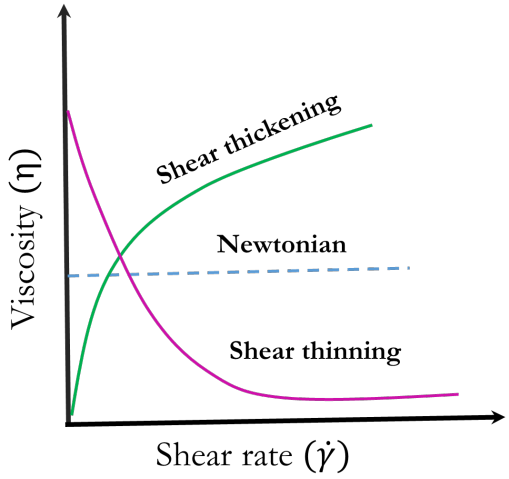

Figure 1.5: Typical variation of viscosity as a function of shear rate, as magenta, dotted blue and green lines indicate shear thinning, Newtonian, and shear thickening flow behaviours, respectively.

Bingham plastic flow behavior can be formulated by the following equation [2]:

$$\sigma = \sigma_y + \eta_p \dot{\gamma} \tag{1.23}$$

where η_p is called plastic viscosity. Viscoelastic fluid often exhibits non-Newtonian behaviour above the yield stress and such flow behaviour can be explained by Herschel Bulkley (HB) model given by the equation:

$$\sigma = \sigma_y + \eta_{(HB)} \dot{\gamma}^p \tag{1.24}$$

where σ_y is the yield stress and $\eta_{(HB)}$ indicates the flow coefficient, also called Herschel-Bulkley viscosity and the exponent p is called the HB index. For $p = 1$ HB equation becomes a linear equation called the "Bingham plastic". The Bingham equation signifies the yield stress of materials at a low shear rate region, whereas the Sisko model explains the viscosity response in the low and high shear rate range of a flow curve.

1.4 Liquid Crystals

In 1888, Austrian botanist Friedrich Reinitzer unexpectedly observed “two melting points” in cholesteryl benzoate, and later Otto Lehmann studied these phases and

named 'liquid crystal' [5,6]. The substance is strongly anisotropic in some of its properties yet exhibits a certain degree of fluidity. The molecules in this state exhibit a long-range orientational order Fig.1.6. They have characteristics of liquids, such as viscosity, surface tension etc. On the otherhand they display solid-like characteristics such as anisotropy in optical (birefringence), electrical (dielectric), magnetic (diamagnetic susceptibility), and other elastic properties. [7,22]. They are very useful in creating low-power displays and tunable optical devices since most of their physical features are tunable by external fields. Liquid crystals can be broadly distinguished as thermotropic and lyotropic. The lyotropic liquid crystals are temperature and concentration dependent, whereas the thermotropic liquid crystals are only temperature dependent. There are some compounds which exhibit both lyotropic and thermotropic phases known as amphotropic liquid crystals [8].

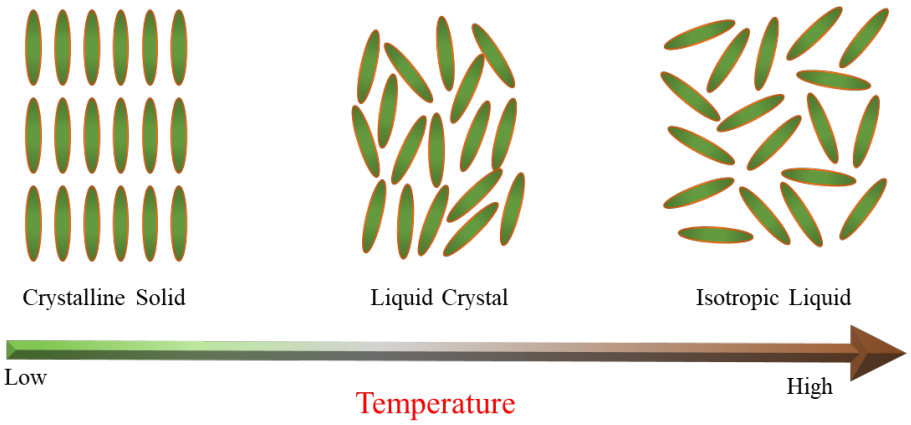

Figure 1.6: Schematic diagram of three different states of liquid crystal as a function of temperature.

Thermotropic liquid crystals are of three categories, depending on the shape of the constituent molecules. They are known as (i) calamatic (consists of rod-like molecules), (ii) bent-core (consists of bent-shaped molecules) and (iii) discotic (consists of disc-like molecules) as shown in Fig.1.7. This section discusses some phases exhibited by rod-shaped molecules.

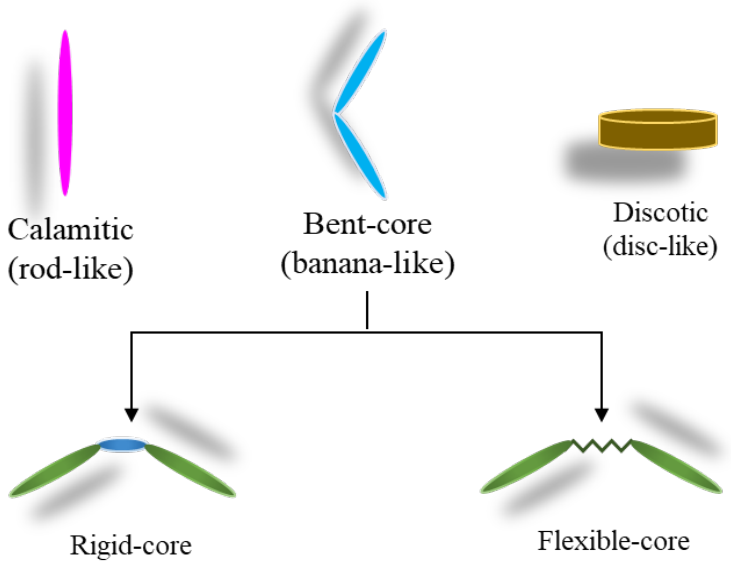

Figure 1.7: Different shapes of the liquid crystal molecules.

1.4.1 Nematic phase (N)

The nematic liquid phase is the simplest phase among all LC phases with only long-range orientational order, where the molecules are spontaneously oriented parallel to their long axes. The average alignment direction of the long molecular axes is called the director ($\hat{n}$). The director $\hat{n}$ and -$\hat{n}$ are physically identical, and the director is said to be apolar in nature. The nematic phase is uniaxial because its rotational symmetry along the director. A schematic diagram of the nematic phase is shown in Fig.1.8(a)

1.4.1.1 Order parameter of nematic

An order parameter measures how much a system changes in order across the phase transitions. The ensemble average of second Legendre polynomial gives the scalar order parameter S that expresses the degree of orientational ordering of the molecules and expressed as [7]

$$S = \langle P_2(cos\theta) \rangle = \frac{1}{2} \left\langle 3cos^2\theta - 1 \right\rangle \tag{1.25}$$

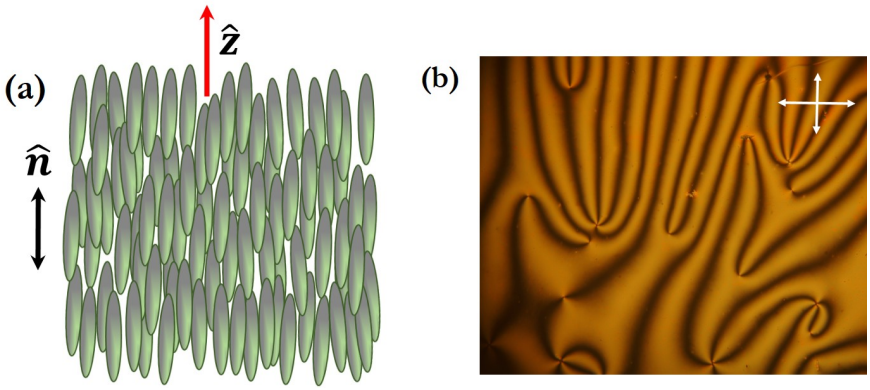

Figure 1.8: Schematic representation of nematic phase, $\hat{n}$ signifies the director of the rod-shaped molecules. (b) Schlieren texture of a nematic phase under crossed polarizing optical microscope (POM).

where $\langle..\rangle$ indicates the ensemble average of the molecules. In general for uniaxial nematic, the order parameter is a second-rank tensor due to the apolar nature and it can be written as

$$S_{\alpha\beta}(\bar{r}) = S(n_\alpha(\bar{r})n_\beta(\bar{r})) - \frac{1}{2}\delta_{\alpha\beta} \tag{1.26}$$

where the term $n_\alpha(\bar{r})n_\beta(\bar{r})$ illustrates the spatial variation of $n(\bar{r})$ and S is the scalar order parameter as defined by Eq.(1.25). Theoretically, S varies from 0 (isotropic phase) to 1 (ordered phase). Experimentally, S ranges from 0.3 at the N-I transition to 0.8 at lower temperatures [7].

1.4.1.2 Cholesteric phase (N*)

The nematic structure spontaneously develops a twist or a helix when chiral dopants are added to the nematic or if the molecules are chiral by nature. Locally, the cholesteric phase is nearer to the nematic phase, but the director $\hat{n}$ rotates helically because of the chirality of the molecules (Fig.1.9). A chiral pitch p is produced, in which the liquid crystal molecules rotate at an angle of 360°. The director rotates 0°-180° as $\hat{n}$ and then 180°- 360° as $-\hat{n}$ are equivalent. The pitch usually changes when the temperature is changed. The cholesteric director field $(\hat{n}(r))$ can be expressed

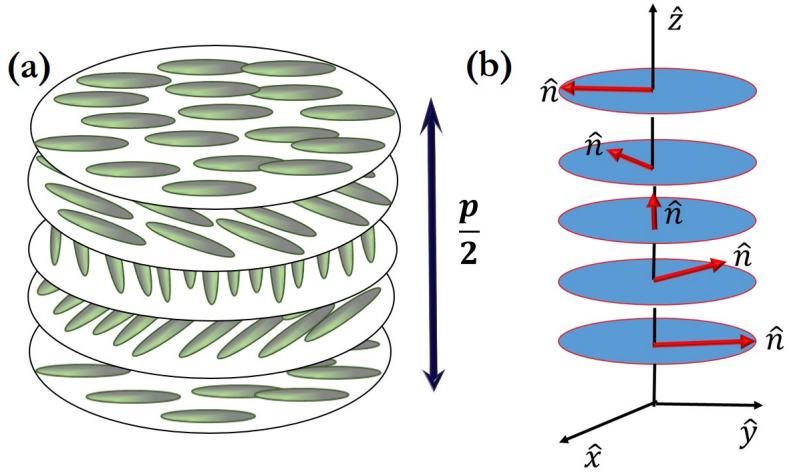

Figure 1.9: (a) Schematic representation of the molecular arrangement in the cholesteric phase where $p/2$ indicate half-pitch length. (b) rotation of director $\hat{n}$ in a helical manner making angle 90° with respect to the z-axis.

as [11]

$$\begin{aligned} \hat{n}_x &= cos\left(\frac{2\pi}{p}z + \phi\right), \\ \hat{n}_y &= sin\left(\frac{2\pi}{p}z + \phi\right), \\ \hat{n}_z &= 0 \end{aligned} \tag{1.27}$$

where ϕ is a constant which depends on the boundary conditions. The pitch of the cholesteric LCs can vary in wide ranges, from a few hundred nanometres to a few tens of micrometres. The chirality of handedness is either left or right. N* phase appears quite differently from the uniaxial N phase in terms of its textural features. The most commonly observed feature for the N* phase are oily streaks, fan-like and fingerprint textures. Some of the textures and corresponding molecular orientations are shown in Fig.1.10.

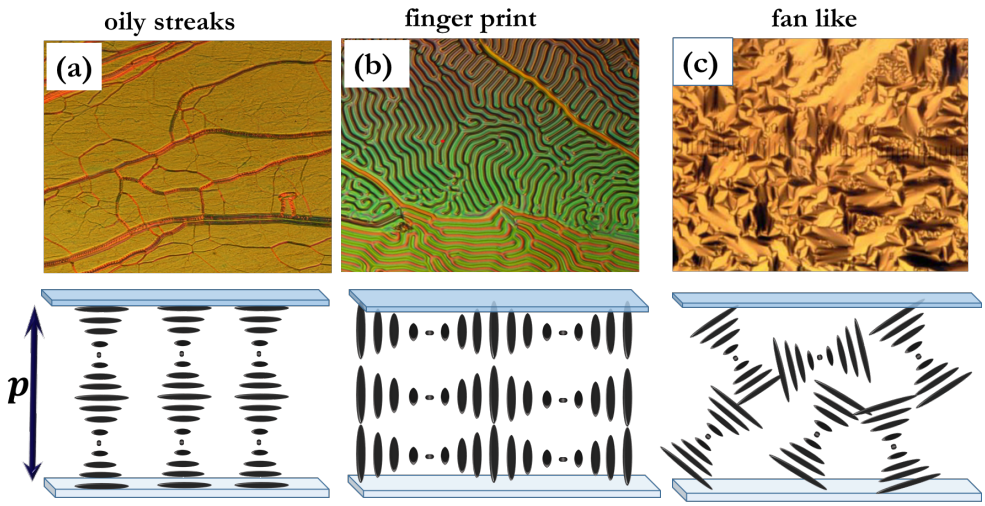

Figure 1.10: (a, b, c) Different cholesteric textures under crossed polarizer and their corresponding director orientation (underneath).

1.4.2 Smectic phases

The molecules in the smectic phases also have a positional order in addition to their orientational order. Here, the positional order refers to the layer structure arranged by the molecules. Though the molecules are stacked in layers, their centres of mass are randomly distributed like liquids. Depending upon the orientation of the director with respect to the layer normal we can get different phases like Smectic-A (SmA), Smectic-C (SmC), and Smectic-C* (SmC*) etc.

Among all smectic phases, Smectic-A is the least ordered layered phase. The average alignment of the molecules in each layer is in the direction of layer normal as shown in Fig.1.11. Typically, the spacing between layers in the smectic-A phase is comparable to the molecular length. There is no long-range correlation of the centre of mass of the molecules in the smectic layers, and they behave like a two-dimensional fluid. The layers can slide over each other, and the diffusion of molecules from one layer to another is possible. The SmA phase is typically uniaxial and positive. While mass density ρ in nematics is constant (Fig.1.12(a)), for SmA it is sinusoidal as represented by Eq.(1.28). In SmA, it becomes a periodic function of the coordinate z normal to

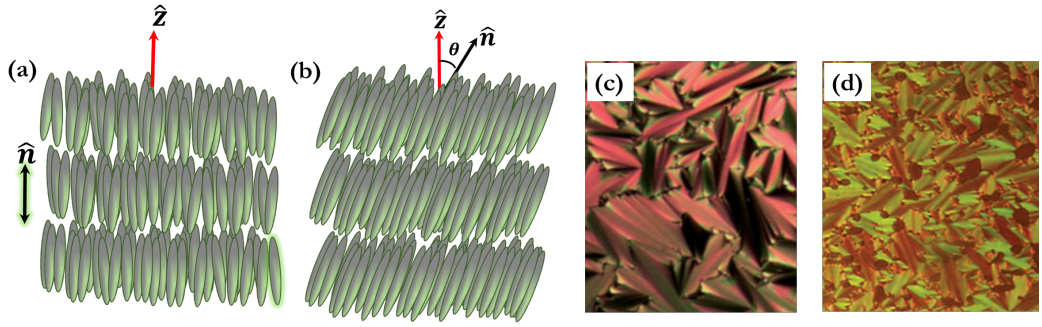

Figure 1.11: Schematic representation of molecular orientation in (a) SmA and (b) SmC phase where $\hat{n}$ and $\hat{z}$ are the director and layer normal, respectively. (c) Focal conic texture of SmA (d) Broken fan-like structure of SmC phase under crossed POM. (Adapted from [12, 13])

.

smectic layers (Fig.1.12(b)) and the density can be expressed as

$$\rho(z) = \rho(z + l) \tag{1.28}$$

where l is the distance between layers. One can decompose Eq.(1.28) into the Fourier series by the cos-functions up to the second-order term.

$$\rho(z) = \rho_0 + |\Psi| \cos(qz) \tag{1.29}$$

Here ρ_o, is the mean density, $|\Psi|$ is the density wave amplitude in smA, $q = \frac{2\pi}{\lambda}$ is the wave number, $|\Psi| \neq 0$ for SmA, while $|\Psi| = 0$ for nematic phase.

In smectic-C (SmC) phase, the layer normal $\hat{z}$ makes an angle θ with the molecular long axis as shown in Fig.1.11(b). Usually, this tilt angle decreases with increase in temperature across the SmA-SmC phase transition. Some typical texture of SmA and SmC phase are shown in Fig.1.11(c) and Fig.1.11(d); respectively.

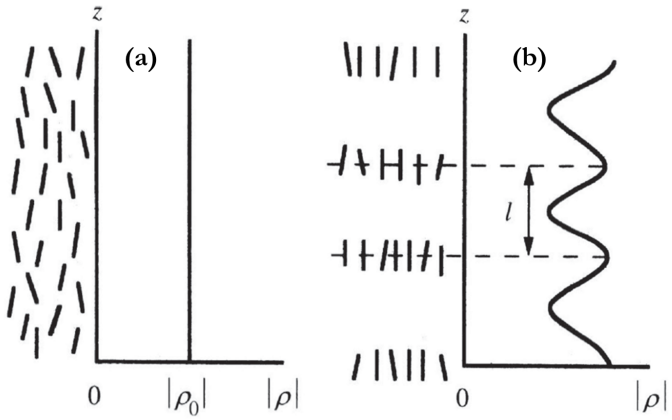

Figure 1.12: Mass density $\rho(z)$ modulation in nematic and SmA phases. (a) In the nematic phase the density ρ is constant whereas, (b) in SmA, the periodic modulation of ρ along the $\hat{z}$ direction indicates layer occurrences. (Adapted from Ref. [14]).

1.4.3 Twist bend nematic phase (N_{TB})

In 2001 Ivan Dozov proposed a new nematic phase of banana-shaped molecules, assuming bend elastic constant (K_{33}) can become negative [16]. He theoretically showed that these bend molecule's ground state is no longer uniform like nematic. It forms either splay-bend deformation or a conical twist-bend helix as shown in Fig.1.13. The local nematic symmetry is broken in both cases and the phase becomes polar. Meyer made a similar prediction long ago, suggesting that polar interaction favour bend deformation that might lead to a twist-bend nematic phase [17]. In this phase the director draws an oblique helicoid, maintaining a constant oblique angle $0 < \theta < \frac{\pi}{2}$ with the helix axis $\hat{z}$. The twist is right-handed or left-handed, depending on molecular chirality. A 3D director field highlighting the differences among N, N_{TB}, and N* phases are shown in (Fig.1.14) Later, in the experiments some unusual nematic phase was observed in some compounds which was named as N_X phase [15]. The optical structures of this phase showed focal conic domains like smectics (Fig.1.15). But through XRD diffraction, no true mass density wave was detected which excluded the possibility of SmA phase. Later, other experimental evidences like freeze-fracture transmission electron microscopy (FFTEM) as shown in Fig.1.16 and most recently by resonant X-ray scattering [15, 21, 31] confirms that the N_X phase is a nematic twist bend phase. A helix

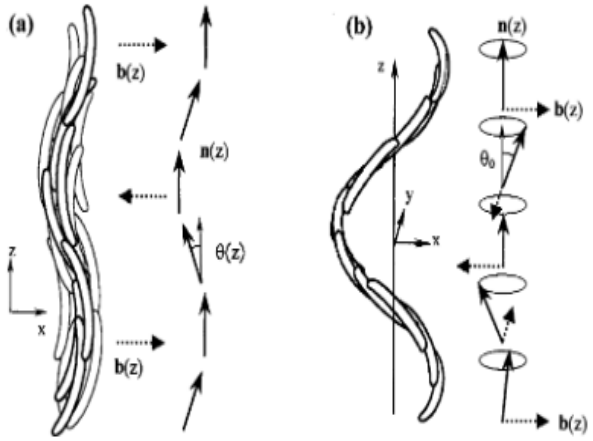

Figure 1.13: Schematic representation of spontaneously modulated splay-bend nematic phase. (b) Conical twist-bend helix with constant angle θ_0 where $\bar{b} = \hat{n} \times (\nabla \times \hat{n})$ (Adapted from Ref. [16]).

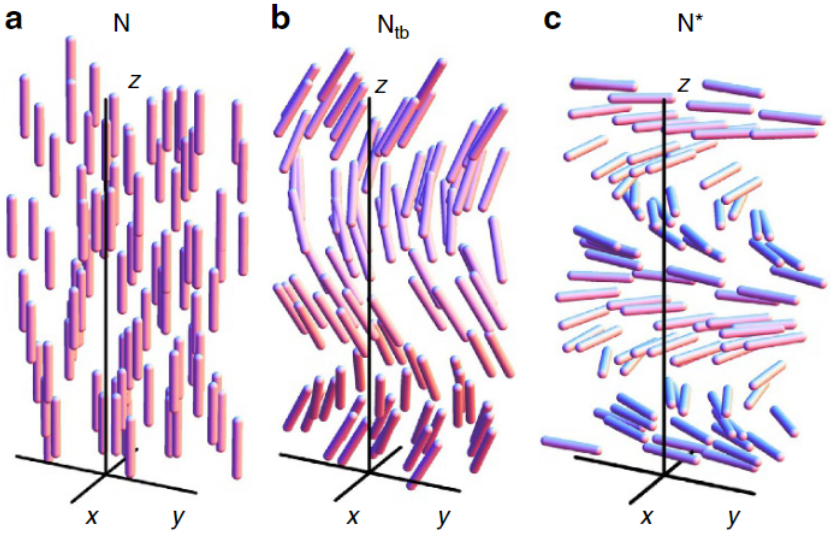

Figure 1.14: Schematic diagram of local director orientation in (a) uniaxial nematic phase, $\theta_0 = 0$, (b) N_{TB} phase with heliconical angle $0 < \theta < \frac{\pi}{2}$, and (c) N* phase with right chirality θ_0= 90° (Adapted from Ref. [15]).

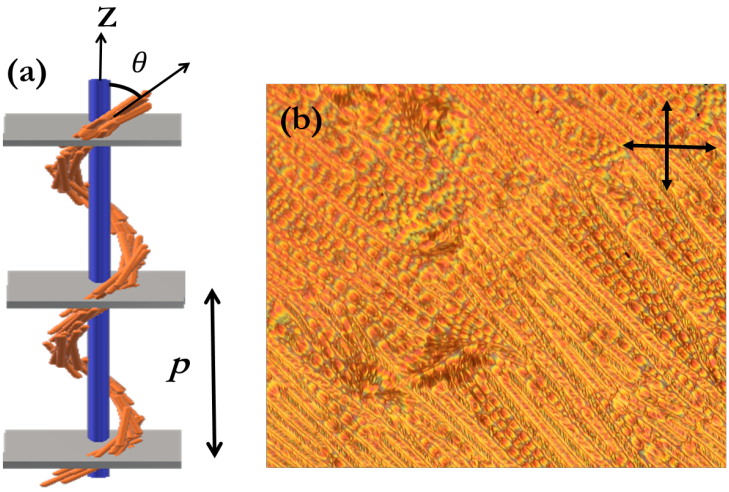

Figure 1.15: (a) Schematic representation of an N_{TB} phase. The director $\hat{n}$ precession helically along the z direction, with constant conical (θ) and pitch p (b) N_{TB} phase of CB9CB at T= 86°C showing the focal conic texture.

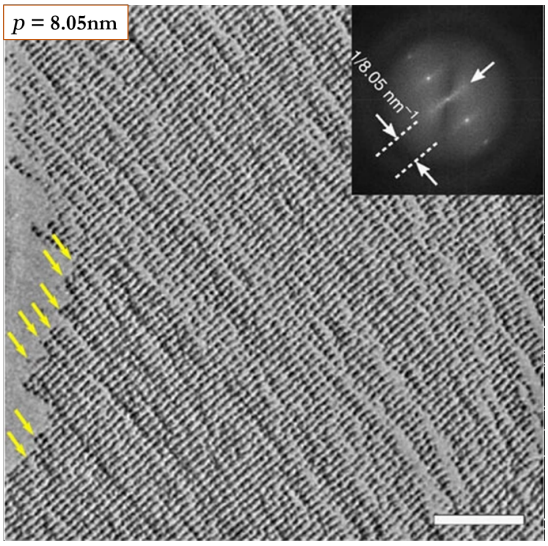

Figure 1.16: FFTEM textures and corresponding fast Fourier transform (FFT) patterns of CB7CB with pitch $p = 8.05$ nm. Scale bar, 100nm. (Adapted from Ref. [15].)

is inherently chiral, so the helical N_{TB} phase spontaneously separates into macroscale domains of opposite-handedness when formed from an achiral material.

1.4.4 Ferroelectric nematic liquid crystal (N_F)

The idea that a nematic phase could be ferroelectric was first suggested by Max Born in 1916 [26]. Decades later, Frank *et al.* discussed the consequence of polar order on elastic free energy density and showed that, in this case, the director lacked head-tail symmetry [27]. Despite intense research, this phase was elusive. Very recently, Nishikawa *et al.* In 2017 [28] reported that a molecule having a $1,3-dioxane$ unit in the mesogenic core exhibits a polar arrangement and later Mandle *et al.* [29] designed a family of rod-like molecules with a terminal nitro group and alkyloxy side group, which exhibit nonpolar nematic to polar nematic phase transition. Initially it was named as splay nematic N_S and later it was confirmed to be a ferroelectric nematic phase N_F. The molecules are wedge or pear-shaped because the NO_2 group at the terminal and have a large axial dipole moment (11.3D) and exhibits spontaneous splay with a large spontaneous electric polarization $\mathbf{P}$ as schematically shown in Fig1.17. A typical texture of the N_F phase is shown in Fig.1.18.

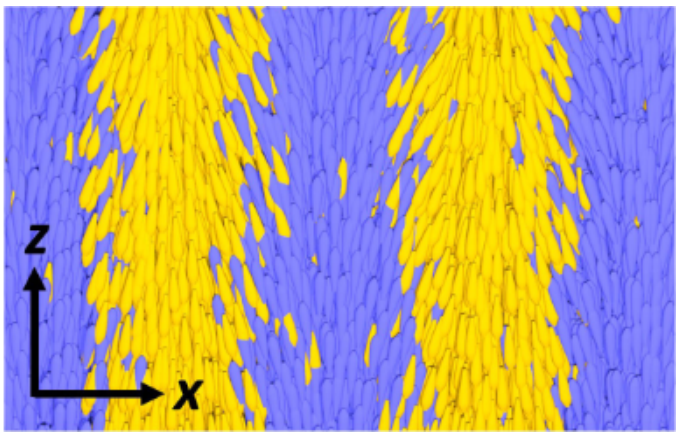

Figure 1.17: Schematic representation of N_S phase with polar order modulation. Different colors denote the molecular orientation of the director along $\hat{n}$ and $-\hat{n}$ (Adapted from Ref. [32]).

The ferroelectric nematic phase is more useful than conventional liquid crystal materials because of its faster response time. They are able to produce more colors and

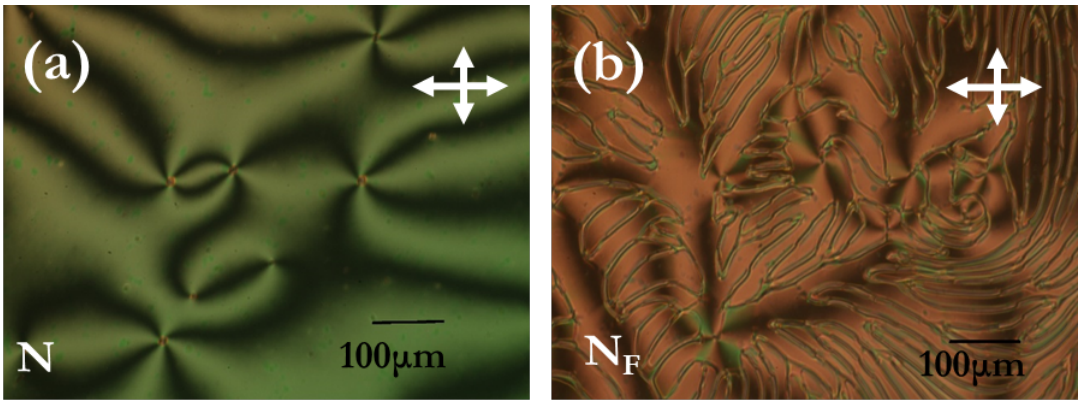

Figure 1.18: (a) Nematic phase and (b) Ferroelectric nematic (N_F) phase with defect lines under cross polarizers.

can operate at low voltages, which makes them more energy-efficient [19].

1.5 Physical properties of liquid crystal

This section discusses some physical properties of the liquid crystals relevant to our studies in the subsequent chapters.

1.5.1 Dielectric Constant

The dielectric constant of the liquid crystals is related to the response of the LC molecules to the applied electric field. The molecular charge distribution and intermolecular interactions affect the dielectric constant. The dielectric constant of liquid crystals with polar molecules is due to the both induced and permanent dipole moments, which have a tendency to align themselves parallel to the externally applied field. The dielectric constant depends on the temperature and the frequency of the applied electric field. In liquid crystals, two components of the dielectric constant ($\epsilon_\perp$ and $\epsilon_\parallel$) can be measured depending on the direction of the applied electric field with respect to the LC director ($\hat{n}$). The symbols $\epsilon_\parallel$, $\epsilon_\perp$ represents components with applied field parallel and perpendicular to the director. The applied electric field perpendicular to the LC director gives $\epsilon_\perp$ and parallel to the director gives $\epsilon_\parallel$ (see Fig.1.19). The

dielectric anisotropy is defined as:

$$\Delta\epsilon = \epsilon_{\parallel} - \epsilon_{\perp} \tag{1.30}$$

and it could be greater or less than zero depending on the molecular structure.

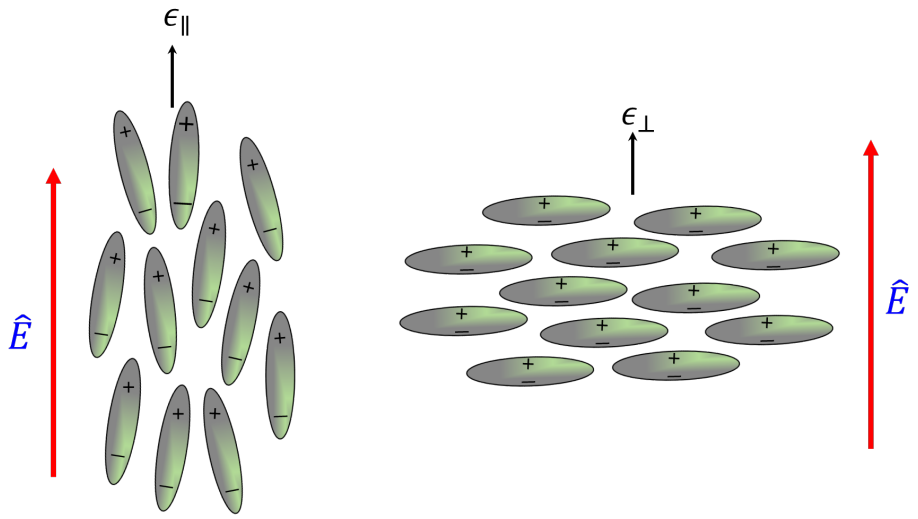

Figure 1.19: Schematic diagram showing parallel and perpendicular components of ($\epsilon_{\parallel}$ and $\epsilon_{\perp}$) the dielectric constant of the nematic LCs

1.5.2 Curvature elastic constants

Any external force can easily deform nematic liquid crystals since they are orientationally ordered fluids. The derivatives of $\vec{n}$(r) emerge when a director distortion is produced, which causes an elastic restoring torque that tends to return $\vec{n}$(r) to the undisturbed condition. Splay, twist, and bend are the three basic curvature deformations that can be combined to depict elastic deformation. Figure.1.20 shows a schematic illustration of these elastic distortions. The deformation free energy density is expressed as [7, 22, 27]:

$$F_N = \frac{1}{2}K_{11}(\nabla.\hat{n})^2 + \frac{1}{2}K_{22}(\hat{n}.\nabla \times \hat{n})^2 + \frac{1}{2}K_{33}(\hat{n} \times \nabla \times \hat{n})^2 \tag{1.31}$$

where K_{11}, K_{22} and K_{33} are called splay, twist and bend elastic constants, respectively. Usually in rod-like molecules, $K_{33} > K_{11} > K_{22}$ and these elastic constants are positive and typical magnitude of those constants is about 10^{-12}N.

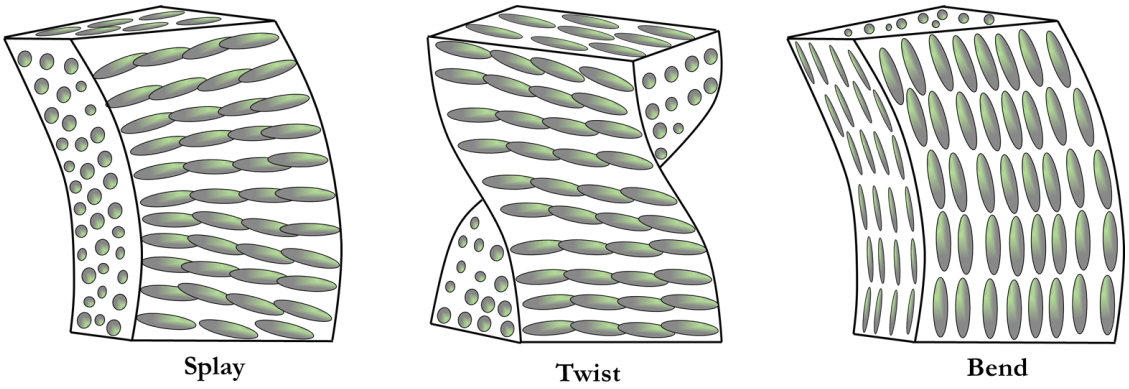

Figure 1.20: Schematic representation of splay, twist and bend distortion of LC director.

1.5.3 Rotational viscosity

The speed of electro-optical switching depends on the rotational viscosity (γ_1) of the liquid crystals. It can be measured by adapting an electro-optic technique as described in chapter-II. The magnitude of γ_1 depends on the structure of the molecules, intermolecular interactions, and temperature. For nematics, γ_1 can be obtained from the relation [35, 36]:

$$\gamma_1 = \frac{\tau_o K_{11} \pi^2}{d^2} \tag{1.32}$$

where K_{11} is the splay elastic constant, d is the thickness of the NLCs in planar cells and τ_o is the relaxation time of the director.

1.5.4 Alignment of liquid crystals in cells

In an unaligned sample, the liquid crystal director ($\hat{n}$) varies nonuniformly in space. Hence, it is crucial to align the LC director before measuring physical properties, such as birefringence dielectric constant, curvature elastic constants, rotational viscosity, etc. Moreover, the display applications require uniform alignment of the director. The director alignment is achieved with the appropriate surface boundary conditions (confined between two chemically treated glass substrates). Usually two types of LC alignments are used for physical measurements i.e, homogeneous, also called (planar) and homeotropic (also called perpendicular) [37, 38]. The schematic diagrams of these

two types of alignments are shown in Fig.1.21

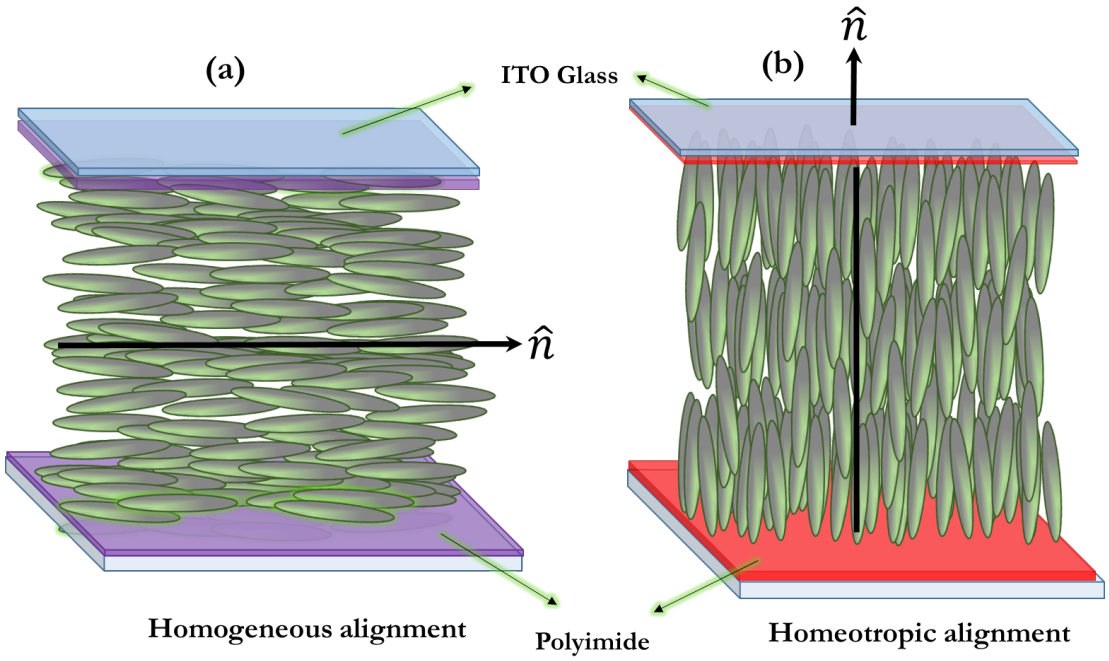

Figure 1.21: Schematic diagram of (a) homogeneous and (b) homeotropic alignments of nematic LCs.

1.5.4.1 Homogeneous alignment

If the alignment of the molecules is parallel to the plane of the glass substrate, then it is called as homogeneous or planar alignment. By coating with the appropriate polyimide on the glass substrate followed by rubbing, micro-grooves are formed on the glass surface along which the LC director can align in parallel to the substrate. The optic axis of the LCs is aligned along the rubbing direction for a uniaxial nematic liquid crystal. Fig.1.21(a) shows the schematic representation of the homogeneous alignment.

1.5.4.2 Homeotropic alignment

If the alignment of the molecules is perpendicular to the plane of the glass substrate, then it is called as homeotropic alignment. This alignment can be obtained by coating the glass substrates with a suitable polyimide which gives a perpendicular anchoring to the LC molecules. In this case, the molecules having amphiphilic polar groups

are attached to the surface, whereas aliphatic alkyl chains stand perpendicular to the surface. The interaction between alkyl chains and LC molecules makes them align perpendicular to the glass substrate. The schematic representation of homeotropic alignment is shown in Fig.1.21(b).

1.5.5 Freedericksz transition

External electric field can reorient the LC director. The transition from a uniformly aligned state of LC to a deformed state by applying an electric or magnetic field is called the Freedericksz transition. The dielectric displacement in a nematic liquid crystal under an electric field is expressed as [39, 40],

$$\vec{D} = \epsilon_o \Delta\epsilon (\hat{n} \cdot \vec{E})\hat{n} + \epsilon_o \epsilon_\perp \vec{E} \tag{1.33}$$

and the nematic dielectric energy density is given by,

$$W_{diel} = -\int_0^E \vec{D} \cdot d\vec{E} = -\frac{1}{2}\epsilon_o \epsilon_\perp \vec{E}^2 - \frac{1}{2}\epsilon_o \Delta\epsilon (\hat{n} \cdot \vec{E}^2) \tag{1.34}$$

In the above Eq.(1.34), the dielectric energy can be minimised when the director ($\hat{n}$) is

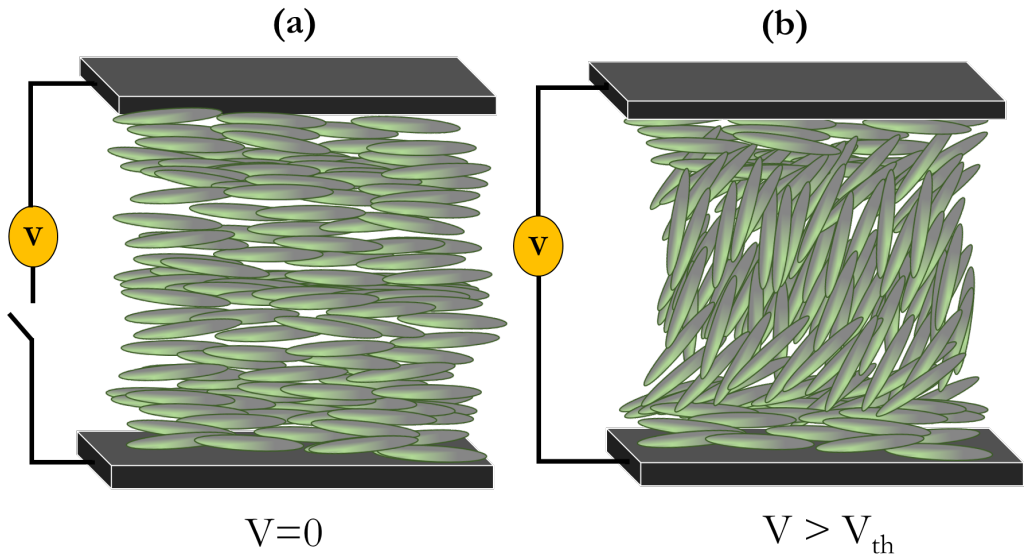

Figure 1.22: Freedericksz transition: Molecular orientation when the applied voltage (a) $V = 0$ V, (b) $V \gg V_{th}$.

parallel to the electric field ($\vec{E}$), which depends on the sign of the $\Delta\epsilon$. In homogeneously

aligned nematic LCs with $\Delta\epsilon > 0$, if an electric field is applied perpendicular to the director, after a certain field, the director reorients along the field direction [41], called as Freedericksz transition (see Fig.1.22). The corresponding voltage is called as Freedericksz threshold voltage and given by,

$$V_{th} = \pi\sqrt{\frac{K_{11}}{\epsilon_o \Delta\epsilon}} \tag{1.35}$$

where K_{11} is the splay elastic constant, $\Delta\epsilon$ is the dielectric anisotropy.

1.6 Viscosity of nematics LCs

The theory of viscosity of nematic LCs was first explained by Ericksen [45, 46]. He described the stress tensor for the flowing nematic in the absence of elastic stress. However, because of the strong anchoring of the director at the bounded walls, the flow gradients produced by shear will distort the director field, leading to elastic stress known as Frank elastic stresses. Thus Ericksen's theory failed to explain the flow of real nematics [2].

Later Leslie considered the importance of Ericksen's and Frank's elastic theories to explain the viscosity of flow nematics [27]. He gave a constitutive equation for the viscous stress tensor (σ) by combining Ericksen and Frank elastic stress tensors known as Leslie-Ericksen theory, which involves the six Leslie coefficients (Eq.1.36). The Leslie-Ericksen equation for the nematic stress tensor can be written as [2, 44]

$$\begin{aligned}\tilde{\sigma}_{i,j} = \; & \alpha_1 n_k A_{kp} n_p n_i n_j + \alpha_2 N_i n_j + \alpha_3 n_i N_j + \alpha_4 A_{ij} \\ & + \alpha_5 n_j A_{ik} n_k + \alpha_6 n_i A_{jk} n_k \end{aligned} \tag{1.36}$$

where α_1, α_2.....,α_6 are the Leslie coefficients, $\mathbf{A}$ is the velocity gradient tensor and $\mathbf{N}$ is the rotation of the director relative to the background fluid. These coefficient are not easily experimentally measurable.

Here we discuss the viscosity of nematic LC based on the three fundamental orientations of the director ($\hat{n}$) with respect to the shear flow. A schematic diagram of these

possible orientations is shown in Fig.1.23. They are called Meisowicz viscosities and is defined as :

(a) η_1: when $\hat{n}$ is parallel to ∇v (velocity gradient direction), (Fig.1.23(a))

(b) η_2: when $\hat{n}$ is parallel to v (shear direction), (Fig.1.23(b))

(c) η_3: when $\hat{n}$ is perpendicular to both v and ∇v. (Fig.1.23(c))

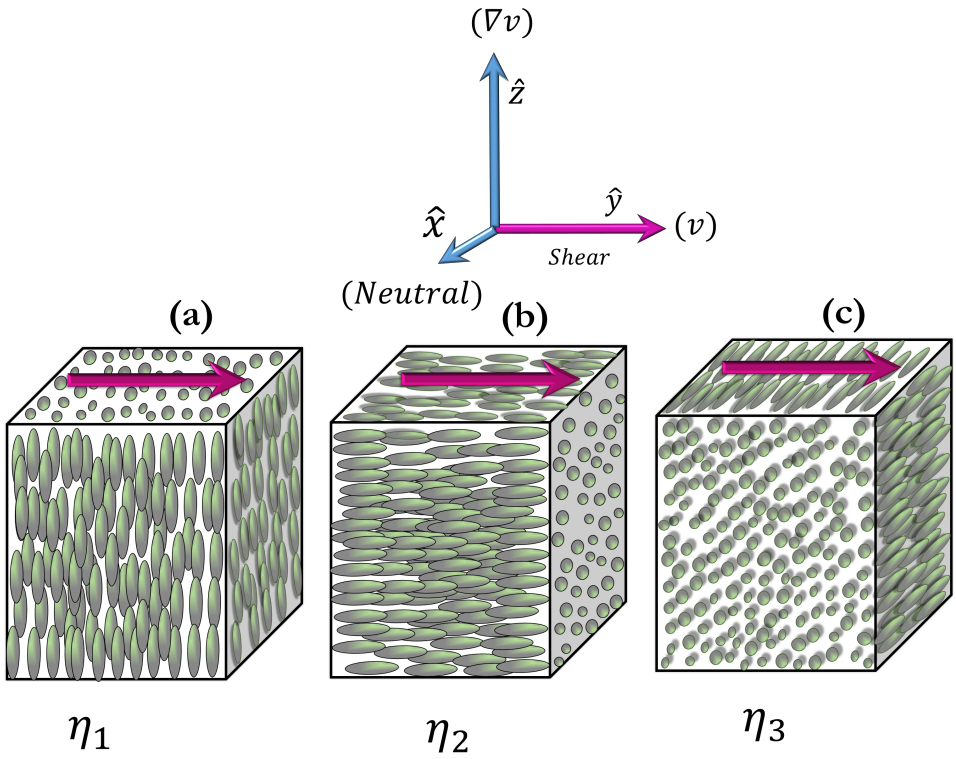

Figure 1.23: Schematic representation of the three basic nematic director orientations with respect to shear flow. The magenta colour arrow shows the direction of the shear flow.

When the director makes and orbitary angle with respect to the flow as shown in Fig.1.24, the Miesowicz viscosities η_1, η_2 and η_3 can be expressed in terms of Leslie coefficients as [2, 48]:

$\eta_1 = \frac{-\alpha_2+\alpha_4+\alpha_5}{2}$, when $\theta = 0$, $\phi = 0$,

$\eta_2 = \frac{\alpha_3+\alpha_4+\alpha_6}{2}$, when $\theta = \pi/2$, $\phi = \pi/2$,

$\eta_3 = \frac{\alpha_4}{2}$, when $\theta = \pi/2$, $\phi = 0$.

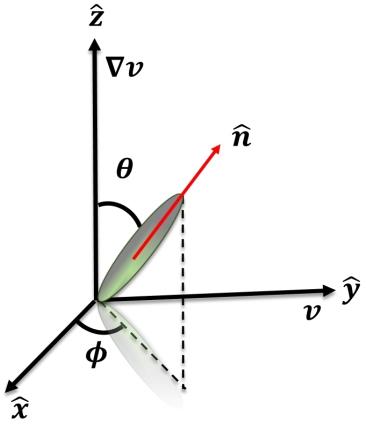

Figure 1.24: Schematic diagram of orbitary orientation of director $\hat{n} = (\sin\theta\cos\phi, \sin\theta\sin\phi, \cos\theta)$ under shear flow (v).

Out of these three viscosities, η_1 and η_2 can be measured experimentally using a standard rheometer.

References

[1] I. W. Flügge. *Viscoelasticity*, Springer-Vrlag, Newyork Heidelberg. berlin. 2nd Edition, 1975.

[2] R. G. Larson. *The structure and rheology of complex fluids*. Oxford University Press, New York, 1999.

[3] R. B. Bird, C. F. Curtiss, R. C. Armstrong and O. Hassager. *Dynamics of polymeric liquids*, Vol2: Kinetic theory, 2nd Edition, Wiley, Newyork, 1987.

[4] M. Sultan. Thesis title: *Towards a high pressure piezoelectric axial vibrator rheometer*. L'Universite de pau et despays de l'adour France, 2012.

[5] D. Coates. *The Chemistry of liquid crystals.* Springer US, pp.375, 1991.

[6] O. Lehmann, Z. Physikal. Chem. 4, 462 (1889).

For a brief historical account of the early work see, H. Kelker and R. Hatz, Handbook of liquid crystals, Verlag Chemie, Weinheim, Chapter 1 (1980).

[7] P. G. de Gennes and J. Prost. *The physics of liquid crystals*. International series of monographs on physics, Clarendon Press, 1993.

[8] W. H. de Jeu. *Physical properties of liquid crystalline materials*. Liquid Crystal Monographs, Gordon and Breach, 1980.

[9] H. A. Barnes, J. F. Hutton and K. Walters. *An Introduction to rheology*. Elsevier science publishers, Netherlands, 3^{rd} edition, 1993.

[10] D. Andrienko. *Introduction to liquid crystals.* Jour of Molecular Liquids. 267, 520 (2018).

[11] I. Dierking. *Chiral liquid crystals: Structures, phases, effects.* Symmetry, 6, 444 (2014).

[12] Z. Jamain, A. N. A. Azman, N. A. Razali, M. Z. H. Makmud. *A Review on Mesophase and Physical Properties of Cyclotriphosphazene Derivatives with Schiff Base Linkage.* Crystals. 12, 1174 (2022).

[13] P. Subhapriya, V. N. Vijayakumar, M. L. N. Madhu Mohan and P. S. Vijayanand. *Study and characterization of double hydrogen-bonded liquid crystals comprising p-n alkoxy benzoic acids with azelaic and dodecane dicarboxlic acids.* Mol. Cryst. Liq. cryst. 36, 537 (2011).

[14] A. S. Sonin. *Introduction to physics of liquid crystals.* Moscow: Nauka; 1983. (in Russian).

[15] V. Borshch, Y. -K. Kim, J. Xiang et al. *Nematic twist-bend phase with nanoscale modulation of molecular orientation.* Nat. Commun. 4, 2635 (2013).

[16] I. Dozov. *On the spontaneous symmetry breaking in the mesophases of achiral banana-shaped molecules.* Europhys. Lett. 56, 247 (2001).

[17] R. B. Meyer. in *Molecular Fluids.* Les Houches Lectures, 1973. (R. Balian, G. Weill, eds) 271–343 (Gordon and Breach, 1976).

[18] Y. Bouligand, M. O. Soyer, and S. Puiseux-Dao. *The fibrillary structure and orientation of chromosomes in Dinoflagellata.* 24, 251 (1968). (Article in French)

[19] X. Chen, D. Dong, X. Wei, R. Shao, et al. *First-principles experimental demonstration of ferroelectricity in a thermotropic nematic liquid crystal: Polar domains and striking electro-optics.* Proc. Natl. Acad. Sci. USA 117, 14021 (2020).

[20] D. Chen, J. H. Porada, J. B. Hooper, et al. *Chiral heliconical ground state of nanoscale pitch in a nematic liquid crystal of achiral molecular dimers.* Proc. Natl. Acad. Sci. U S A. 110, 15931 (2013).

[21] Ch. Zhu, M. R. Tuchband, A. Young, et al.*Resonant carbon K-edge soft x-ray scattering from lattice-free heliconical molecular ordering: soft dilative elasticity of the twist-bend liquid crystal phase.* Phys. Rev. Lett. 116, 147803 (2016).

[22] S. Chandrasekhar. *Liquid Crystals*. Cambridge University Press, 1992.

[23] J. W. Goodby, M. A. Waugh, S. M. Stein, E. Chin, R. Pindak, and J. S. Patel. *Characterization of a new helical smectic liquid crystal*. Nature. 337, 449 (1989).

[24] S. R. Renn and T. C. Lubensky. *Abrikosov dislocation lattice in a model of the cholesteric-to-smectic-A transition*. Phys. Rev. A. 38, 2132 (1988).

[25] P. A. Pramod, R. Pratibha, and N. V. Madhusudana. *A three-dimensionally modulated structure in a chiral smectic-C liquid crystal*. Current Science. 73, 761 (1997).

[26] Born Max. *Über anisotrope Flüssigkeiten. Versuch einer Theorie der flüssigen Kristalle und des elektrischen KERR-Effekts in Flüssigkeiten.* Sitzungsber. Preuss. Akad Wiss. 30, 614 (1916).

[27] F. C. Frank. *I. Liquid Crystals. On the Theory of Liquid Crystals.* Discuss Faraday Soc. 25, 19 (1958).

[28] H. Nishikawa, K. Shiroshita, H. Higuchi, Y. Okumura, Y. Haseba, S. Yamamoto, K. Sago, and H. Kikuchi. *A Fluid Liquid-Crystal Material with Highly Polar Order.* Advanced Materials. 29, 1702354 (2017).

[29] R. J. Mandle, S. J. Cowling, and J. W. Goodby. *Rational Design of Rod-Like Liquid Crystals Exhibiting Two Nematic Phases.* Chem. Eur. J. 23, 14554 (2017).

[30] H. K. Bisoyi, G. Singh, M. R. Fisch, D. M. Agra-Kooijman, Q. Li and S. Kumar. *Chiral and orientationally ordered fluid mesophases formed by oxadiazole bisaniline based achiral bent mesogens*. Liq. cryst. 46, 1373 (2019).

[31] M. Cestari, S. Diez-Berart, D. A. Dunmur, A. Ferrarini, M. R. de la Fuente, D. J. B. Jackson, D. O. Lopez, G. R. Luckhurst, M. A. Perez-Jubindo, R. M. Richardson, J. Salud, B. A. Timimi, and H. Zimmermann. *Phase behavior and*

properties of the liquid-crystal dimer 1″,7″*-bis(*4*-cyanobiphenyl-*4′*-yl) heptane: A twist-bend nematic liquid crystal.* Phys. Rev. E. 84, 031704 (2011).

[32] A. Mertelj, L. Cmok, N. Sebastián, J. Mandle, R. R. Parker, A. C. Whitwood, J. W. Goodby, and M. Čopič. *Splay Nematic Phase.* Phys. Rev. X. 8, 041025 (2018).

[33] M. P. Rosseto, J. V. Selinger. *Theory of the splay nematic phase: Single versus double splay.*Phys. Rev. E. 101, 052707 (2020).

[34] J. V. Selinger. *Interpretation of saddle-splay and the Oseen-Frank free energy in liquid crystals*, Liq. Cryst. Rev. 6, 129 (2018).

[35] S. T. Wu and C. S. Wu. *Experimental confirmation of the osipov-terentjev theory on the viscosity of nematic liquid crystals.* Phys. Rev. A. 42, 2219 (1990).

[36] M. L. Dark, M. H. Moore, D. K. Shenoy, and R. Shashidhar. *Rotational viscosity and molecular structure of nematic liquid crystals.* Liq. cryst. 33, 67 (2006).

[37] A. A. Sonin. *The surface physics of liquid crystals.* Taylor and Francis, 1995.

[38] K. Takatoh, M. Sakamoto, R. Hasegawa, M. Koden, N. Itoh, and M. Hasegawa. *Alignment technology and applications of liquid crystal devices.* CRC Press, 2005.

[39] H. J. Deuling. *Deformation of nematic liquid crystals in an electric field.* Mol. Cryst. Liq. Cryst. 19, 123 (1972).

[40] H. Gruler and G. Meier. *Electric field-induced deformations in oriented liquid crystals of the nematic type.* Mol. Cryst. Liq. Cryst. 16, 299 (1972).

[41] L. M. Blinov and V. G. Chigrino. *Electrooptic effects in liquid crystals.* Springer-verlag, New York, 1996.

[42] T. Mezger. *The handbook of Rheology.* 4th edition, Vincentz Network, Hanover, Germany, 2014.

[43] P. Sollich, F. Lequeux, P. Hébraud, and M. E. Cates. *Rheology of Soft Glassy Materials.* Phys. Rev. Lett. 78, 2020 (1997).

[44] F. M. Leslie. *Some Constitutive Equations For Anisotropic Fluids.* J. Mech. Appl. Math. 19, 357 (1966).

[45] J. L. Ericksen. *Anisotropic fluids.* Arch. Ration. Mech. Anal. 4, 231 (1959).

[46] J. L. Ericksen. *Conservation laws for liquid crystals.* Trans. Soc. Rheol. 5, 23 (1961).

[47] M. Miesowicz. *The three coefficients of viscosity of anisotropic liquids.* Nature. 158, 27 (1946).

[48] I. W. Stewart. *The Static and Dynamic Continuum Theory of Liquid Crystals: A Mathematical Introduction.* Liquid Crystals Book Series, Taylor and Francis, 2004.

2

Experimental Setup

2.1 Introduction

In this chapter, we discuss different experimental techniques used in this thesis. We used a strain-controlled rheometer (MCR-501) for all rheological measurements. It has several attachments like electro-rheology, rheomicroscopy, magnetorheology and rheo-SALS (small angle light scattering). In addition, we also discuss an electro-optic technique which is used for the measurements of rotational viscosity of nematic LCs.

2.2 Rheometer

We use a modular compact rheometer (MCR-501 Anton Paar) see Fig.2.1(a). It has an EC (electrically commutated) synchronised motor supported by air bearings and a high-resolution optical encoder (Fig.2.1(b)). It controls the angular deflection and can precisely measure angular displacements as tiny as 0.1 μrad. Two air bearings, referred to as radial and axial, support the synchronous EC motor. The radial bearing normally stabilises the centre rod in the motor part, whereas the axial bearing supports the total weight of the spinning parts. Because of the assistance provided by such air bearings, the MCR can measure the low torque down to a minimum of 0.5 nNm. The normal force sensor, which is attached to the air bearings, measures the normal stress. Depending on the behaviour of the sample, it measures the normal force in both the upward (positive) and downward (negative) directions during the dynamic and stable states. Rheological measurements are controlled and analysed using the Rheoplus software. The exact and optimum gap sizes between the two measuring geometry

plates are regulated by TruGap technology [1]. The bottom plate of the rheometer

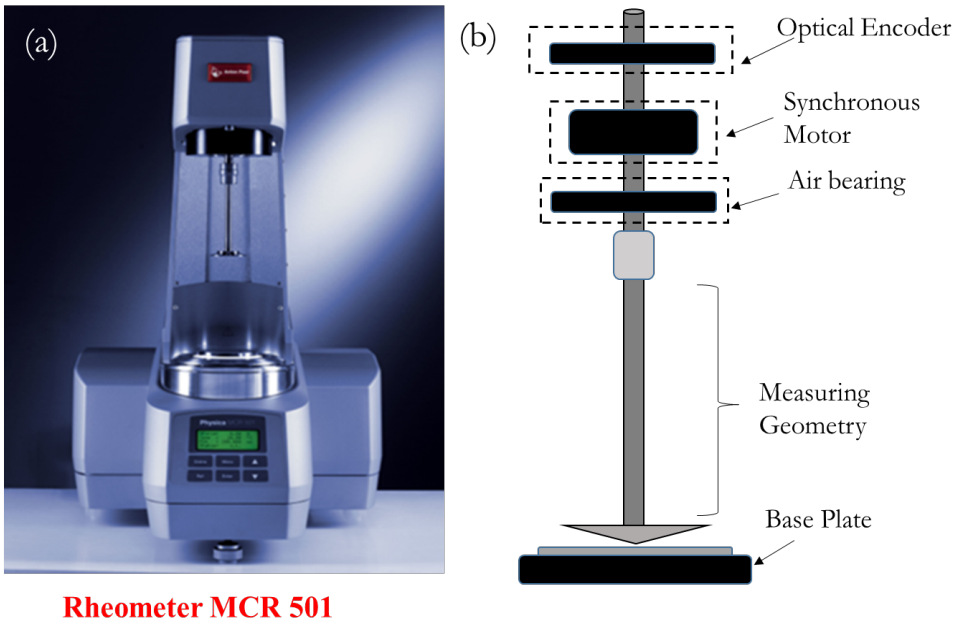

Figure 2.1: (a) Picture of the rheometer (MCR-501) (b) Main components of the MCR rheometer.

is immovable, and the upper plate is movable. The rheometer is equipped with a Peltier temperature controller system with a peltier hood to maintain the required temperature within an accuracy of 0.1°C. The rheometer is connected to an oil-free compressor for the functioning of air bearings, which provides 5-8 bars of pressure to the rheometer. A chiller is also attached to it to circulate the water throughout the system to maintain the temperature. All the rheological measurements are carried out through the Rheoplus software [1]. According to the response of the sample, a broad range of measuring systems are used to measure the rheological properties.

2.3 Measuring geometries

The measurement geometry can be classified into three basic categories: (1) cone-plate (CP), (2) parallel-plate (PP), and (3) cylindrical (coaxial cylindrical (CC) and double-gap cylindrical (DG) measuring systems). In our experiments we mostly used two measurement geometries i.e., cone-plate and parallel-plate systems. Here we present a brief description of these measuring systems.

2.3.1 Cone and plate measuring system (CP)

This measuring system consists of two crucial parts. A conical-surfaced bob (upper plate) and a flat-surfaced fixed plate (lower plate).

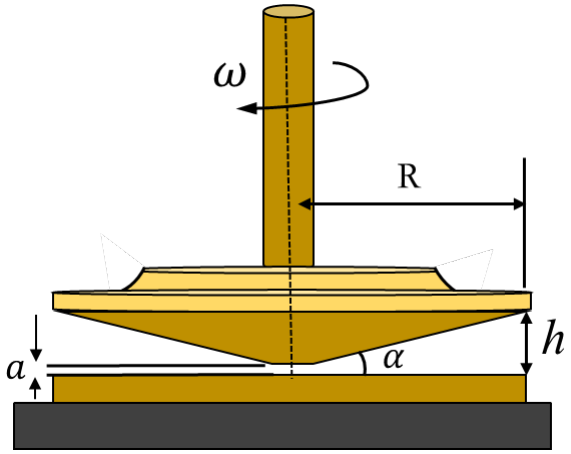

Figure 2.2: Schematic diagram of cone-and-plate measuring system. The symbols represent the following parameters: R - cone radius, h - the gap between the two plates at the edge, α - cone angle, ω - angular frequency and a - the truncated gap between the plates.

The cone radius "R" and the cone angle "α" of the conical surface of the measuring device are important for achieving accuracy of the measurements. The sample exerts torque (M) on the upper plate, which are available in two distinct diameters i.e., 25 mm and 50 mm. For low-viscosity fluids, 50 mm plate provides greater accuracy than 25 mm plate. It is because a plate with a greater radius has a larger shear area, consequently enhances sensitivity to low torque or shear stress values. Usually, the smaller plate (25 mm diameter) is employed for samples with higher viscosity. (The schematic illustration of a cone-plate measuring system is shown in Fig.2.2). For cone-plate systems shear stress (σ) and shear rate ($\dot{\gamma}$) can be expressed as.

$$\sigma = \frac{3M}{2\pi R^3} \tag{2.1}$$

$$\dot{\gamma} = \frac{\omega}{\alpha} \tag{2.2}$$

It should be noted that in CP measuring systems, the radius does not appear in cal-

culating shear rate. Hence, the shear rate remains constant across the whole sample. Therefore, compared to the parallel plate and cylindrical measuring systems, CP system is the most advantageous. The upper plate's truncated cone tip should touch the lower plate at one point to improve measurement accuracy. After mounting the sample on the lower plate, the measuring position in CP measuring systems, the gap between the truncated cone tip and the bottom plate, is always set. Below is a list of some CP systems available in our laboratory.

Plate	Cone angle (α)	Truncation gap (a)	diameter (mm)
CP25	1 °	50 μm	24.9
CP25	2 °	50 μm	24.9
CP50	0.50 °	49 μm	49.9
CP50	1 °	48 μm	49.9

Table 2.1: Details of cone angle, truncated gap and diameter of some CP systems

2.3.2 Parallel-plate measuring system (PP)

The upper and lower plates of the parallel-plate measurement system (PP) are flat. The lower plate is fixed, and the upper plate is movable. We have two PP measuring

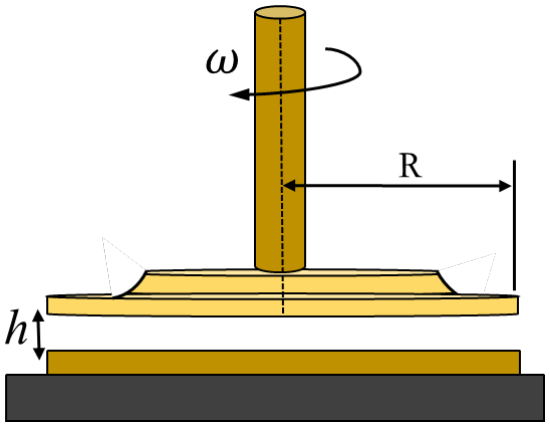

Figure 2.3: Schematic diagram of the parallel-plate measuring system. The symbols represent the following parameters: R - plate radius, h - the gap between the two plates, ω - angular frequency.

systems with diameters of 20 mm and 50 mm. Figure.2.3 shows the schematic diagram

of the parallel-plate measurement system. Because the gap between the plates can be adjusted with some freedom, a substantial sample volume is required. The stress σ and shear rate $\dot{\gamma}$ for PP systems are given below.

$$\sigma = \frac{2M}{\pi R^3} \tag{2.3}$$

and

$$\dot{\gamma} = \frac{\omega R}{h} \tag{2.4}$$

where, M is the torque exerted on the upper plate by the sample, and the distance (h) between two parallel plates must be less than the plate radius (R), or ($h \ll R$). Here ω, R and h are angular frequency, radius and height of the PP system, respectively. It should be noted that the shear rate is not uniform throughout the sample since it depends on the radius of the upper plate.

2.4 Rheo-dielectric measurements

We used parallel plate configuration for the simultaneous measurements of the rheological and dielectric properties by attaching an LCR meter (Agilent E4980A) to the rheometer Fig.2.4. For most of the rheo-dielectric measurements, we kept the plate gap in the range of 75 μm to 80 μm so that a small quantity of sample is required. The electric field was applied between the plates in an upward direction using two electrodes as shown in Fig.2.4(d). The top plate was connected to a low-friction spring wire electrode. The air correction *i.e.,* the contribution due to very small friction in the absence of the sample was subtracted from the measured quantities with the sample, such as viscosity.

The rheometer generates an alternative signal through the M1/M2 port for triggering the LCR meter. LCR meter output was connected to the rheometer plates to measure the capacitance and resistance of the sample. The data was stored in a USB 1.0 flash drive connected to the LCR meter Fig.2.4(b). For electrorheological measurements above 20 V, we have used a signal generator (Tektronix AFG3102) and

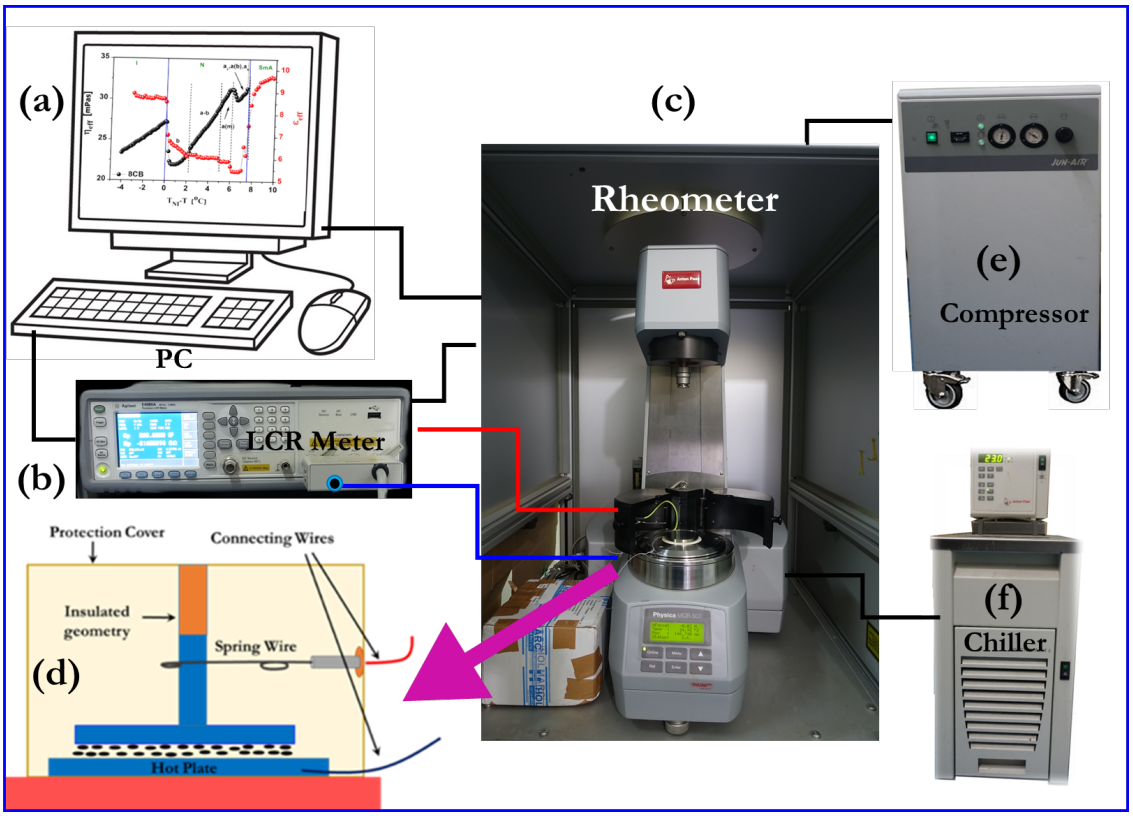

Figure 2.4: Schematic diagram of the rheo-dielectric setup (a) PC equipped with rheoplus and LabVIEW software to collect rheodielectric data (b) Agilent E4980A LCR meter: Red and blue lines are the connecting wires to supply voltage and to measure dielectric constant. (c) Rheometer. (d) Schematic diagram of parallel plate setup inside the protection cover where low-friction spring wire connected to the top plate. (e) Jun-Air compressor to provide air pressure to the rheometer (f) Antonpaar viscotherm VT2 chiller to maintain peltier temperature.

voltage amplifiers (TEGAM). Depending on the sample, the frequency of the sinusoidal voltage is kept in the range of 1-10 KHz. The calibration of the peltier heater was checked by measuring the phase transition temperature of some standard liquid crystalline materials.

2.5 Preparation of liquid crystal cell

Here, we briefly discuss the preparation of liquid crystal cells. Two indium-tin-oxide (ITO) coated glass plates with an ITO layer thickness of around 1500 Å and a resistivity of 15-20 Ω cm^2 were used to make Hele-Shaw type cells. The plates were thoroughly cleaned using distilled water, acetone, and hexane. We spin-coated the plates with different polyimides for the desired alignment of the LC molecules, i.e., planar and homeotropic. For the planar or homogeneous alignment, the glass plates were coated with polyimide AL-1254 and then cured at 180°C for 1 hour. For homeotropic alignment of LC molecules, the glass plates are treated with JALS-204 and cured at 200°C for 1 hour 15 min. The plates treated with AL-1254 are unidirectionally rubbed via a rubbing machine to align the LC molecules in a certain direction. The electrode regions overlap when the two plates are stacked on top of the other for a parallel plate capacitor configuration. They are bonded together using UV-curable glue (NOA-65 Norland) and silica beads of the appropriate diameter to maintain the gap. Using the interferometric technique [7], the cell gap was determined with an Ocean optics spectrometer (HR 4000CG-UV-NIR). Alternative maxima and minima make up the spectrum, and the gap d of the cell is determined by using the formula, $d = \frac{\lambda_m \lambda_n}{\lambda_n - \lambda_m} \times \frac{n-m}{2}$ where λ_n and λ_m are wavelengths of n^{th} and m^{th} minima or maxima. The electrical connections to the cells are given by soldering with copper wires. A schematic representation of the top view of a liquid crystal sample cell is shown in Fig.2.5.

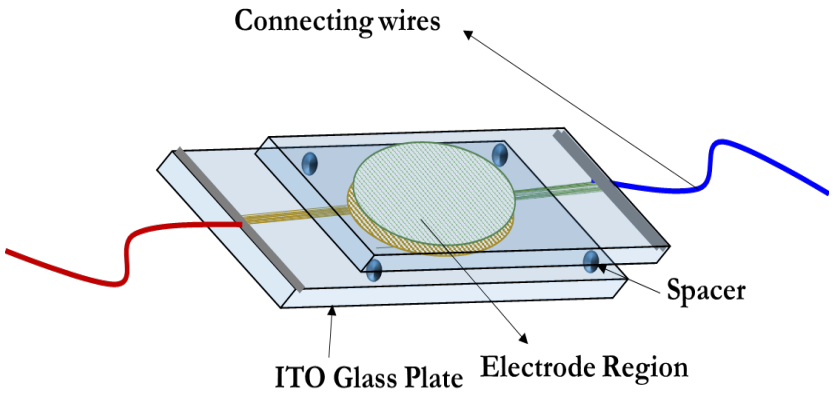

Figure 2.5: Schematic diagram of the cell made of ITO-coated glass plates. The circular region indicates the overlapped electrode area.

2.6 Polarizing optical microscope (POM)

A polarizing optical microscope (POM) is an important device for observing and photographing birefringent specimens. It helps to observe the optical and morphological properties of any birefringent materials like liquid crystals.

A POM is primarily equipped with a two linear - polarizers, one is called a polarizer, and another is called an analyser. Their axis of polarization is kept perpendicular to each other. Between these linear polarizers, a rotating sample stage and microscope objective are arranged in the line of the optical path. The emergent light from the objective is viewed through the eyepiece (ocular). To capture images, a charge-coupled device (CCD) camera is kept in the place of the eyepiece or a hybrid system called the trinocular. A schematic figure is shown (Fig.2.6(a)) when light passes through different components of the microscope. We use Olympus BX51 polarizing microscope to view the textures of different LC phases. A Köhler illumination system, which usually employs a xenon lamp, is used for uniform sample illumination. Various objectives (e.g., 5X, 10X, 20X, 50X) are used for the magnification of the image. In addition to that, it has accessories (e.g., intensity controller, condenser, colour filters, Bertrand lens, rotating noise piece etc) (Fig.2.6(b)). The illumination intensity I when a LC

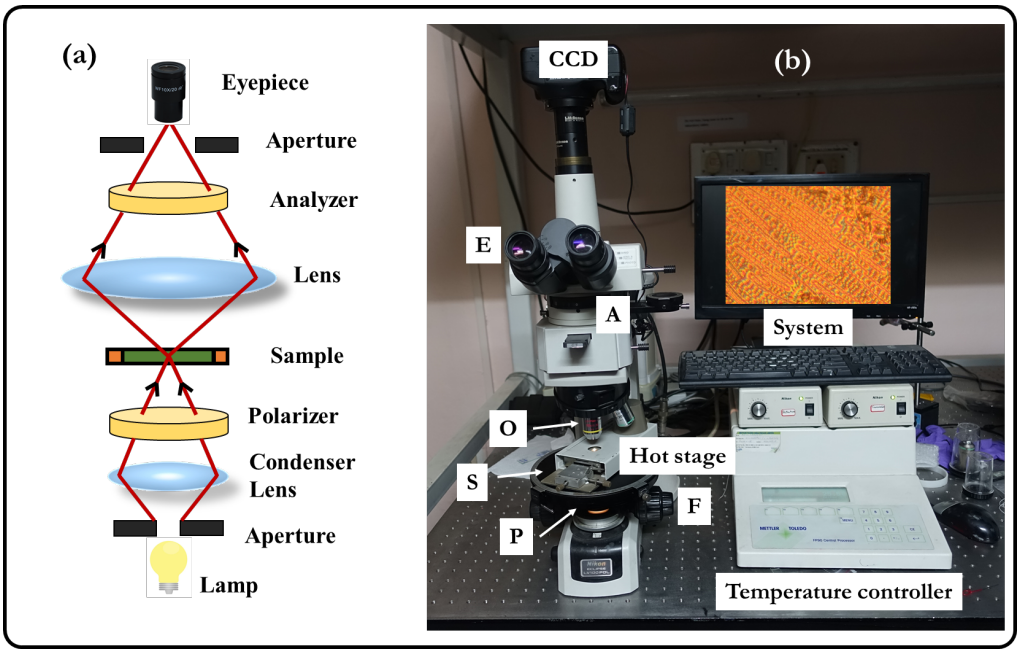

Figure 2.6: (a) Schematic diagram of light passing through different components of the polarizing microscope. (b) Photograph of microscope setup along with Mettler-Toledo temperature controller, the microscope parts are labelled as CCD (CCD camera) E (Eyepiece) A (Analyzer) O (Objective) S (Sample stage) P (Polarizer) F (Focus knob).

sample is viewed under a cross polarizers is given by [4, 5]

$$I = I_o \sin^2(2\phi) \sin^2(\frac{\delta}{2}) \tag{2.5}$$

where I_o is the light intensity after passing through the polarizer. ϕ is the angle between director projection on the sample plane (x-y plane) with the analyser axis as shown in Fig.2.7. δ is the phase difference between the extraordinary ray (n_e) and ordinary rays (n_o) which is given by

$$\delta = \frac{2\pi}{\lambda} \Delta n_{eff} d \tag{2.6}$$

where d is the length of light passing in a LC medium (width of the cell) λ is the wavelength of the light and Δn_{eff} is the effective birefringence.

When the optic axis (LC director) makes an angle θ with the direction of light propagation and $n_{\parallel}$ and $n_{\perp}$ are the refractive indices along long and short molecular

axis. The relation between n_e, n_o, $n_\parallel$ and $n_\perp$ are given by the relation [4]

$$n_e = \frac{n_\parallel n_\perp}{\sqrt{(n_\perp^2 \sin^2\theta + n_\parallel^2 \cos^2\theta)}}. \tag{2.7}$$

depending on the value of δ and the thickness of the cell (d), LCs show coloured textures and defects. The intensity of the light depends on the angle ϕ. We used a

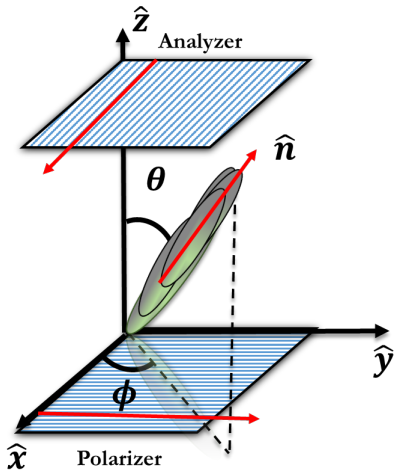

Figure 2.7: Schematic diagram of uniaxial LCs between cross polarizer.

temperature controller (Mettler -Toledo FP90 Central processor) for changing sample temperature while observing. We keep the sample cell inside the hot stage (FP82HT Hot Stage) which is mounted on rotating stage (Fig.2.6(b)). It can be operated from room temperature to maximum 375°C with an accuracy of ±0.8°C.

2.7 An electro-optic technique for measuring rotational viscosity (γ_1) of nematic LCs

To measure the rotational viscosity γ_1 we adopted the retardation relaxation method [10]. In this technique, the transmitted light intensity is measured through a planar-aligned LC cell to obtain optical retardation as a function of time. The schematic diagram of the experimental setup is shown in Fig.2.8. The experimental procedure is performed in two steps: (i) at a fixed temperature voltage-dependent intensity is

measured and (ii) by switching off the voltage, time-dependent transmitted intensity is measured. The voltage-dependent transmitted intensity is measured to get the maxima and minima. A representative variation of the voltage-dependent transmitted intensity of a 5CB nematic liquid crystal at 28 °C is shown in Fig.2.9(a). A voltage (V_b) is applied, and then it is switched off to measure the time-dependent transmission intensity of the liquid crystal by using an oscilloscope.

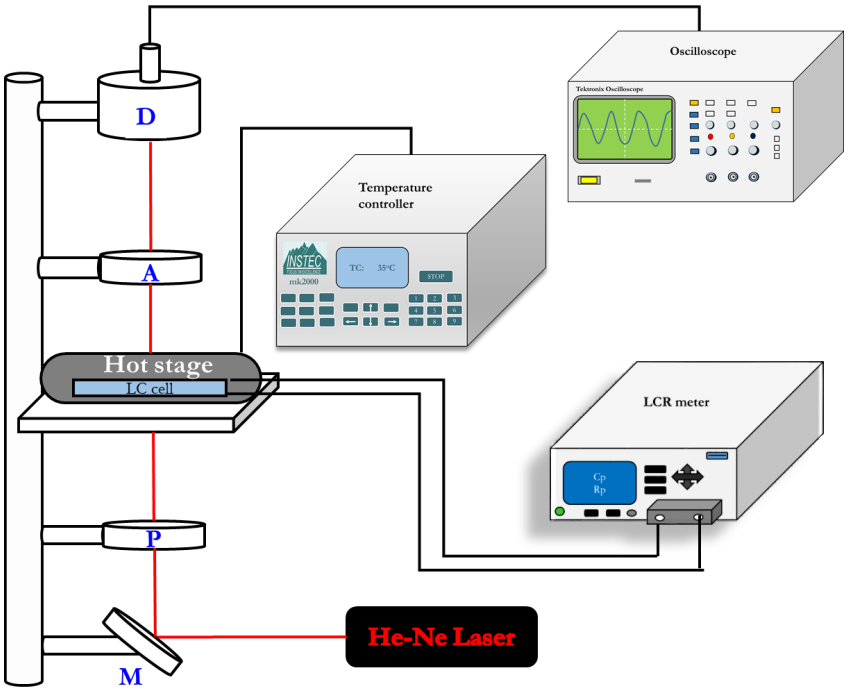

Figure 2.8: Experimental setup for measuring rotational viscosity. P- polarizer, A-analyser, M-Mirror, D-detector

The phase change $\delta(t)$ as a function of time (t) is measured from the time dependent intensity, $I(t)$ using the following equation:

$$I(t) = I_0 sin^2\left[(\Delta_{tot} - \delta(t))/2\right] \tag{2.8}$$

where I_0 is the maximum intensity change and Δ_{tot} is the total phase retardation. The phase decay (t) is given by the following equation [10, 11] :

$$\delta(t) = \delta(0)\, exp(\frac{-2t}{\tau_0}) \tag{2.9}$$

where $\delta(0)$ is the total phase change of the LC cell. The slope of the linear plot $ln[\delta(0)/\delta(t)]$ is $2/\tau_0$, and this gives the relaxation time (τ_0) (see Fig.2.9(b)). The

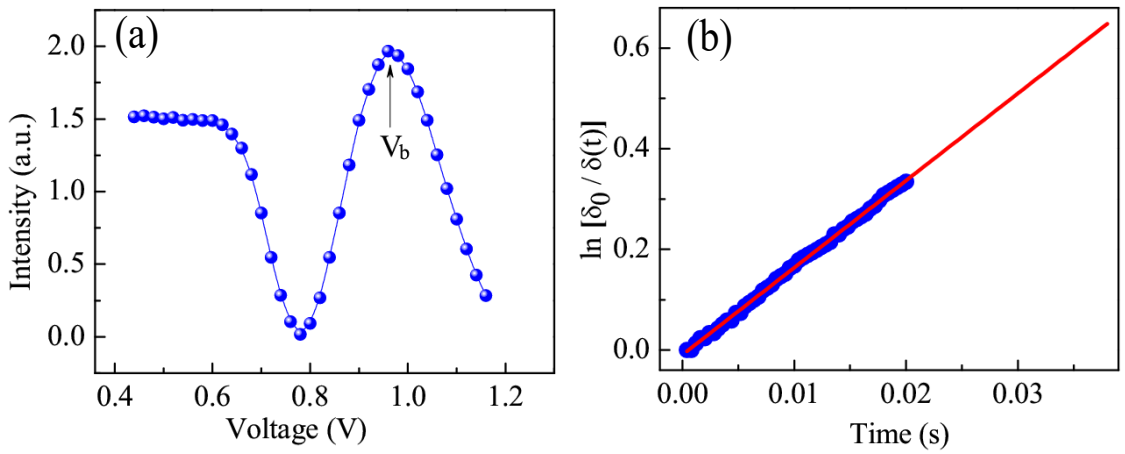

Figure 2.9: (a) The voltage-dependent transmission intensity of a standard nematic liquid crystal of 5CB LC at 28 °C. (b) A representative plot of linear variation of $\ln[\delta(0)/\delta(t)]$ with time (t).

rotational viscosity γ_1 of the sample is given by:

$$\gamma_1 = \tau_0 K_{11} \pi^2 / d^2 \tag{2.10}$$

where d is the thickness of the cell and K_{11} is the splay elastic constant.

References

[1] *Anton-paar instruction manual.*

[2] J. Läuger and P. Heyer. *Rheo-Microscopy: Simultaneous structural and rheological information.* Annual Transactions of the Nordic Rheology Society. 20, 179 (2012).

[3] A. R. Uribe, B. A. Tenorio, and M. E. R. Guzman. *A Small-Angle Light Scattering instrument to study soft condensed matter.* Rev. LatinAm. Metal. Mat. 30, 190 (2010).

[4] I. Dierking. *Textures of Liquid Crystals.* Wiley-VCH, Weinheim (2003).

[5] L. S. Hirst. *Fundamentals of Soft Matter Science.* 1st ed., CRC Press (Taylor and Francis), London (2012).

[6] H. Kawamoto. *The history of liquid-crystal display and its industry*, Third IEEE History of ELectro-technology Conference (HISTELCON), 1-6 (2012).

[7] K. H. Yang. *Measurements of empty cell gap for liquid-crystal displays using interferometric methods.* J. Appl. Phys. 64, 4780 (1988).

[8] G. Barbero and L. R. Evangelista. *An Elementary Course on the Continuum Theory for Nematic Liquid Crystals.* World Scientific, Singapore 2000.

[9] P. Sathyanarayana, B. K Sadashiva, and S. Dhara. *Splay-bend elasticity and rotational viscosity of liquid crystal mixtures of rod-like and bent-core molecules.* Soft Matter. 7, 8556 (2011).

[10] S. T. Wu and C. S. Wu. *Experimental confirmation of the Osipov-Terentjev theory on the viscosity of nematic liquid crystals.* Phys. Rev. A. 42, 2219 (1990).

[11] S. T. Wu. *Phase retardation dependent optical response time of parallel-aligned liquid crystals*. J. Appl. Phys. 60, 1836 (1986).

3

Smectic-like rheology and pseudolayer compression elastic constant of a twist-bend nematic liquid crystal

3.1 Introduction

Experimental discovery of twist-bend nematic (N_{TB}) phase in bent-core liquid crystals has created immense interests in liquid crystal community [1–7] although it was theoretically predicted much before from different perspectives [8–11]. In the N_{TB} phase, the director $\hat{\mathbf{n}}$ (the mean molecular orientation) exhibits periodic twist and bend deformations forming a conical helix and is tilted with respect to the axis $\mathbf{L}$ as shown in Fig.3.1(a). The typical pitch p of the heliconical structure is of the order of 10 nm, thus comparable to a few molecular length. Commonly, N_{TB} phase is observed in odd-membered liquid crystal dimers wherein two mesogenic units are connected through a flexible spacers [12–14]. A fascinating feature of the N_{TB} phase is the observation of spontaneous chirality i.e., formation of both left and right handed helical domains even though the constituent molecules are achiral. This leads to several unusual physical properties of N_{TB} phase compared to the conventional nematic phase (N) [15–21].

A few coarse-grained theories have been proposed to explain the emergence of N_{TB} phase from the high-temperature uniform nematic phase. Meyer and Dozov showed

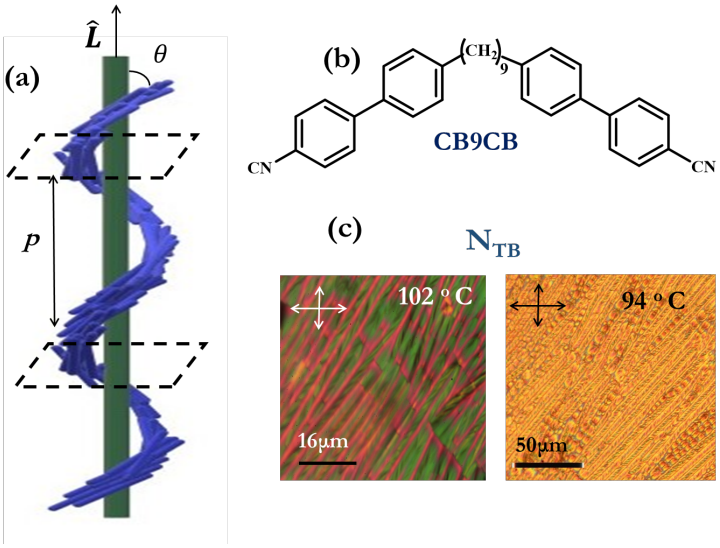

Figure 3.1: (a) Schematic view of heliconical molecular orientation of the nematic twsit-bend (N_{TB}) phase. p represents helical pitch equivalent to pseudo-layer thickness. (b) Chemical structure of CB9CB molecules used in the study. (c) Polarising optical microscope texture at 94°C and 102°C in the N_{TB} phase. **L** is the macroscopic average orientation of $\hat{\mathbf{n}}$ over several periods.

that the elastic properties of the N_{TB} phase could be viewed in two different length scales in reference to the pitch length (p) [22]. When the considered length (l) is less than p i.e., $l < p$, the elastic description is similar to that of the usual nematics. On the other hand, when $l >> p$, the elastic description is similar to regular lamellar systems such as cholesteric and smectic LCs [22]. In the latter picture, the thickness of one pitch can be considered as a pseudo-layer and the large-scale elasticity of the N_{TB} phase could be described in terms of an effective pseudo-layer compression elastic constant B_{eff} and an curvature elastic constant K_{11}^N and the corresponding free energy density of N_{TB} can be expressed as [22]:

$$f_{TB} = \frac{1}{2}B_{eff}\epsilon^2 + \frac{1}{2}K_{11}^N\left(\frac{1}{R_1} + \frac{1}{R_2}\right)^2 \tag{3.1}$$

where R_1, R_2 are the radii of pseudo layer curvatures and ϵ is the pseudo-layer compression. Another coarse-grained theory has been developed considering heli-polar order and their coupling with bend distortions [20, 23]. Both the theories predicted that the temperature dependence of B_{eff} is much faster than that of the usual SmA

LCs.

There have been a very few experimental studies on the measurements of B_{eff} of N_{TB} LCs [23–25]. For example, Gorecka *et al.* have measured B_{eff} of CB7CB and some chiral N_{TB} LCs. Their reported values are in the range of a usual SmA LC ($10^6 - 10^7$ Pa) and vary inversely with the temperature [24]. Parsouzi *et al.* have reported that B_{eff} is in the range of $10^3 - 10^4$Pa and it scales as $B_{eff} \sim (T_{TB} - N)^{3/2}$ [23]. Thus, there are several orders of magnitude difference in the reported values measured on two different samples using two different methods. The universal temperature dependence of B_{eff} is still an unresolved issue. In this paper we report experimental studies on the rheological properties of a N_{TB} LC. We use a novel method for measuring B_{eff} from the dynamic shear modulus $G^*(\omega)$. We discuss the temperature dependence of B_{eff} and compare with that proposed by the coarse-grained elastic theories of the N_{TB} phase.

3.2 Experimental

The LC material 1,ω-bis(4-cyanobiphenyl-4$'$-yl) alkane (CB9CB) was synthesised by our collaborators in Poland following the synthesis procedure reported in Ref. [14]. It is a cyanobiphenyl-based dimer with an odd number of methylene units ($n = 9$) in the flexible spacer (Fig.3.1(b)). It exhibits the following phase transitions: I 124°C N 108°C N_{TB} 84°C Cr. and enantiotropic transition with the widest temperature range of N_{TB} phase (22°C) among the LCs in the homologous series of CBnCB [14]. For comparison, we also studied 8CB (Octylcyano biphenyl), which shows the following phase transitions: I 41°C N 34°C SmA 22°C Cr. We used the strain-controlled Rheometer (MCR 501, Anton Paar) with a cone-plate measuring system having a plate diameter of 25mm and cone angle of 1° for rheological measurements. A Peltier temperature controller was attached to the bottom plate for controlling the temperature with an accuracy of 0.1°C. A hood was used to cover the measuring plates for uniformity of sample temperature. Temperature-dependent viscosity was measured by cooling the sample from the isotropic phase. For measuring the dynamic shear modulus, the sample was quenched from the isotropic to the N_{TB} phase at the rate of 15°C per min.

A total of 5g LC was synthesised, and about 200mg was used for each rheological measurements. The phase transitions and textures were initially observed using a polarising optical microscope (Olympus BX51) and a temperature controller (Mettler FP 90). A typical texture of an unaligned sample is shown in Fig.3.1(c). It is noticed that the textures of N_{TB} are very similar to that of the focal conic textures of usual SmA LCs.

3.3 Results and discussion

To begin with, we measure the shear viscosity of CB9CB as a function of temperature at two different shear rates ($\dot{\gamma}$ =100 and 10 s^{-1}) to identify the phase transition temperatures. Since the director orientation with respect to the shear direction usually changes with temperature, we define it as effective viscosity η_{eff}. As shown in Fig.3.2, the N to N_{TB} phase transition is identified from the rapid increase (more than two orders of magnitudes) of η_{eff} with respect to the N phase. The onset of the N-N_{TB} transition (108°C) is better seen in the inset of Fig.3.2. We also measured temperature-dependent η_{eff} of 8CB LC as shown in Fig.3.2. It is evident that the magnitude and the overall temperature dependence of η_{eff} of the two samples are very similar.

It indicates that the pretransitional fluctuations and the resulting director dynamics across the N-N_{TB} transition are similar to that of N-SmA transition [26–28]. In analogy with 8CB LC, three simplest orientations of the pseudolayers can be considered, wherein the layer normal is parallel to the vorticity ($\nabla \times v$), velocity gradient (∇v) and flow directions (v) as shown schematically in Fig.3.3. These are commonly known as perpendicular, parallel and transverse orientations. The large η_{eff} of the N_{TB} phase is expected to arise from the transverse orientation of the pseudo-layers similar to those reported in the SmA phase of 8CB LC [29].

We study the flow curve of N_{TB} phase and compared with that of the SmA phase of 8CB as shown in Fig.3.4. N_{TB} phase shows yield stress similar to that of the SmA phase of 8CB LC. However, the rheology of SmA phase is complex as it shows a shear-induced structural transition [30]. A small but discontinuous change of σ_{eff} near $\dot{\gamma}$ = 8 s^{-1} in Fig.3.4 and increase in η_{eff} at 24°C (Fig.3.2) could be a signature

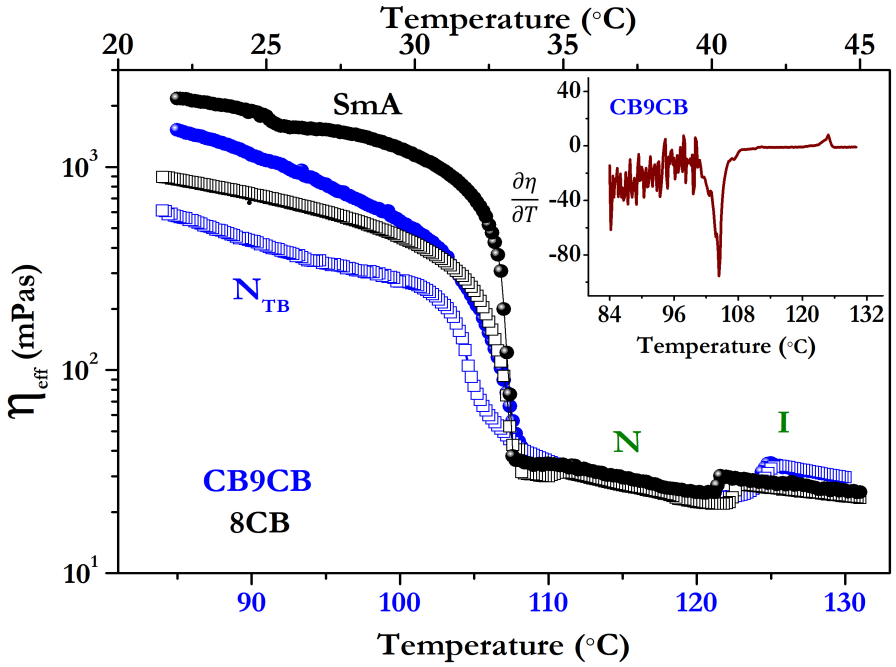

Figure 3.2: Temperature-dependent effective viscosity η_{eff} of CB9CB (blue squares) and 8CB (black spheres) LCs at two different shear rates, namely, $\dot{\gamma} = 100\ \text{s}^{-1}$ (squares) and $\dot{\gamma} = 10\ \text{s}^{-1}$ (circles). (Inset) Variation of $\frac{\partial \eta_{eff}}{\partial T}$ with temperature T of CB9CB.

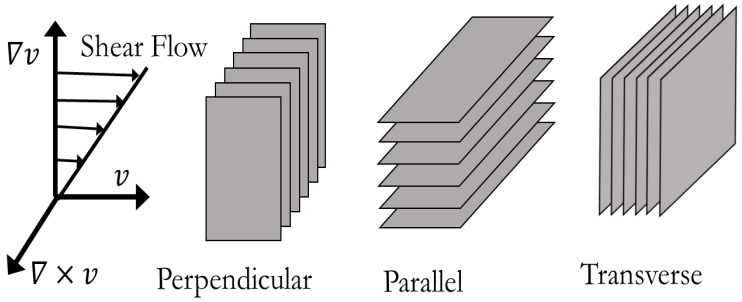

Figure 3.3: Schematic representation of pseudolayer orientations in a shear flow.

of such effect. Interestingly, similar discontinuity is observed in the case of CB9CB at $\dot{\gamma} = 22\text{s}^{-1}$. Further studies are required to confirm the occurrence of such a transition in CB9CB. Nevertheless, the shear rate dependent shear stress σ_{eff} can be fitted to the Herschel-Bulkley (HB) model:

$$\sigma_{eff} = \sigma_y + A\dot{\gamma}^n \tag{3.2}$$

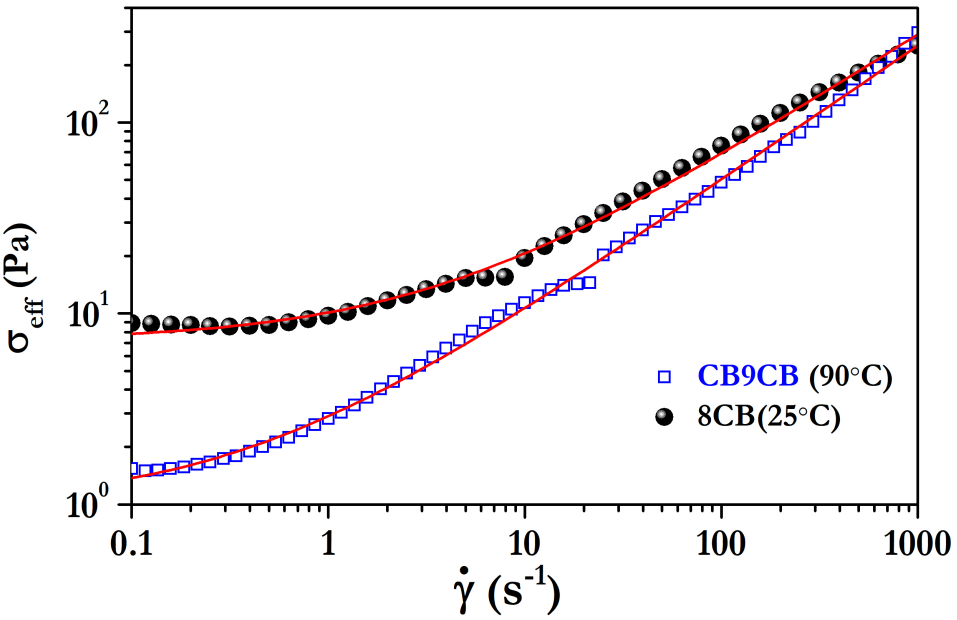

Figure 3.4: Shear rate dependent effective shear stress σ_{eff} at fixed temperatures in CB9CB and in 8CB. The solid lines are theoretical fits to Eq.(3.2).

where σ_y is the yield stress, and A and n are constants. The fit parameters obtained are: $n = 0.71$, $\sigma_y = 1.0$ Pa, $A = 1.9$ for N_{TB} and $n = 0.66$, $\sigma_y = 7.1$ Pa, $A = 2.9$ for SmA phase. The two sets of fit parameters characterising the flow curves of two phases are reasonably close, suggesting they have similar flow behaviour. These two samples have structural similarities; namely, pseudolayer thickness (∼10nm) of N_{TB} is closer to the layer thickness of 8CB (∼2nm). Moreover, both samples exhibit focal conic textures. Hence their generic mechanical responses under shear are similar.

As a next step, we measure the shear modulus $G^*(\omega) = G^{'}(\omega) + iG^{''}(\omega)$. The regime of linear viscoelasticity of N_{TB} is determined by performing oscillatory measurements in which the strain amplitude is varies from $\gamma = 0.01\%$ to $\gamma = 100\%$ at a fixed frequency $\omega = 1$ rad/sec. The strain amplitude dependence can be described by the empirical relation [31],

$$G^{'}(\omega, \gamma) = \frac{G^{'}(\omega, 0)}{1 + \gamma/\gamma_c} \tag{3.3}$$

where γ_c is the critical strain amplitude. As shown in Fig.3.5(a), the critical strain amplitude $\gamma_c = 3.3\%$ and modulus $G^{'}(1, 0) = 391$ Pa, setting the upper limit of the linear

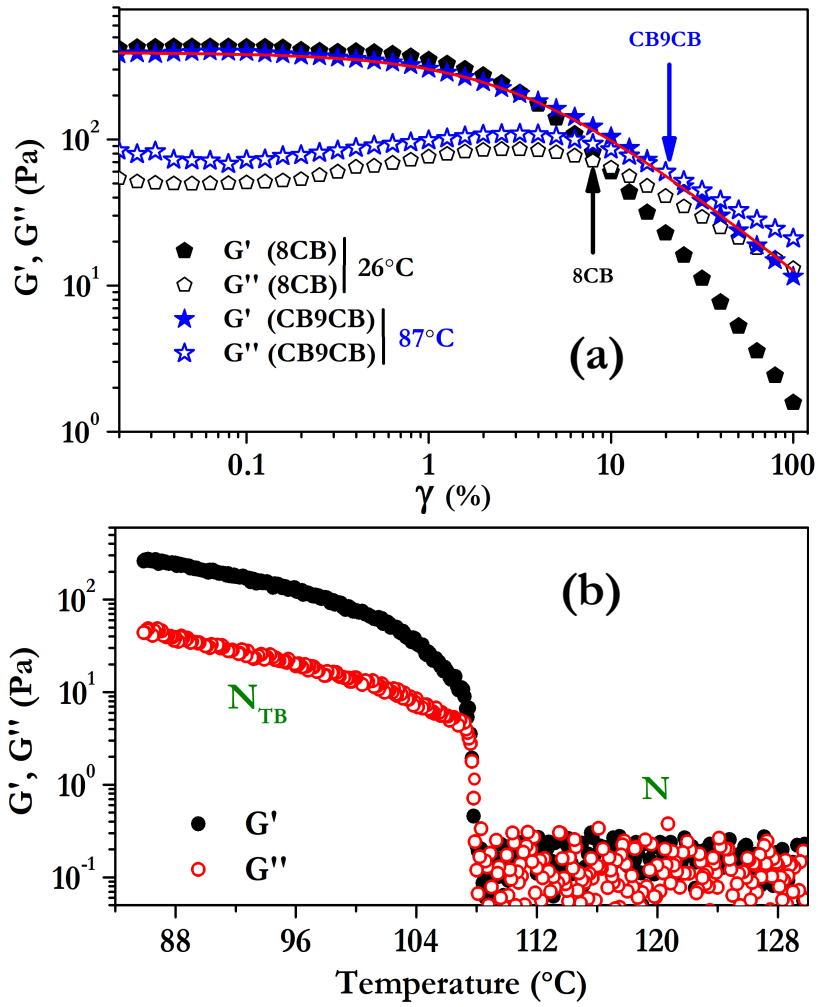

Figure 3.5: (a) Strain amplitude dependence of the storage $G^{'}$ (solid symbol) and loss moduli $G^{''}$ (open symbol) for N_{TB} (T=87°C) and 8CB (T=26°C). The solid line is a theoretical fit to Eq.(3). Arrows indicate crossover strains. (b) Temperature dependence of $G^{'}$ (solid symbol) and loss moduli $G^{''}$ (open symbol) at a fixed strain amplitude $\gamma = 0.1\%$. Measurements are performed at frequency $\omega = 1$ rad/sec.

viscoelastic regime. For comparison we also measured G^{*} of the SmA phase of 8CB as shown in Fig.3.5(a). It is interesting to note that not only the strain dependence but also the magnitudes of the shear moduli of the N_{TB} and SmA are comparable, indicating they have a common structural origin. Further, we have measured the temperature dependence of dynamic moduli of N_{TB} at a fixed shear amplitude $\gamma = 0.1\%$ and observe that $G^{'} > G^{''}$ in the entire N_{TB} phase (Fig.3.5(b)). This is remarkably

similar to that observed in smectics with true mass density wave. Hence, the shear response of the N_{TB} phase can be discussed in analogy with the rheological responses of usual SmA liquid crystals [31]. Like SmA, N_{TB} is solid like in one direction and liquid like in the other two directions. For understanding the shear modulus data, three simplest orientations of the pseudo-layers are considered as shown in Fig.3.3. In perpendicular and parallel orientations the pseudo-layers can slide past each other easily and the N_{TB} phase behaves like a liquid. In transverse orientation, the shear tends to change the pseudo-layer spacing. As a result of which N_{TB} phase shows a viscoelastic solid-like behaviour consequently, $G' > G''$.

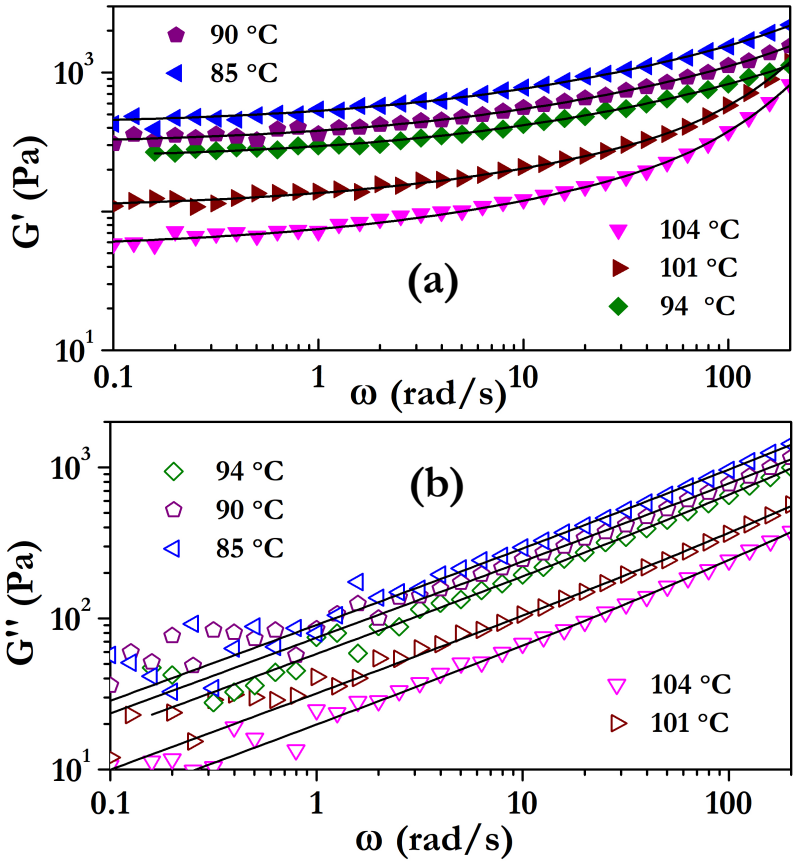

Figure 3.6: Frequency dependence of (a) storage G' (solid symbols) and (b) loss G'' (open symbols) moduli at a few representative temperatures. Solid lines are theoretical fits of Eq.(3.4) and Eq.(3.5) to G' and $G,''$ respectively.

The observed solid-like response of the N_{TB} phase can be explained based on a simple physical model described for defect-mediated cholesteric and smectic LCs. According

to this model, the storage modulus can be expressed as [32]

$$G^{'}(\omega) = G_0 + \beta_d \omega^{1/2} + \beta_0 \omega^2 \tag{3.4}$$

The first term G_0 arises from the elasticity of the static defects [33]. The second term $\beta_d \omega^{1/2}$ arises from the regions of misaligned pseudo-layers in the sample [34]. The last term results from the regions of the sample where the pseudo-layers are parallel to the shear direction. The proportionality constants are given by $\beta_0 \simeq \eta(\gamma_1/K)(p/4\pi)^2$ and $\beta_d = (\pi/24\sqrt{2})\sqrt{(B_{eff}\eta)}$ where γ_1 is the rotational viscosity, η is the effective viscosity and B_{eff} is the compression elastic modulus [34]. In particular, β_d describes

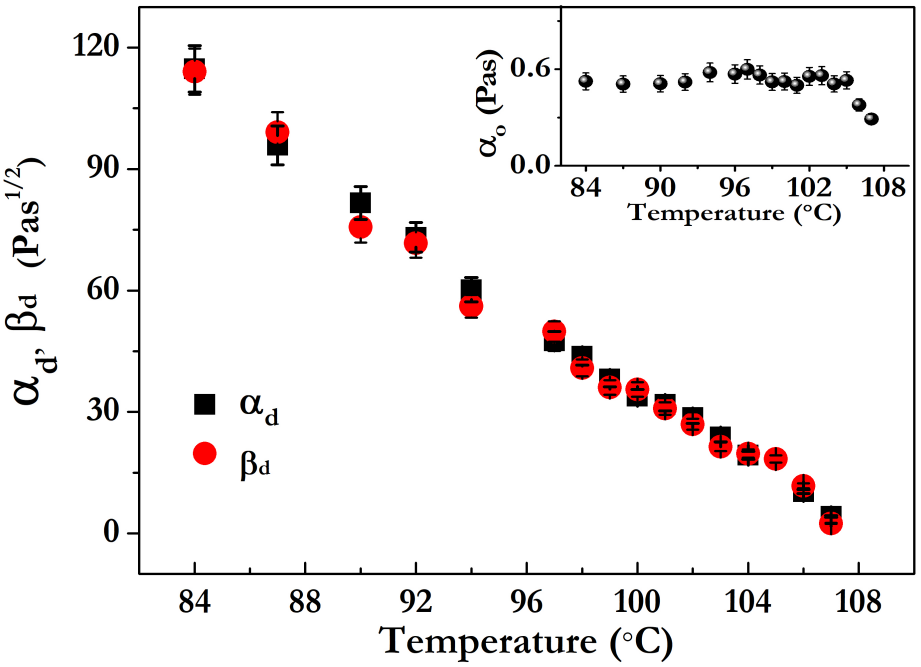

Figure 3.7: Temperature dependence of fit parameters β_d (red spheres) and α_d (black squares). (Inset) Temperature dependence of α_0.

the response of the lamellar regions with the layer normal oriented such that strain involves layer compression. Following similar arguments, the loss modulus can be written as [32]

$$G^{''}(\omega) = \alpha_d \omega^{1/2} + \alpha_0 \omega \tag{3.5}$$

where the first and the second terms arise from the misaligned parts of the samples and the Maxwell-fluid type contribution, respectively. Thus, by measuring β_d and α_0 from the disoriented sample, we can estimate B_{eff}. In order to measure these parameters at

different temperatures we quenched the sample directly from the isotropic to the N_{TB} phase so as to obtain mostly disoriented sample. Figure 3.6 shows some representative plots of $G^{'}(\omega)$ and $G^{''}(\omega)$ at different temperatures in the N_{TB} phase. The parameters obtained by fitting Eq.(3.4) and Eq.(3.5) at different temperatures are shown in Fig.3.7. The fit parameter β_0 is found to be very small (10^{-3}) and does not vary considerably with temperature. It is noted that $\beta_d \simeq \alpha_d$ is expected theoretically and both increase with decreasing temperature. Assuming the whole sample is in the disorientated state, the temperature dependence of B_{eff} can be expressed as

$$B_{eff} = \frac{\beta_d^2}{\alpha_0}\left(\frac{24\sqrt{2}}{\pi}\right)^2 \tag{3.6}$$

Figure 3.8 shows the temperature dependence of calculated B_{eff} in the N_{TB} phase. Just below the N-N_{TB} transition B_{eff} is relatively smaller; 1.5×10^3 Pa (T=105°C) and it increases rapidly to 2×10^6 Pa (T=85°C). The latter value is only one order of magnitude lower that the typical layer compression modulus of SmA phase of 8CB [35]. So far experimentally B_{eff} of very few N_{TB} LCs have been measured. Gorecka *et al.* measured temperature dependence of B_{eff} of a few chiral twist bend nematic LCs including CB7CB using atomic force microscopy technique and reported that B_{eff} is in the range of $10^6 - 10^7$ Pa, comparable to an ordinary SmA LCs. Using a dynamic light scattering technique, Parsouzi *et al.* reported that B_{eff} of N_{TB} phase of an LC made of the multicomponent mixture is in the range of $10^3 - 10^4$ Pa, which is almost three orders of magnitude smaller than the ordinary SmA LCs [23, 25]. Our experiment shows a wide variation of B_{eff}, covering both ranges. Such wide variation of B_{eff} could partly be attributed to the increase in the cone angle θ with decreasing temperature. Based on a crude model $B_{eff} = K_2(2\pi/p)^2 \sin^4\theta$ [25], where θ increases with decreasing temperature [19, 36]. Considering physical parameters for CB7CB such as: $p = 10$nm [19] and $\theta = 10^\circ$ [36] (2°C below N-N_{TB} transition); $p = 8$nm [19] and $\theta = 33^\circ$ [36] (25°C below the transition) and $K_2 = 3$pN, the calculated B_{eff} near two limiting temperatures are given by 1.1×10^3 and 1.6×10^5 Pa. The calculated B_{eff} close to the transition agrees reasonably well with our experiments, but it is smaller by one order of magnitude at far below the transition. This assessment suggests that a mere increase in the cone angle with decreasing temperature can enhance B_{eff} by almost two orders of magnitude.

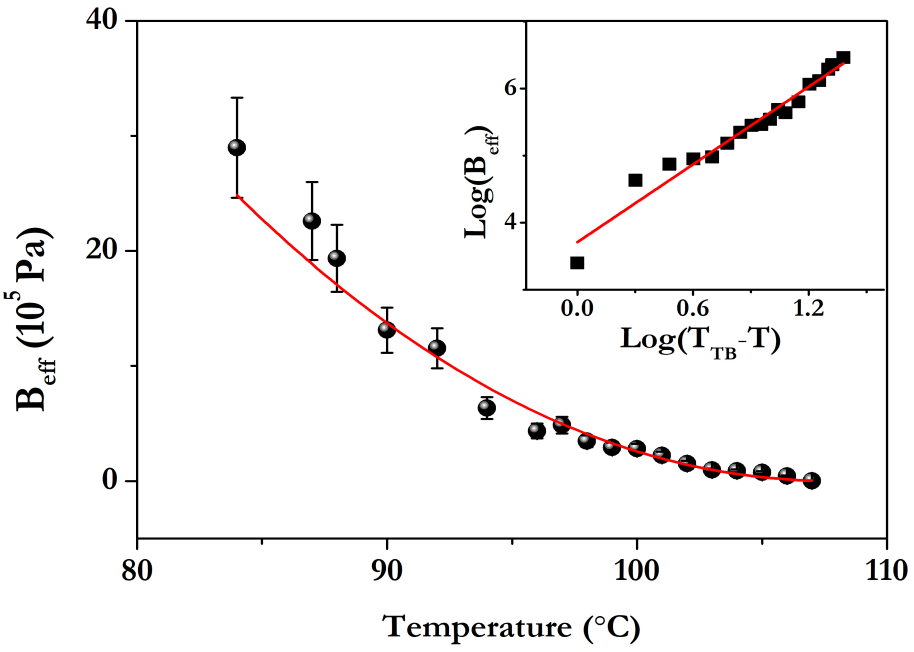

Figure 3.8: Temperature dependence of effective elastic compressional modulus B_{eff}. The solid line is theoretical fit to the equation $B_{eff} \sim (T_{TB} - T)^{\alpha}$, where $\alpha = 2.0 \pm 0.1$. (Inset) variation of B_{eff} with temperature in Log-Log scale.

The temperature dependence of B_{eff} has been predicted theoretically using coarse-grained theoretical models. In analogy with SmA*, Meyer and Dozov defined smectic-like effective pseudo-layer compression and bending elastic constants (K_{33}^N) [22]. Assuming $K_{33}^N < 0$, they predicted $B_{eff} \sim (T_{TB} - T)^2$. Parsouzi *et al.* have developed another model accounting for the helical polarisation field and their coupling with the bend distortion of the director [23]. Considering a small variation in the pseudo-layer spacing and resulting changes in the cone angle and polar order, the theory predicts that there are two regimes of B_{eff}. For temperature (T) sufficiently close to the T_{TB}, $B_{eff} \sim (T_{TB} - T)^3$, whereas for T sufficiently below T_{TB}, the theory gives $B_{eff} \sim (T_{TB} - T)^{3/2}$. Experimentally they found (in a mixture exhibiting N_{TB} phase) that within a relatively small temperature range ($\simeq 6°C$), B_{eff} scales as $(T_{TB} - T)^{3/2}$. To get an estimation of the scaling exponent of B_{eff}, we fit our data to the equation $B_{eff} \sim (T_{TB} - T)^{\alpha}$, with α as a fit parameter as shown in Fig.3.7. Inset shows the variation in the Log-Log scale. We obtain $\alpha = 2.0 \pm 0.1$, which is equal to the scaling

exponent predicted by the "negative elasticity" model of Meyer and Dozov [22].

The temperature dependence of G_0 as shown in Fig.3.9 indicates that the static defects contribute to the mechanical response of the N_{TB} phase similar to that of the SmA phase. Inset of Fig.3.9 shows that it scales with temperature as $G_0 \sim \chi$, where $\chi = (T_{TB} - T)/T_{TB}$ is the reduced temperature. This is slightly faster than that in the case of SmA ($\chi^{0.7}$) [39] as expected in view of the fact that B scales much faster with temperature in the N_{TB} phase.

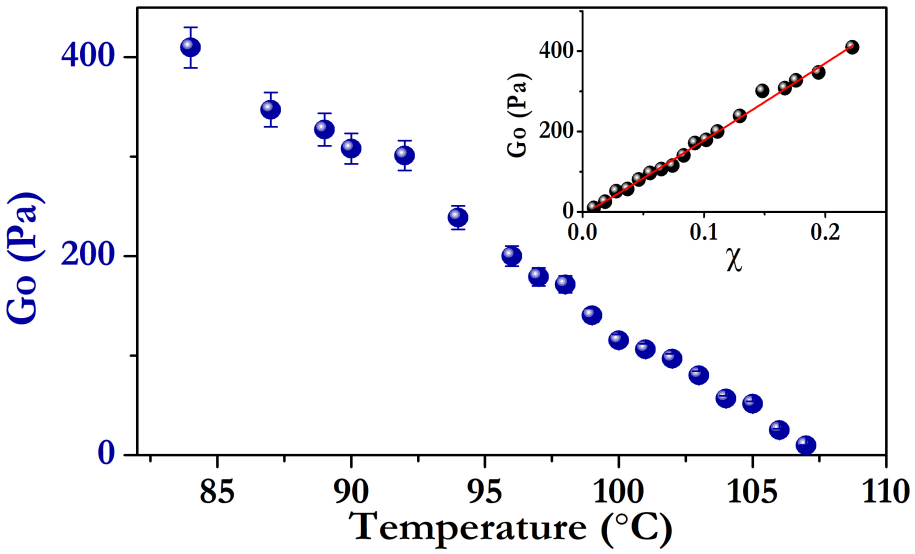

Figure 3.9: Temperature dependence of fit parameter G_0. (Inset) Solid line shows the fit result $G_0 \sim \chi$, where the reduced temperature $\chi = (T_{TB} - T)/T_{TB}$.

3.4 Conclusion

In this work we have presented rheological properties of a N_{TB} LC. The structural rheology of N_{TB} phase is found to be remarkably similar to that of the usual SmA phase of calamitic liquid crystals. Our measurements reveal that in spite of the absence of true mass density wave, N_{TB} LCs are viscoelastic solids similar to many defect mediated lamellar systems. We found that B_{eff} is relatively softer near the N-N_{TB} transition but increases with decreasing temperature to three orders of magnitude more at a much faster rate than the usual SmA LCs. The temperature dependence of B_{eff} agrees well with the prediction of the coarse-grained elastic theories. Thus, our results provide a valuable test of the validity of the proposed theoretical models. The

experiments also offer new perspectives of N_{TB} LCs and open unexplored aspects of rheology of nematic LCs with nanoscale modulation of the director.

References

[1] V. P. Panov, M. Nagaraj, J. K. Vij, Y. P. Panarin, A. Kohlmeier, M. G. Tamba, R. A. Lewis, and G. H. Mehl. *Spontaneous Periodic Deformations in Nonchiral Planar-Aligned Bimesogens with a Nematic-Nematic Transition and a Negative Elastic Constant.* Phys. Rev. Lett. 105, 167801 (2010).

[2] M. Čopič. *Nematic phase of achiral dimers spontaneously bends and twists.* Proc. Natl. Acad. Sci. USA. 110, 15855 (2013).

[3] D. Chen, J. H. Porada, J. B. Hooper, A. Klittnick, Y. Shena, M. R. Tuchbanda, E. Korblova, D. Bedrov, D. M. Walba, M. A. Glaser, J. E. Maclennana, and N. A. Clark. *Chiral heliconical ground state of nanoscale pitch in a nematic liquid crystal of achiral molecular dimers.* Proc. Natl. Acad. Sci. USA. 110, 15931 (2013).

[4] V. Borshch, Y.-K. Kim, J. Xiang, M. Gao, A. Jákli, V. P. Panov, J. K. Vij, C. T. Imrie, M. G. Tamba, G. H. Mehl, and O. D. Lavrentovich. *Nematic twist-bend phase with nanoscale modulation of molecular orientation.* Nat. Commun. 4, 2635 (2013).

[5] L. Beguin, J. W. Emsley, M. Lelli, A. Lesage, G. R. Luckhurst, B. A. Timimi, and H. Zimmermann. *The Chirality of a Twist–Bend Nematic Phase Identified by NMR Spectroscopy.* J. Chem. Phys. B. 116, 7940 (2012).

[6] G. Pajak, L. Longa, and A. Chrzanowska. *Nematic twist–bend phase in an external field.* Proc. Natl. Acad. Sci. USA. 115, E10303 (2018).

[7] J. Zhou, W. Tang, Y. Arakawa, H. Tsuji and S. Aya. *Viscoelastic properties of a thioether-based heliconical twist–bend nematogen.* Phys. Chem. Chem. Phys. 22, 9593 (2020).

[8] R. B. Meyer in *Molecular Fluids*, ed. R. Balian and G. Weill, Les Houches Summer School in Theoretical Physics, Gordon and Breach, New York, vol. XXV-1973, pp.273-373 (1976).

[9] V. L. Lorman and B. Mettout. *Unconventional Mesophases Formed by Condensed Vector Waves in a Medium of Achiral Molecules.* Phys. Rev. Lett. 82, 940 (1999).

[10] V. L. Lorman and B. Mettout. *Theory of chiral periodic mesophases formed from an achiral liquid of bent-core molecules.* Phys. Rev. E. 69, 061710 (2004).

[11] I. Dozov. *On the spontaneous symmetry breaking in the mesophases of achiral banana-shaped molecules.* Europhys. Lett. 56, 247 (2001).

[12] R. J. Mandle, E. J. Davis, C. T. Archbold, S. J. Cowling and J. W. Goodby. *Microscopy studies of the nematic N_{TB} phase of 1,11-di-(1 ″cyanobiphenyl*-4-*yl)undecane.* J. Mater Chem. C. 2, 556 (2014).

[13] M. Cestari, S. Diez-Berart, D. A. Dunmur, A. Ferrarini, M. R. de la Fuente, D. J. B. Jackson, D. O. Lopez, G. R. Luckhurst, M. A. Perez-Jubindo, R. M. Richardson, J. Salud, B. A. Timimi, and H. Zimmermann. *Phase behavior and properties of the liquid-crystal dimer* 1″,7″*-bis(*4*-cyanobiphenyl-*4′*-yl) heptane: A twist-bend nematic liquid crystal.* Phys. Rev. E. 84, 031704 (2011).

[14] D. A. Paterson, J. P. Abberley, W. TA. Harrison, J. MD Storey and C. T. Imrie. *Cyanobiphenyl-based liquid crystal dimers and the twist-bend nematic phase.* Liq. Cryst. 44, 127 (2017).

[15] C. Meyer, G. R. Luckhurst, and I. Dozov. *Flexoelectrically Driven Electroclinic Effect in the Twist-Bend Nematic Phase of Achiral Molecules with Bent Shapes.* Phys. Rev. Lett. 111, 067801 (2013).

[16] N. Sebastián, B. Robles-Hernández, S. Diez-Berart, J. Salud, G. R. Luckhurst, D. A. Dunmur, D. O. López and M. R. de la Fuente. *Distinctive dielectric properties of nematic liquid crystal dimers.* Liq. Cryst. 44, 177 (2017).

[17] N. Trbojevic, D. J. Read, and M. Nagaraj. *Dielectric properties of liquid crystalline dimer mixtures exhibiting the nematic and twist-bend nematic phases.* Phys. Rev. E. 96, 052703 (2017).

[18] S. A. Pardaev, S. M. Shamid, M. G. Tamba, C. Welch, G. H. Mehl, J. T. Gleeson, D. W. Allender, J. V. Selinger, B. Ellman, A. Jákli and S. Sprunt. *Second harmonic light scattering induced by defects in the twist-bend nematic phase of liquid crystal dimers.* Soft Matter. 12, 4472 (2016).

[19] C. Zhu, M. R. Tuchband, A. Young, Min Shuai, A. Scarbrough, D. M. Walba, J. E. Maclennan, C. Wang, A. Hexemer, and N. A. Clark. *Resonant Carbon K-Edge Soft X-Ray Scattering from Lattice-Free Heliconical Molecular Ordering: Soft Dilative Elasticity of the Twist-Bend Liquid Crystal Phase.* Phys. Rev. Lett. 116, 147803 (2016).

[20] Z. Parsouzi, S. M. Shamid, V. Borshch, K. Challa, A. R. Baldwin, M. G. Tamba, C. Welch, G. H. Mehl, J. T. Gleeson, A. Jákli, O. D. Lavrentovich, D. W. Allender, J. V. Selinger and S. Sprunt. *Fluctuation Modes of a Twist-Bend Nematic Liquid Crystal.* Phys. Rev. X. 6, 021041 (2016).

[21] B. Robles-Hernández, N. Sebastián, M. R. de la Fuente, D. O. López, S. Diez-Berart, J. Salud, M. Blanca Ros, D. A. Dunmur, G. R. Luckhurst, and B. A. Timimi. *Twist, tilt, and orientational order at the nematic to twist-bend nematic phase transition of* 1 ″, 9 ″*-bis(*4*-cyanobiphenyl-* 4 ′*-yl) nonane: A dielectric,* ^{2}H *NMR, and calorimetric study.* Phys. Rev. E. 92, 062505 (2015).

[22] C. Meyer and I. Dozov. *Local distortion energy and coarse-grained elasticity of the twist-bend nematic phase.* Soft Matter. 12, 574 (2016).

[23] Z. Parsouzi, S. A. Pardaev, C. Welch, Z. Ahmed, G. H. Mehl, A. R. Baldwin, J. T. Gleeson, O. D. Lavrentovich, D. W. Allender, J. V. Selinger, A. Jakli and S. Sprunt. *Light scattering study of the "pseudo-layer" compression elastic constant in a twist-bend nematic liquid crystal.* Phys. Chem. Chem. Phys. 18, 31645 (2016).

[24] E. Gorecka, N. Vaupotić, A. Zep, D. Pociecha, J. Yoshioka, J. Yamamoto and H.

Takezoe. *A Twist-Bend Nematic (N_{TB}) Phase of Chiral Materials.* Angew. Chem. Int. Ed. 54, 10155 (2015).

[25] S. M. Salili, C. Kim, S. Sprunt, J. T. Gleeson, O. Parri and A. Jákli. *Flow properties of a twist-bend nematic liquid crystal.* RSC Adv. 4, 57419 (2014).

[26] C. R. Safinya, E. B. Sirota, and R. J. Plano. *Nematic to smectic- A phase transition under shear flow: A nonequilibrium synchrotron X-ray study.* Phys. Rev. Lett. 66, 1986 (1991).

[27] J. Ananthaiah, M. Rajeswari, V. S. S. Sastry, R. Dabrowski, and S. Dhara. *Effect of electric field on the rheological and dielectric properties of a liquid crystal exhibiting nematic-to-smectic-A phase transition.* Eur. Phys. J. E. 34, 74 (2011).

[28] M. Praveen Kumar, D. Venkata Sai, and S. Dhara. *Effect of Sm-A short-range order on the activation energies of translational and rotational viscosities of nematic liquid crystals with highly polar molecules.* Phys. Rev. E. 98, 062701 (2011).

[29] R. G. Larson, The Structure and Rheology of Complex Fluids, Oxford University Press, New York pp 480. (1999)

[30] P. Panizza, P. Archambault and D. Roux. *Effects of Shear on the Smectic A Phase of Thermotropic Liquid Crystals.* J. Phys. II France. 5, 303 (1995).

[31] R. H. Colby, C. K. Ober, J. R. Gillmor, R. W. Connelly, T. Doung, G. Galli and M. Laus. *Smectic rheology.* Rheol. Acta. 36, 498 (1997).

[32] L. Ramos, M. Zapotocky, T. C. Lubensky and D. A. Weitz. *Rheology of defect networks in cholesteric liquid crystals.* Phys. Rev. E. 66, 031711 (2002).

[33] R. Bandyopadhyay, D. Liang, R. H. Colby, J. L. Harden, and Robert L. Leheny. *Enhanced Elasticity and Soft Glassy Rheology of a Smectic in a Random Porous Environment.* Phys. Rev. Lett. 94, 107801 (2005).

[34] K. Kawasaki and A. Anuki. *Dynamics and rheology of diblock copolymers quenched into microphase-separated states.* Phys. Rev. A. 42, 3664(R) (1990).

[35] M. Benzekri, J. P. Marcerou, H. T. Nguyen and J. C. Roullion. *Critical behavior of the layer compressional elastic constant B at the smectic- A –nematic phase transition.* Phys. Rev. B. 41, 9032 (1990).

[36] C. Meyer, G. R. Luckhurst and I. Dozov. *The temperature dependence of the heliconical tilt angle in the twist-bend nematic phase of the odd dimer CB7CB.* J. Mater. Chem. C. 3, 318 (2015).

[37] J. A. N. Zasadzinski. *Direct observations of dislocations in thermotropic smectics using freeze-fracture replication.* J. Phys. (Les Ulis, Fr.) 51, 747 (1990).

bibitemmkl M. Kleman. *Defects in liquid crystals.* Rep. Prog. Phys. 52, 555 (1989).

[38] R. L. Leheny, S. Park, R. J. Birgeneau, J. -L. Gallani, C. W. Garland, and G. S. Iannacchione. *Smectic ordering in liquid-crystal–aerosil dispersions. I. X-ray scattering.* Phys. Rev. E. 67, 011708 (2003).

[39] S. Fujii, S. Komura, Y. Ishii, C. -Y. D. Lu. *Elasticity of smectic liquid crystals with focal conic domains.* J. Phys.: Condens. Matter. 23, 235105 (2011).

4

Dynamics of sheared twist bend nematic liquid crystals

4.1 Introduction

In the previous chapter, we studied rheological properties of N_{TB} phase and showed that the flow behaviour of N_{TB} is similar to the SmA phase. Analyzing the shear response with frequency and adapting a simplified physical model for the rheology of defect-mediated lamellar systems, we measure the pseudolayer compression elastic constant B_{eff} and its temperature dependence. In this chapter, we investigate and try to understand from the fundamental perspective, how the novel nematic phase (N_{TB}) responds to the varying shear rate? Is the flow behaviour of N_{TB} Liquid Crystals nematic like or smectic like? To address these questions, we systematically investigated the flow behaviour at varying shear rates.

4.2 Experimental

In this chapter, we used the same compound studied in the previous chapter α, ω-bis(4,4-$'$cyanobiphenyl nonane), known as CB9CB. Texture of the sample in homogeneous and homeotropic cells are shown in Fig.4.1. The textures is very different than conventional nematics and more closure to the focal conic-like textures in smectics. We use a cone-plate measuring system having a plate diameter of 25 mm and a cone angle of 1° for all rheological measurements, and a peltier with a hood used to maintain temperature uniformity of the sample temperature with an accuracy of

0.1°C. A fresh sample was mounted for each measurement, and it was heated above the nematic-isotropic transition temperature and then cooled at the rate 1°C per min to the N_{TB} phase. Before starting the measurements the sample was presheared for 5 minutes at a low shear rate (5 s^{-1}). The phase transition temperatures (N and N_{TB}) of the mounted samples in the Rheometer were ascertained from the temperature-dependent viscosity that shows characteristic change at the phase transitions. The stress relaxation measurement data was collected at each second for 60 minutes.

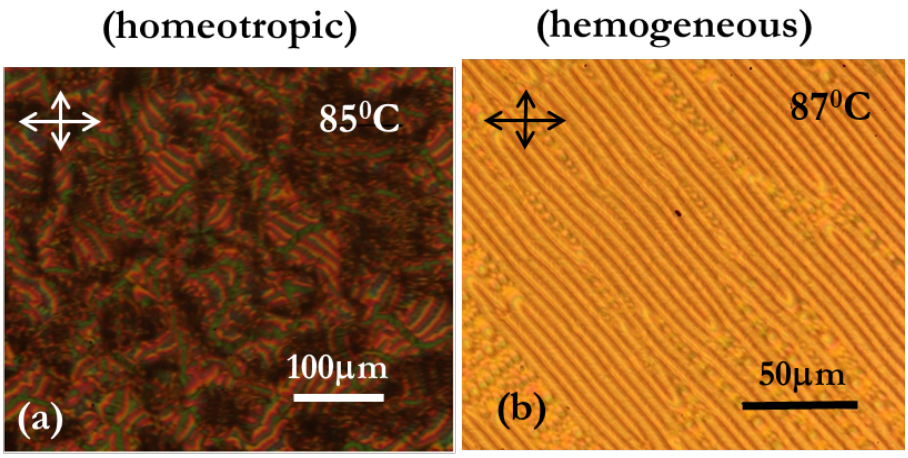

Figure 4.1: Polarizing optical microscope textures of N_{TB} phase in a (a) homeotropic (b) and in a homogeneous cells.

4.3 Results and discussions

Figure 4.2 shows the flow curves at different temperatures in the N_{TB} phase in log-log scale. The data in the linear scale from the starting shear rate $\dot{\gamma} = 1$ s^{-1} is shown in the appendix (Fig.4.10). At a fixed temperature (Fig.4.2), initially the stress (σ) increases with shear rate ($\dot{\gamma}$) and at a particular shear rate ($\dot{\gamma_L}$), it changes slope and tends to saturate, showing a near-plateau. At a certain higher shear rate ($\dot{\gamma_U}$), the stress jumps discontinuously to a larger value from the near-plateau and continue to increase with increasing shear rate. Similar discontinuous transition is also observed with decreasing shear rate. But the transition takes place at a slightly higher shear rate, showing a clear thermal hysteresis, a typical characteristic of discontinuous transition (inset to Fig.4.3). At higher temperatures the discontinuous transition takes place at higher

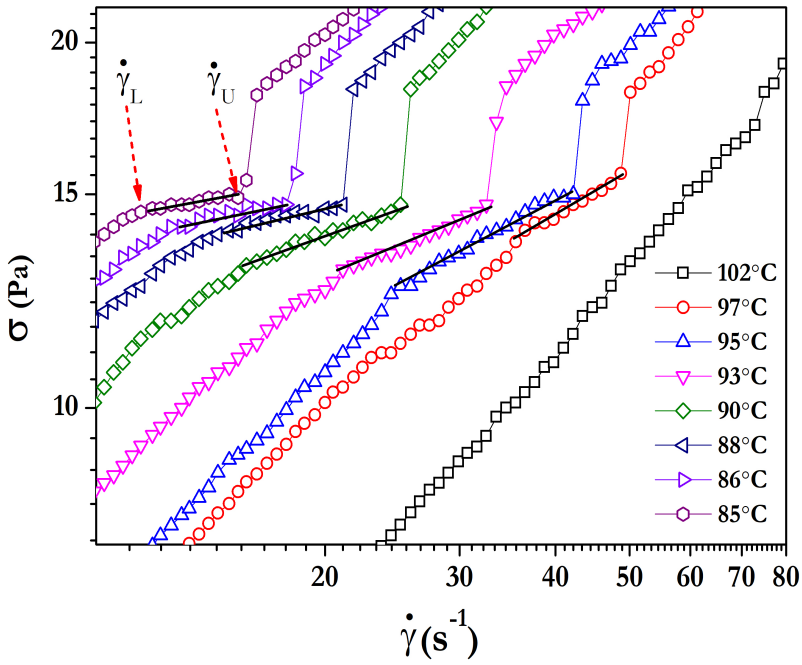

Figure 4.2: Flow curves at different temperatures in the N_{TB} phase of CB9CB LC. Solid lines show best fits to $\sigma \sim \dot{\gamma}^{\alpha}$.

shear rates. The variations of the limiting shear rates, $\dot{\gamma_L}$ and $\dot{\gamma_U}$ with temperature are shown in Fig.4.3. We observe three distinct regimes in this diagram. The transition from region-I to region-II takes place continuously whereas from the region-II to the region-III, the transition takes place discontinuously. Beyond T$\simeq$ 97 °C the near-plateau is not observed although the stress jump is observed till T$\simeq$ 103 °C.

Figure 4.4(a) shows the variation of stress σ with the shear rate in region-I. It shows a Non-Newtonian flow behaviour and the data can be fitted to the scaling relation $\sigma \sim C_1(T)\dot{\gamma}^{1/2}$, where $C_1(T)$ is a proportionality constant that varies with temperature. This also means that the shear viscosity decreases as $\eta \sim \dot{\gamma}^{-1/2}$, exhibiting a shear thinning behaviour. The constant $C_1(T)$ decreases with increasing temperature and it can be fitted to $C_1(T) \sim (T_c - T)^{0.53\pm0.01}$, where T_c (=103 °C) is the temperature above which the discontinuous transition is not detectable. It is noticed that T_c is about 5°C below the N to N_{TB} transition temperature (108 °C).

The near-plateau has a finite slope and it can be fitted to a power law: $\sigma \sim \dot{\gamma}^{\alpha}$

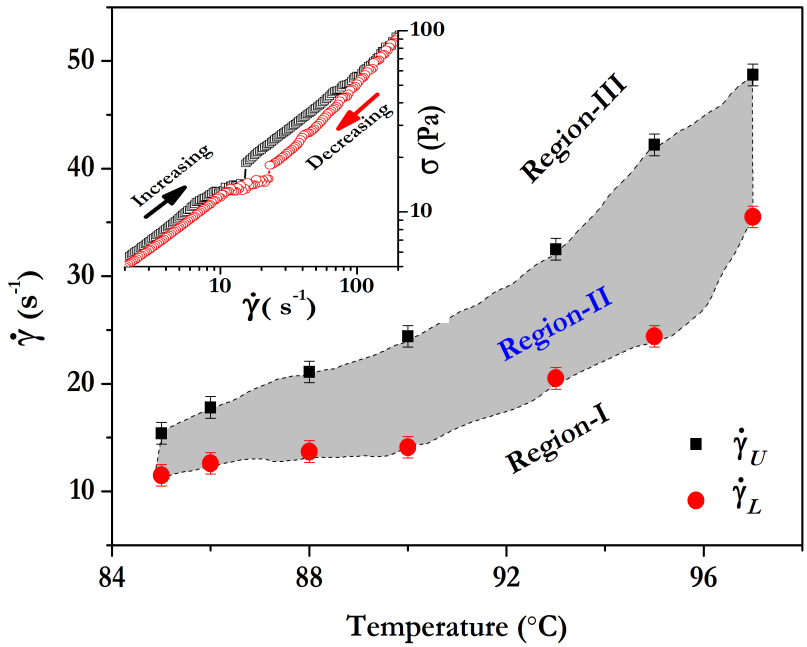

Figure 4.3: Temperature variation of the onset shear rate $\dot{\gamma}_L$ (red circles) and the terminal shear rate $\dot{\gamma}_U$ (black squares) of the near-plateau as shown in Figure 4.3. Dotted curve is a guide to the eye. Inset shows the hysteresis of the transition at T=85°C. The difference between the two shear rates in heating and cooling at the transition is $\Delta\dot{\gamma} = \dot{\gamma}_U - \dot{\gamma}_L = 8$ s^{-1}.

where α is an exponent that increases linearly with the temperature from 0.1 to 0.4 as shown in Fig.4.5(a). Figure 4.5(b) shows the variation of stress jump $\Delta\sigma$ with temperature. It decreases approximately from 3.5 Pa to 1 Pa as the temperature is increased to T_c = 102 °C. Similar near-plateau has been observed in shear-banding micellar aqueous solutions of surfactant (cetyl trimethylammonium tosulate (CTAT)) as a function of salt concentration [28]. It was explained, taking into account the effect of coupling of flow-concentration [28–38] and flow-microstructures [39]. Ours is a single component thermotropic LC hence the possibility of flow-concentration coupling is ruled out. Similar stress-plateau has also been observed in wormlike micellar systems very near to the nematic to isotropic phase transition, wherein the low (isotropic) and high viscous (nematic) regions are separated, forming shear-bands [33]. But in our system, the near-plateau is observed below 100°C which is about 8°C below the N-N_{TB} phase transition temperature. Hence, the shear banding or mixing of N and

N_{TB} phases can also be ruled out.

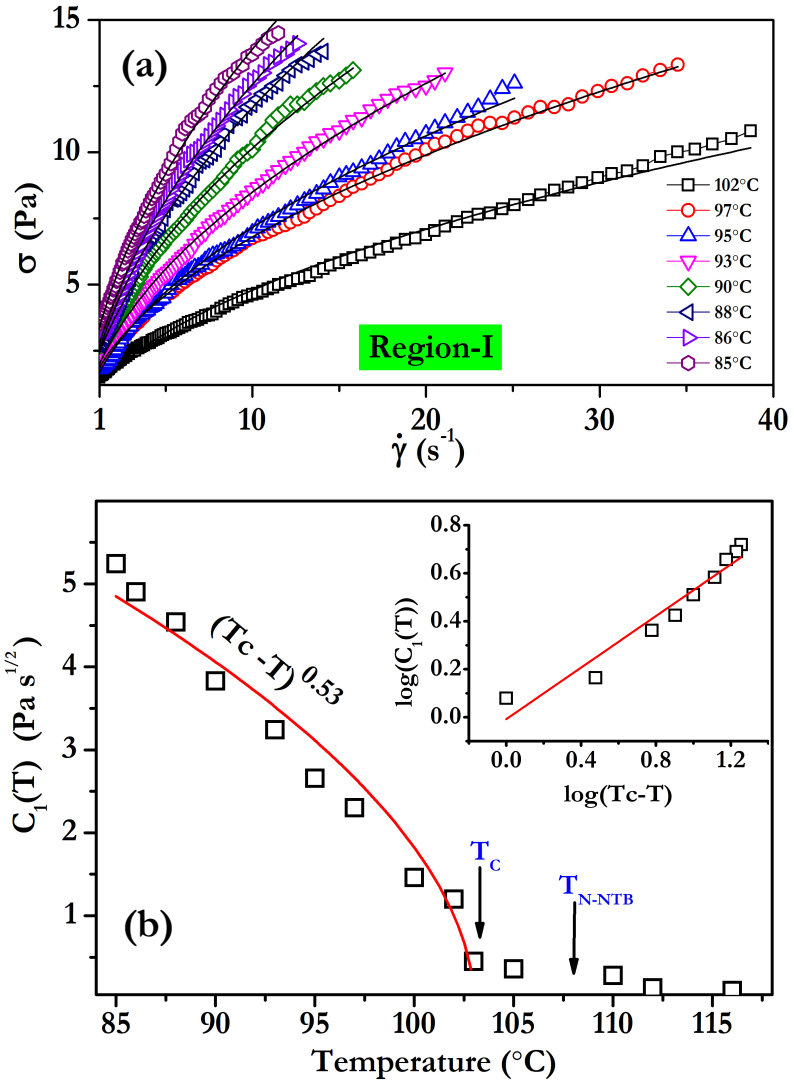

Figure 4.4: (a) Variation of σ with $\dot{\gamma}$ in region 1 at different temperatures in the N_{TB} phase. Solid lines are best fits to $\sigma \sim C_1(T)\sqrt{\dot{\gamma}}$. (b) Temperature variation of slope $C_1(T)$. Solid red curve is a least square fit to $C_1(T) \sim (T_c - T)^{0.53\pm0.01}$ with $T_c = 103°C$. Both temperatures, T_c and nematic to N_{TB} transition (T_{N-NTB}) are marked by vertical arrows. Inset shows the log-log plot.

In region-III, the N_{TB} phase shows a Newtonian flow behaviour (Fig.4.6(a)) and the stress can be fitted to the scaling relation $\sigma \sim C_3(T)\dot{\gamma}$, where $C_3(T)$ is equivalent to the effective viscosity η_{eff}. Figure 4.6(b) shows that $C_3(T)$ decreases with increasing temperature as expected.

The effect of shear in the SmA phase of 4-cyano-4'-octylbiphenyl (8CB) liquid crystal

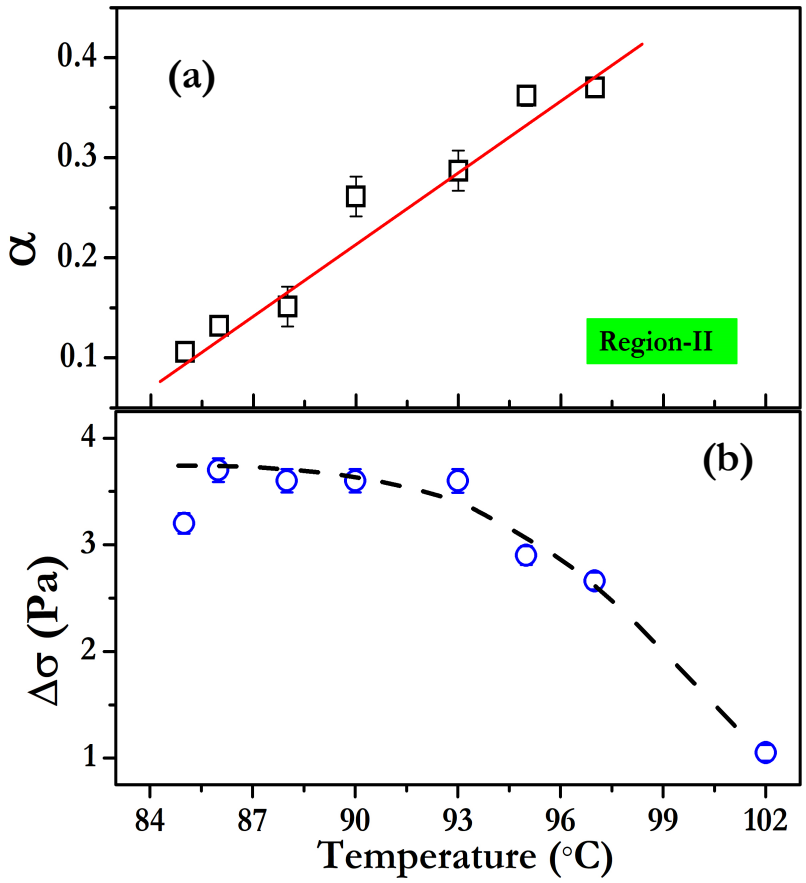

Figure 4.5: (a) Temperature variation of α in the near-plateau. Solid red line is a best fit to the data. (b) Temperature variation of the stress jump $\Delta\sigma$ in the N_{TB} phase dashed curve is drawn as a guide to the eye.

has been studied using a stress-controlled rheometer, in which the stress was applied and the strain was measured [31]. Interestingly, the shear response of the N_{TB} phase is somewhat similar to that of the SmA phase of 8CB LC, except the different regions in N_{TB} appear at much higher shear rates. From the simultaneous rheo-x-ray investigations of the 8CB LC, two steady state orientations of lamellae were identified in a certain temperature range of the SmA phase. In the low shear-rate regime (equivalent to region-I), multilamellar cylinders are formed which are oriented along the flow direction as shown schematically in Fig.4.7(a) and the system shows a non-Newtonian flow behaviour namely, $\sigma \sim \sqrt{\dot{\gamma}}$, similar to that is observed in the present sample. At high shear-rate regime (equivalent to region-III), SmA layers are oriented perpendic-

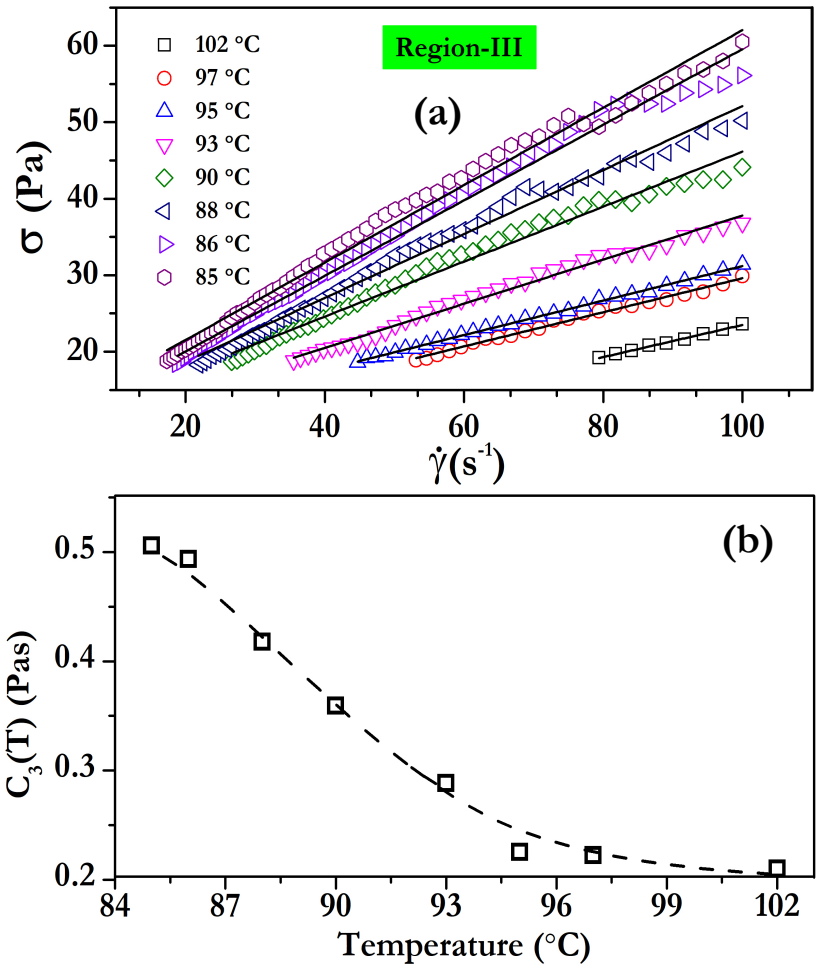

Figure 4.6: (a) Variation of stress σ with $\dot{\gamma}$ in region-III at different temperatures in the N_{TB} phase. Solid lines are best fits to $\sigma \sim C_3(T)\dot{\gamma}$. (b) Temperature variation of $C_3(T)$ dashed curve is drawn as a guide to the eye

ular to the shear plane as shown in Fig.4.7(b) and $\sigma \sim \dot{\gamma}$. In the intermediate shear rate range, a diphasic region was observed where these two states coexist.

The SmA phase of 8CB LC has a layer thickness ~ 2 nm with a mass density wave, whereas the N_{TB} phase of CB9CB LC has a pseudolayer structure (pitch ~ 9 nm) without a true mass density wave [23]. Moreover, the pseudolayers of N_{TB} phase exhibits compression elastic modulus whose value is one to two orders of magnitude lower than that of the SmA phase [26]. Considering the structural similarities between the SmA and N_{TB} phases, it is more likely that in region-I of the N_{TB} phase, the pseudolayers

form multi-pseudolamellar cylinders which are oriented along the flow direction and in region-III the pseudolayers are oriented perpendicular to the shearing plates as shown schematically in Fig.4.7. Region-II is diphasic region wherein the pseudolayers and multi-pseudolamellar cylinders coexist. At higher temperatures (> 102°C) and high shear rates (> 80 s^{-1}), the N_{TB} phase may completely transit to N phase. However, confirmation of such dynamic features require further rheo-microscopy or rheo-x-ray investigations.

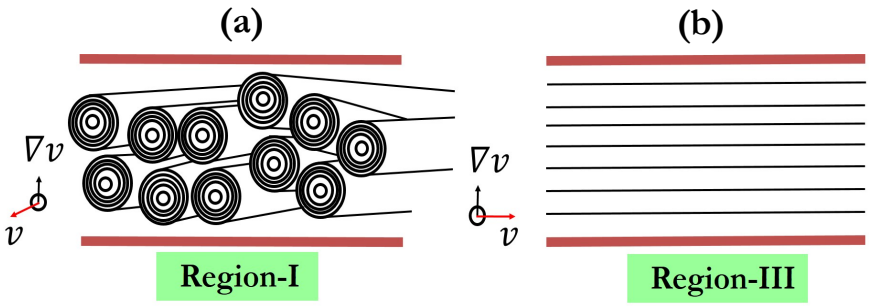

Figure 4.7: Schematic diagram showing (a) multi-pseudolamellar cylinders in region-I and (b) parallel pseudolayers in region-III.

The existence of stress plateau is often regarded as a signature of shear-banded inhomogeneous stationary flows resulting mechanical instability [37]. The time-dependent stress in this regime usually shows dynamic relaxation [38, 40]. In order to study the stress dynamics in the near-plateau region we have measured the time dependence of stress under a steady shear at a few temperatures. Figure 4.8(a) shows the time-dependent stress profiles at some selected shear rates, namely $\dot{\gamma} = 5, 10, 12, 15, 18$ s^{-1} and at a fixed temperature (T= 85°C) in the N_{TB} phase. Among these shear rates, 5 s^{-1} lies just below and shear rate 18 s^{-1} lies just above the near-plateau regime. The stress values (σ) for these two shear rates (beyond the near-plateau regime) is almost independent of time. When the shear rate is increased to 10 s^{-1}, σ shows oscillation which looks periodic and the patterns change at higher shear rates ($\dot{\gamma}$ = 12 and 15 s^{-1}). It may be mentioned that the amplitude of the oscillation is much larger than the limiting stress value of the plate-cone geometry (24 mPa.s^{-1}) therefore, the stress signal is due to the dynamic response of the sample. The Fourier power spectrums of the signals for the shear rates, $\dot{\gamma} = 10, 12$ and 15 s^{-1} are shown in Fig.4.8(b). The power spectrum at 10 s^{-1} shows a fundamental mode (ω) and its higher harmonics.

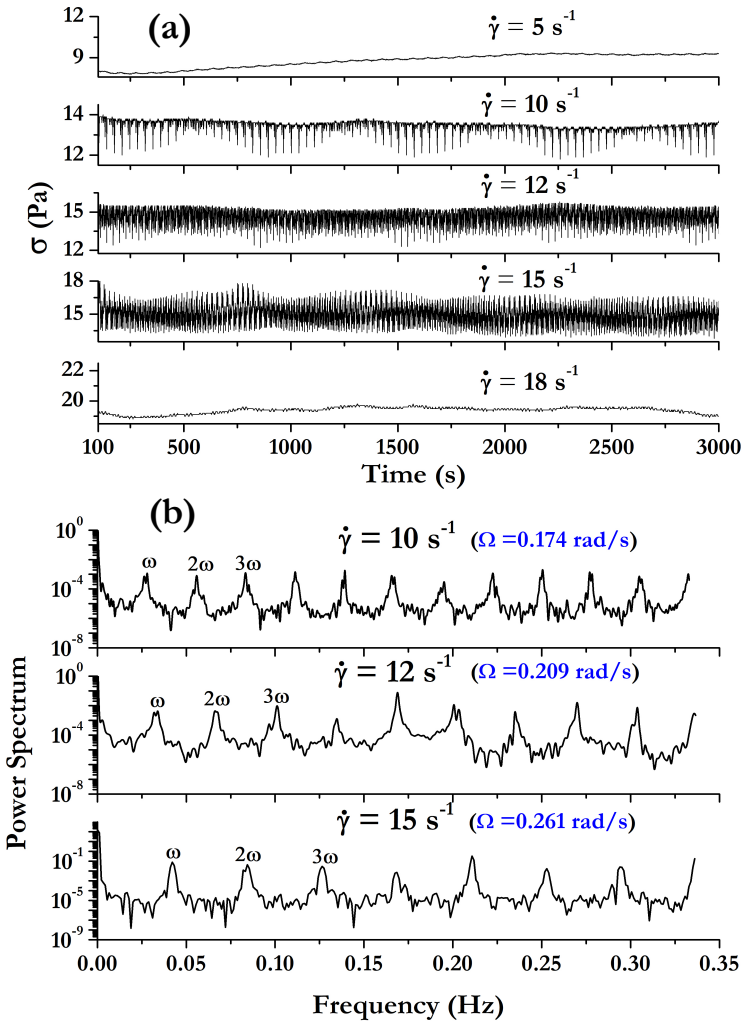

Figure 4.8: (a) Stress dynamics in the near-plateau regime at T=85°C. The stress oscillation time series at different shear rates. Shear rates $\dot{\gamma} = 10, 12, 15$ s^{-1} lies within the stress plateau. $\dot{\gamma} = 5$ and 18 s^{-1} lies just below and above the stress-plateau, respectively (see Fig.4.3). (b) Corresponding Fourier power spectrum. A few harmonics of the fundamental frequency ω $(= 2\pi f)$ are labelled. The fundamental frequencies ω for the shear rates $10, 12, 15$ s^{-1} are 0.17, 0.21 and 0.27 rad/s, respectively. Shearing frequencies calculated using $\Omega = \dot{\gamma}\tan(\alpha)$ are also shows in blue within brackets next to the shear rates.

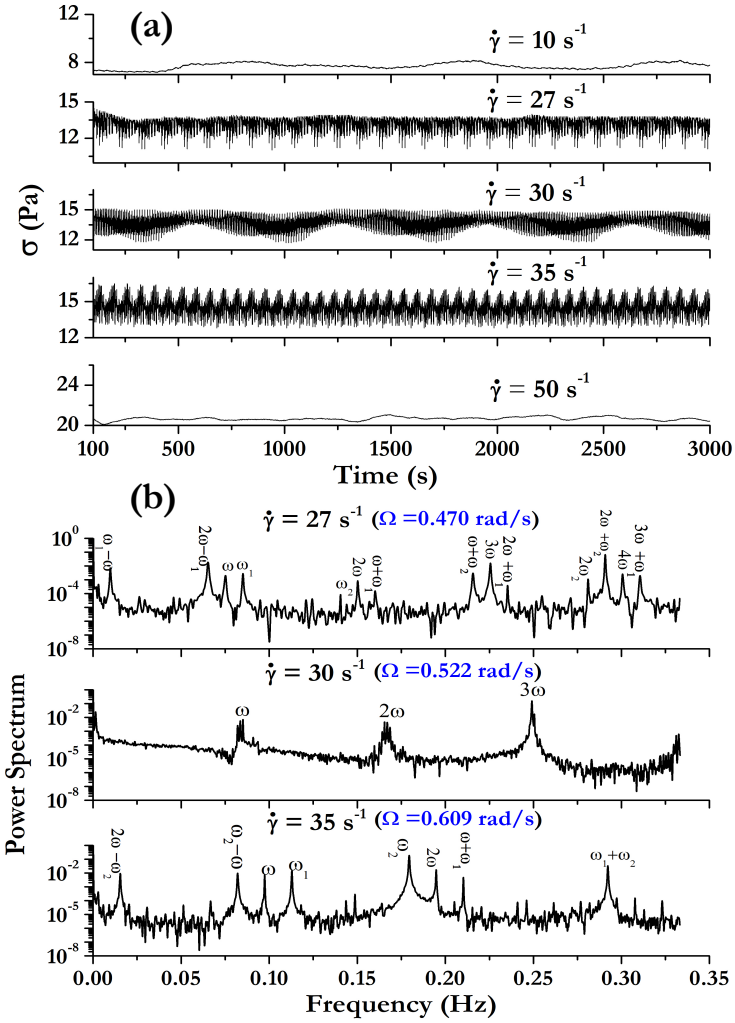

Figure 4.9: (a) Stress dynamics in the near-plateau regime at T=95°C. The stress oscillation time series at different shear rates. $\dot{\gamma} = 27, 30, 35$ s^{-1} lies within the stress near-plateau. $\dot{\gamma} = 10$ and 50 s^{-1} lies below and above the stress plateau, respectively (see Fig. 4.3). (b) Corresponding Fourier power spectrum. A few harmonics of the fundamental frequency ω $(= 2\pi f)$ are labelled. The fundamental frequencies ω for the shear rates $27, 30, 35$ s^{-1} are 0.47, 0.53 and 0.61 rad/s, respectively. Shearing frequencies calculated using $\Omega = \dot{\gamma}\tan(\alpha)$ are shown within brackets next to the shear rates.

The frequency ω of the fundamental mode is shifted to higher values with increasing shear rate. For example, the frequencies ($\omega = 2\pi f$) for the fundamental modes for shear rates, $\dot{\gamma} = 10, 12$ and 15 s^{-1} are 0.17 rad/s, 0.21 rad/s and 0.27 rad/s, respectively. The driving angular frequency (Ω) of the plate-cone system for a given shear rate $\dot{\gamma}$, is given by $\Omega = \dot{\gamma}\tan(\alpha)$, where α (=1°) is the cone angle. The calculated driving frequencies Ω for the shear rates 10, 12 and 15 s^{-1} are 0.17, 0.21 and 0.26 rad/s, respectively which are almost equal to the respective fundamental frequencies i.e., $\Omega = \omega$ (Fig.4.8(b)). This suggests that the stress oscillations in the near-plateau is driven by the shearing force.

Figure 4.9 shows time-dependent stress profile and the corresponding power spectra at a higher temperature (T=95°C). Shear rates 10 and 50 s^{-1} lie below and above the near-plateau regime and the corresponding stress values are almost constant (Fig.4.9(a)). Shear rates 27, 30 and 35 s^{-1} are well within the range of near-plateau. The stress signal corresponding to $\dot{\gamma} = 27$ s^{-1} looks periodic (Fig.4.9(a)) with two modes but the power spectrum shows that there is a fundamental frequency ω, which is identified as equal to the shearing frequency Ω and also its higher harmonics e.g., 2ω, 3ω and 4ω. Apart from these, there are two more frequencies ω_1, ω_2 and their higher harmonics, and there are also several linear combinations of frequencies such as $\omega + \omega_1$, $\omega + \omega_2$, $\omega_1 + 2\omega$, $2\omega + \omega_2$, $3\omega + \omega_1$, $2\omega - \omega_1$ and $\omega_1 - \omega$ etc. These additional features are the hallmark of quasiperiodic signal. The stress oscillation corresponding to the shear rate 30 s^{-1} apparently looks periodic (Fig. 4.9(a)). The stress oscillation at shear rate 35 s^{-1} and the corresponding power spectrum shows that the oscillation is quasiperiodic and apart from the three primary frequencies (ω, ω_1, ω_2), there are linear combination of frequencies such as $\omega + \omega_1$, $\omega_1 + \omega_2$, $\omega_2 - 2\omega_1$ and $\omega - \omega_2$. We also performed experiments at a few higher temperatures and the overall the stress response was quasiperiodic.

Theoretically dynamics of shared nematogenic fluids considering the coupling of the order parameter to flow have been studied based on the relaxation equation for the alignment tensor [41–44]. It was shown that in the absence of flow alignment the dynamic responses are due to the spatiotemporal fluctuations of the stress [41]. Also a variety of symmetry breaking transient states with out-of-plane director configura-

tion showing complicated periodic or regular chaotic states have been predicted [45]. Recently nematic hydrodynamic incorporating spatial inhomogeneity under controlled shear rate and shear stress has been studied numerically [42]. For a certain range of tumbling parameters the model predicts, three distinct states or phases, namely periodic, spatiotemporally chaotic and aligned. In the N_{TB} phase, we observe some of the features of the stress dynamics predicted in the above references. The similarities of our experimental results with those of the theories are exciting and it encourages for further experimental work using rheo-optical and rheo-x-ray scattering techniques.

4.4 Conclusion

In conclusion we have studied the effect of steady shear on the dynamics of a twist-bend nematic liquid crystal. We observe three dynamic regimes in the $\dot{\gamma}$-T diagram. The N_{TB} liquid crystal shows a continuous transition from region-I to region-II and a discontinuous transition from region-II to region-III with a finite stress jump. With increasing temperature, the stress jump decreases and the transition is not detectable beyond a particular temperature. The stress is nearly plateaued in region-II. The flow behaviour in region-I and region-II is non-Newtonian with characteristic exponents. However, in region-III the flow behaviour is Newtonian. The overall flow behaviour in region-I and region-III are similar to that of the SmA phase of 8CB LCs. Thus, under shear, the pseudolayers of N_{TB} behave like a usual SmA layers. In the near-plateau region we have observed both regular periodic and quasi-periodic stress oscillations which are somewhat similar to those were reported in wormlike micellar systems. It appears that with increasing temperature our system moves from regular periodic to quasi-periodic state. Our experiments show some striking similarities with the dynamic stress response of nematogenic fluids predicted recently. Our study unveils the flow dynamics of twist-bend nematic liquid crystals which are promising for further experimental and theoretical studies.

4.5 Appendix

Figure 4.10 shows the variation of shear stress σ with shear rate $\dot{\gamma}$ in the linear scale. Different regimes are marked as described in the main text. We would like to mention that inspired by our experiments I.E.Kates proposed a qualitative theoretical model for understanding our experiment. He explained the scaling behaviour of these three regimes using coarse grain theory of smectics with larger scales [46].

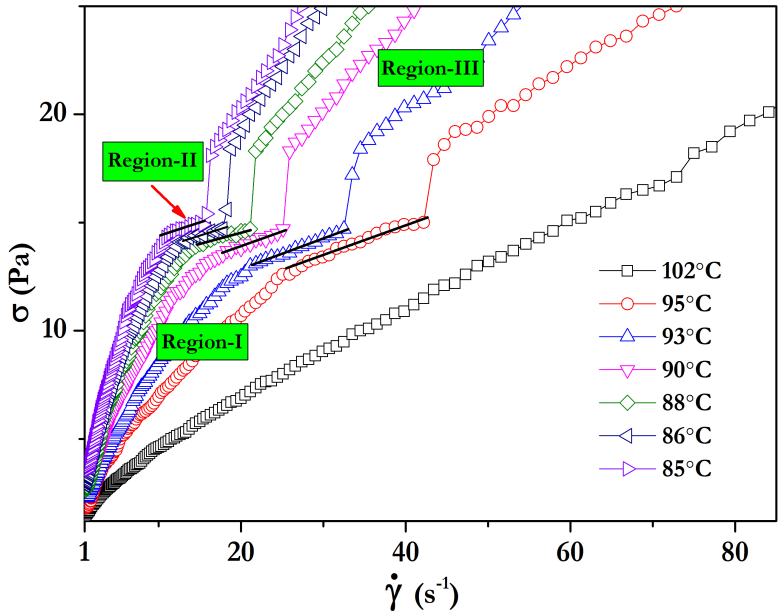

Figure 4.10: Shear-rate dependent shear-stress in linear scale, from $\dot{\gamma} = 1$ s^{-1} to 85 s^{-1} at different temperature in the N_{TB} phase.

References

[1] R. G. Larson. *The structure and rheology of complex fluids*, Oxford University Press, New York (1999).

[2] T. Divoux, M. A. Fardin, S. Manneville and S. Lerouge. *Shear Banding of Complex Fluids.* Annu. Rev. Fluid Mech. 48, 81 (2016).

[3] J. M. Krishnan, A. P. Deshpande and P. B. Sunil Kumar. *Rheology of complex fluids.* Springer, New York Dordrecht Heidelberg London (2010).

[4] S. M. Fielding. *Complex dynamics of shear banded flows.* Soft Matter. 3, 1262 (2007).

[5] P. G. de Gennes. *The Physics of Liquid Crystals.* Oxford University Press: Oxford, England, (1974).

[6] S. Chandrasekhar. *Liquid Crystals.* Cambridge University Press, Cambridge, England (1992).

[7] L. M. Blinov and V. G. Chigrinov. *Electrooptic effects in liquid crystal materials.* Springer-Verlag, Berlin (1994).

[8] C. R. Safinya, E. B. Sirota, and R. J. Plano. *Nematic to smectic- A phase transition under shear flow: A nonequilibrium synchrotron x-ray study.* Phys. Rev. Lett. 66, 1986 (1991).

[9] O. Henrich, K. Stratford, D. Marenduzzo, P. V. Coveney and M. E. Cates. *Rheology of lamellar liquid crystals in two and three dimensions: a simulation study.* Soft Matter. 8, 3817 (2012).

[10] J. Ananthaiah, R. Sahoo, M. V. Rasna, and S. Dhara. *Rheology of nematic liquid crystals with highly polar molecules.* Phys. Rev. E. 89, 022510 (2014).

[11] K. Negita, M. Inoue, and S. Kondo. *Dielectric study on the shear-induced structural changes in the nematic and the smectic- A phases of* 4-*n*-octyl-4′-*cyanobiphenyl (8CB).* Phys. Rev. E. 74, 051708 (2006).

[12] M. R. Alcantara, and J. Vanin. *Rheological properties of lyotropic liquid crystals.* Colloids Surf. A. Physicochem and Eng. Asp. 97(2) 151 (1995).

[13] R. Mezzenga, C. Meyer, C. Servais, A. I. Romoscanu, L. Sagalowicz, and R. C. Hayward. *Shear Rheology of Lyotropic Liquid Crystals: A Case Study.* Langmuir. 21, 3322 (2005).

[14] W. H. Han and A. D. Rey. *Simulation and validation of temperature effects on the nematorheology of aligning and nonaligning liquid crystals.* J. Rheol. 39, 301 (1995).

[15] I. Dozov. *On the spontaneous symmetry breaking in the mesophases of achiral banana-shaped molecules.* Europhys. Lett. 56, 247 (2001).

[16] V. P. Panov, M. Nagaraj, J. K. Vij, Yu. P. Panarin, A. Kohlmeier, M. G. Tamba, R. A. Lewis, and G. H. Mehl. *Spontaneous Periodic Deformations in Nonchiral Planar-Aligned Bimesogens with a Nematic-Nematic Transition and a Negative Elastic Constant.* Phys. Rev. Lett. 105, 167801 (2010).

[17] V. Borshch, Y.-K. Kim, J. Xiang, M Gao, A. Jákli, V. P. Panov, J. K. Vij, C. T. Imrie, M. G. Tamba, G. H. Mehl, and O. D. Lavrentovich. *Nematic twist-bend phase with nanoscale modulation of molecular orientation.* Nat. Commun. 4, 2635 (2013).

[18] M. Čopič. *Nematic phase of achiral dimers spontaneously bends and twists.* Proc. Natl. Acad. Sci. USA. 110, 15855 (2013).

[19] D. Chen, J. H. Porada, J. B. Hooper, A. Klittnick, Y. Shena, M. R. Tuchbanda, E. Korblova, D. Bedrov, D. M. Walba, M. A. Glaser, J. E. Maclennana, and N.

A. Clark. *Chiral heliconical ground state of nanoscale pitch in a nematic liquid crystal of achiral molecular dimers.* Proc. Natl. Acad. Sci. USA. 110, 15931 (2013).

[20] C. Meyer, G. R. Luckhurst, and I. Dozov. *Flexoelectrically Driven Electroclinic Effect in the Twist-Bend Nematic Phase of Achiral Molecules with Bent Shapes.* Phys. Rev. Lett. 111, 067801 (2013).

[21] Z. Parsouzi, S. M. Shamid, V. Borshch, K. Challa, A. R. Baldwin, M. G. Tamba, C. Welch, G. H. Mehl, J. T. Gleeson, A. Jakli, O. D. Lavrentovich, D. W. Allender, J. V. Selinger and S. Sprunt. *Fluctuation Modes of a Twist-Bend Nematic Liquid Crystal.* Phys. Rev. X. 6, 021041 (2016).

[22] Z. Parsouzi, S. A. Pardaev, C. Welch, Z. Ahmed, G. H. Mehl, A. R. Baldwin, J. T. Gleeson, O. D. Lavrentovich, D. W. Allender, J. V. Selinger, A. Jakli and S. Sprunt. *Light scattering study of the "pseudo-layer" compression elastic constant in a twist-bend nematic liquid crystal.* Phys. Chem. Chem. Phys. 18, 31645 (2016).

[23] C. Zhu, M. R. Tuchband, A. Young, Min Shuai, A. Scarbrough, D. M. Walba, J. E. Maclennan, C. Wang, A. Hexemer, and N. A. Clark. *Resonant Carbon K-Edge Soft X-Ray Scattering from Lattice-Free Heliconical Molecular Ordering: Soft Dilative Elasticity of the Twist-Bend Liquid Crystal Phase.* Phys. Rev. Lett. 116, 147803 (2016).

[24] C. Meyer and I. Dozov. *Local distortion energy and coarse-grained elasticity of the twist-bend nematic phase.* Soft Matter. 12, 574 (2016).

[25] S. M. Salili, C. Kim, S. Sprunt, J. T. Gleeson, O. Parri and A. Jakli. *Flow properties of a twist-bend nematic liquid crystal.* RSC Adv. 4, 57419 (2014).

[26] M. Praveen Kumar, P. Kula, and S. Dhara. *Smecticlike rheology and pseudolayer compression elastic constant of a twist-bend nematic liquid crystal.* Phys. Rev. Materials. 4, 115601 (2020).

[27] D. A. Paterson, J. P. Abberley, W. TA. Harrison, J. MD Storey and C. T. Imrie. *Cyanobiphenyl-based liquid crystal dimers and the twist-bend nematic phase.* Liq. Cryst. 44, 127 (2017).

[28] R. Ganapathy and A. K.Sood. *Tuning Rheochaos by Temperature in Wormlike Micelles.* Langmuir. 22, 11016 (2006).

[29] O. Diat, D. Roux, F. Nallet. *Effect of shear on a lyotropic lamellar phase.* J. Phys. II France. 3, 1427 (1993).

[30] D. Roux, F. Nallet, and O. Diat. *Rheology of Lyotropic Lamellar Phases.* Europhys Lett. 24, 53 (1993).

[31] P. Panizza, P. Archambault and D. Roux. *Effects of Shear on the Smectic A Phase of Thermotropic Liquid Crystals.* J. Phys. II France. 5, 303 (1995).

[32] R. Bandyopadhyay, A. K. Sood. *Effect of Screening of Intermicellar Interactions on the Linear and Nonlinear Rheology of a Viscoelastic Gel.* Langmuir. 19, 3121 (2003).

[33] J. Berret, D. C. Roux and G. Porte. *Isotropic-to-nematic transition in wormlike micelles under shear.* J. Phys. II France. 4, 1261 (1994).

[34] J. F. Berret. *Transient Rheology of Wormlike Micelles.* Langmuir. 13, 2227 (1997).

[35] A. K. Sood and R. Ganapathy. *Order and chaos in soft condensed matter.* Pramana. 67, 33 (2006).

[36] S. M. Fielding and P. D. Olmsted. *Flow phase diagrams for concentration-coupled shear banding.* Eur. Phys. J. E. 11, 65 (2003).

[37] G. Porte, J-F. Berret and J. L. Harden. *Inhomogeneous Flows of Complex Fluids: Mechanical Instability Versus Non-Equilibrium Phase Transition.* J. Phys. II France. 7, 459 (1997).

[38] R. Bandyopadhyay, G. Basappa and A. K. Sood. *Observation of Chaotic Dynamics in Dilute Sheared Aqueous Solutions of CTAT.* Phys. Rev. Lett. 84, 2022 (2000).

[39] S. M. Fielding and P. D. Olmsted. *Spatiotemporal Oscillations and Rheochaos in a Simple Model of Shear Banding.* Phys. Rev. Lett. 92, 084502 (2004).

[40] R. Ganapathy and A. K. Sood. *Intermittency Route to Rheochaos in Wormlike Micelles with Flow-Concentration Coupling.* Phys. Rev. Lett. 96, 108301 (2006).

[41] B. Chakrabarti, M. Das, C. Dasgupta, S. Ramaswamy and A. K. Sood. *Spatiotemporal Rheochaos in Nematic Hydrodynamics.* Phys. Rev. Lett. 92, 055501 (2004).

[42] R. Mandal, B. Chakrabarti, D. Chakraborty, and C. Dasgupta. *Complex dynamics of a sheared nematic fluid.* J. Phys.: Condens. Matter. 32, 134002 (2020).

[43] M. Das, B. Chakrabarti, C. Dasgupta, S. Ramaswamy, and A. K. Sood. *Routes to spatiotemporal chaos in the rheology of nematogenic fluids.* Phys. Rev. E. 71, 021707 (2005).

[44] D. Chakraborty, C. Dasgupta, and A. K. Sood. *Banded spatiotemporal chaos in sheared nematogenic fluids.* Phys. Rev. E **82**, 065301R (2010).

[45] G. Rienäcker, M. Kröger and S. Hess. *Chaotic orientational behavior of a nematic liquid crystal subjected to a steady shear flow.* Phys. Rev. E. 66, 040702R (2002).

[46] I. E. Kates *Non-Newtonian Rheology in Twist-bend Nematic Liquid Crystals.* JETP Lett. (2022). DOI: 10.1134/S0021364022601397

5

Giant electroviscous effects in a ferroelectric nematic liquid crystal

5.1 Introduction

In previous chapters, we studied the rheological properties of twist-bend nematic phase. In this chapter, we discuss electrorheological properties of ferroelectric nematic phase (N_F) which was discovered recently in highly polar and wedge-shaped molecules [3–9]. It has created a lot of interest in science and engineering communities because of its technological applications and intriguing phenomena important for fundamental science [10–16]. The ferroelectric nematic has high potential to replace the existing non-polar nematics in displays because of its striking electro-optical properties and fast response time [9, 17, 18]. Although several new physical and electrooptical properties of N_F phase have been reported [19–26] their flow viscosities and the effect of external electric field on the flows are yet unexplored. Since the constituent molecules are highly polar the electroviscous effects in ferroelectric NLCs are expected to be more robust than in ordinary nematic liquid crystals due to the interaction of polarisation with the electric field.

The electroviscous effect deals with the change in viscosity especially in polar liquids in the presence of the electric field. The electric field-dependent viscosity of such liquids can be expressed as [27, 28]

$$\eta(E) = \eta_0(1 + f|E|^2) \tag{5.1}$$

where η_0 is the viscosity in the absence of the field and f is the viscoelectric coefficient. For many organic liquids including water, $f \sim 10^{-13} - 10^{-16}$ m^2V^{-2} [27, 29]. When the

fluid is a nematic liquid crystal (NLC) the viscosity depends on the orientation of the director with respect to the flow direction. There are three flow viscosity coefficients (η_1, η_2 and η_3) of nematics which are known as Miesowicz viscosities [30, 31]. In case of η_1, the director is perpendicular to the flow direction i.e., $\hat{n} \perp \overrightarrow{v}$ and parallel to the velocity gradient i.e., $\hat{n} || \overrightarrow{\nabla} v$. For η_2, the director is parallel to the flow direction i.e., $\hat{n} || \overrightarrow{v}$. In the case of η_3 the director is perpendicular to both the velocity and velocity gradient directions, i.e., $\hat{n} \perp \overrightarrow{v}$ and $\hat{n} \perp \overrightarrow{\nabla} v$ (see Fig.1.23). These viscosity coefficients depend on the molecular structure as well as on the intermolecular interactions and usually increase with decreasing temperature. For calamitic LCs (rod-like molecules), $(\eta_1 > \eta_3 > \eta_2)$ [35, 36].

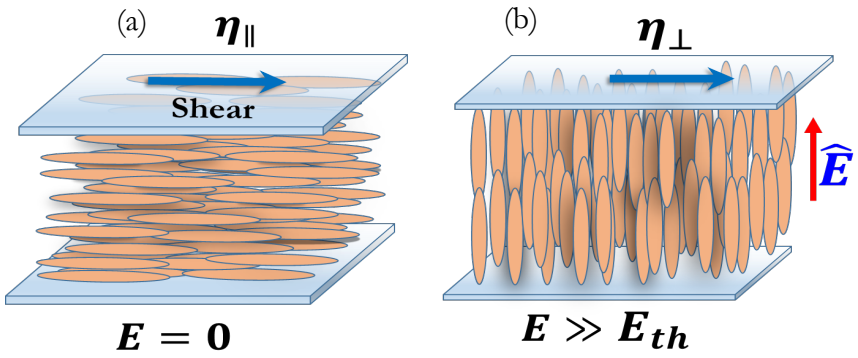

Figure 5.1: Orientation of the LC director $\hat{\mathbf{n}}$ without and with electric field, E. (a) In the absence of an electric field, $\hat{n}$ is parallel to the flow direction (blue arrow) and the apparent viscosity $\eta \simeq \eta_{||}$. (b) Above the Freedericksz threshold field $E >> E_{th}$, $\hat{n}$ is perpendicular to the flow direction and the apparent viscosity $\eta \simeq \eta_{\perp}$.

There are a few studies on the effect of electric field on the flow viscosities of ordinary NLCs [35–41]. In the absence of an electric field, the director $\hat{n}$ of the presheared nematic is parallel to the shear-flow direction and we can write the apparent viscosity $\eta \simeq \eta_2 \simeq \eta_{||}$ (Fig.5.1(a)). Preshear is necessary to get a uniform alignment of the liquid crystal director. For a NLC with positive dielectric anisotropy, above the Freedericksz threshold electric field (E_{th}), $\hat{n}$ reorients toward the field direction and the apparent viscosity increases and saturates at higher fields and $\eta \simeq \eta_1 \simeq \eta_{\perp}$ (Fig.5.1(b)). Here, $\eta_{||}$ and $\eta_{\perp}$ are the viscosities of the NLCs with the director $\hat{n}$ parallel and perpendicular to the flow direction, respectively. The rising part of the viscosity from zero field to the onset of saturation can be expressed by Eq.(5.1) and the coefficient f can be regarded

as the viscoelectric coefficient of the nematic liquid crystal. It signifies the growth rate of the electroviscosity due to the applied electric field.

5.2 Experimental

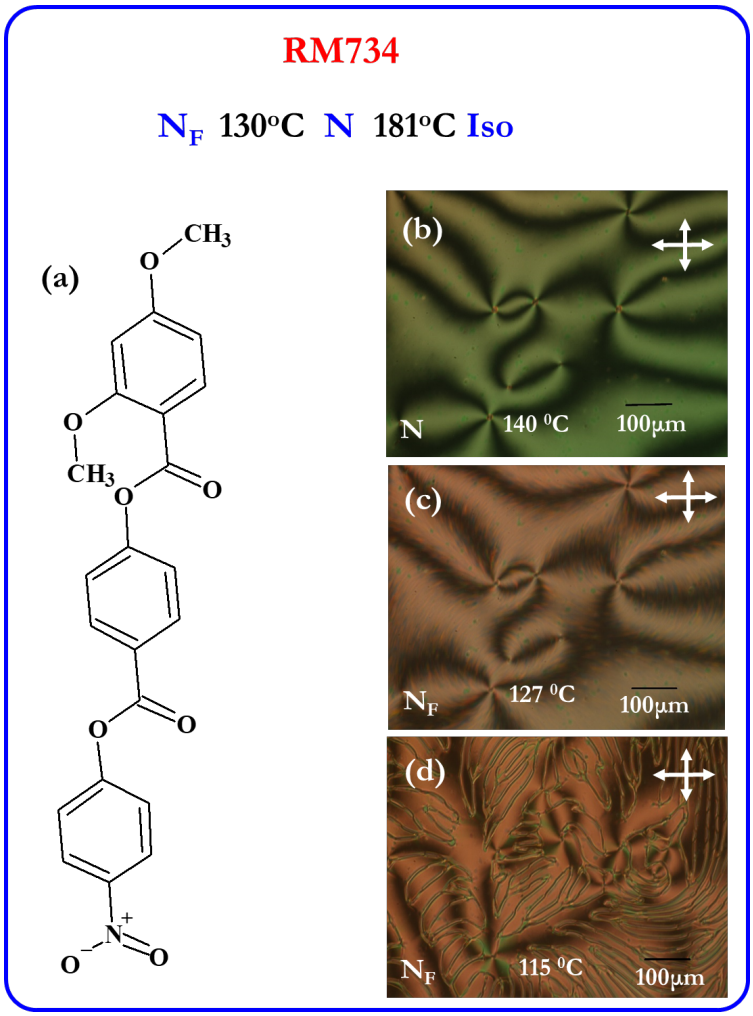

Figure 5.2: (a) Chemical structure of Ferroelectric nematic compound RM734. (b) Nematic phase texture under POM at 140°C. (c) Appearance of brush like at N-N_F phase transition (127°C) and (d) a large number of additional lines appearance in N_F phase (115°C).

We work with a ferroelectric nematic liquid crystal RM-734 synthesized by our collaborator in Poland. Its chemical formula, phase transition temperature, and POM textures are shown in Fig.5.2. The DSC data of RM734 is shown in Fig.5.3. The peaks at 184°C and 127°C represents the nematic-isotropic and nematic to ferroelec-

tric nematic phase transition temperatures. Their corresponding enthalpies are 0.95 J/g and 0.34 J/g, respectively. Since the material is monotropic, all the rheological measurmeants are done in cooling mode. We set up a computer-controlled electrorheological experiment based on a rheometer. The measuring device consists of two parallel plates with a fixed gap connected to an LCR meter and interfaced with a computer. The setup is capable of measuring the viscosity and the dielectric constant simultaneously. Electrorheological measurements were made using a rheometer (Anton Paar Physica MCR-501) fitted with an electrorheological device consisting of two 50 mm diameter parallel plates, separated by a distance of $80\mu m$. The plates are coated with polyimide AL-1254 (JSR Corporation) and cured at 180°C for 1 hour for planar anchoring. An LCR meter (Agilent E4980A) was used for applying ac voltage and simultaneously measuring the static dielectric constant at a frequency f =600 Hz. A schematic diagram of the experimental setup is shown in Chapter 2 (Fig.2.4). The sample temperature was controlled with a Peltier controller, and the parallel plates were covered with an insulated hood to maintain the uniformity of the sample temperature.

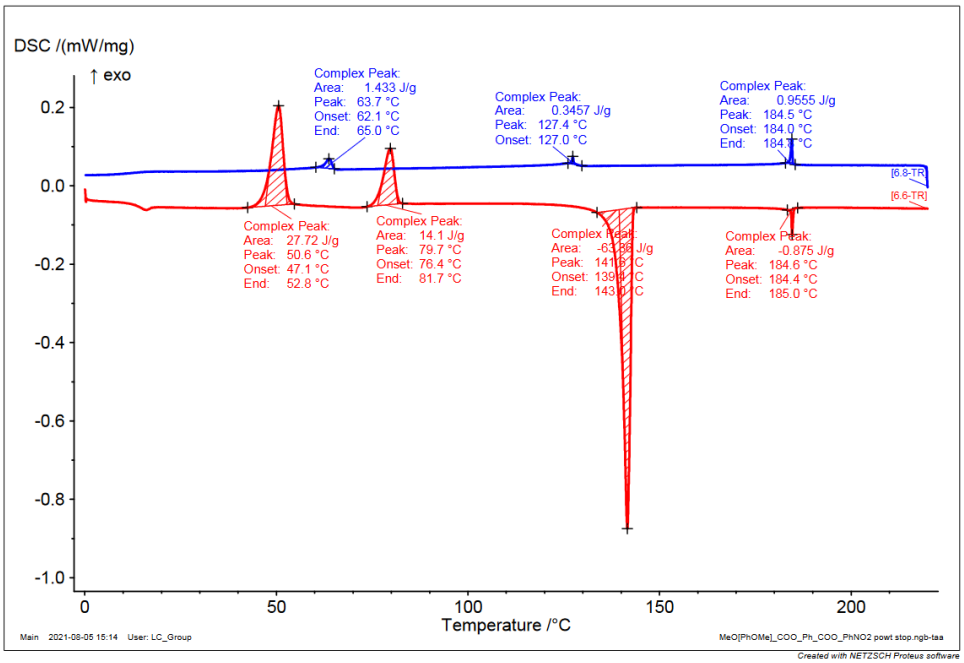

Figure 5.3: Differential scanning calorimetry (DSC) data of RM734.

All the measurements were done in cooling the sample from the isotropic phase. We worked in the voltage range of 0.1 to 20V at frequency f=600 Hz. The sample was presheared at a fixed shear rate $\dot{\gamma}$ =120 s^{-1} for 5 minutes before doing any measurements. The experiments were controlled by a computer using a Rheoplus software and a Labview program developed by us. In our experiment, the measured dielectric constant ϵ in the N_F phase is an effective one for the polydomain texture. We have chosen an optimum frequency (600 Hz) to avoid electrical short-circuit due to the relatively higher ionic electrical conductivity of the bulk sample in the low-frequency range. We collected the sample from the rheometer after the measurements and checked the phase transition temperatures under polarising optical microscope. We did not observe any noticeable change in the N-I and N-N_F phase transition temperatures after the first scan.

5.3 Results and discussion

First, we measured electric field-dependent viscosity, known as apparent viscosity at different temperatures by changing the amplitude of the electric field at a fixed frequency. The viscosity of the presheared sample is independent of the shear rate (see Appendix Fig.4.10), hence we fixed the shear rate $\dot{\gamma}$ = 120s^{-1} for all measurements. Figure.5.4(a) shows the variation of apparent viscosity η at different temperatures in the nematic (N) phase of RM-734. The viscosity below a particular field (Freedericksz threshold, $E_{th} \simeq 2.5 \times 10^4$ V/m) is constant (= η_0) and it rises rapidly with the field and saturates above $E \simeq 1.0 \times 10^5$ V/m. Figure 5.4(b) shows the variation of apparent viscosity at different temperatures in the N_F phase.

In this phase, the viscosity shows similar trends but the relative enhancement of viscosity with respect to the zero field viscosity is smaller compared to that of the N phase. In order to bring out the differences we introduce normalised viscosity, defined as $\eta_N = \frac{\eta(E)}{\eta_0}$, where η_0 is the zero-field viscosity (Fig.5.4(c)). It is noted that the change of saturated viscosity with temperature is non-monotonic. For example, the saturated viscosity increases as the temperature is raised from 160°C and reach a maximum value at the N-N_F transition and then decreases drastically as the temperature is reduced.

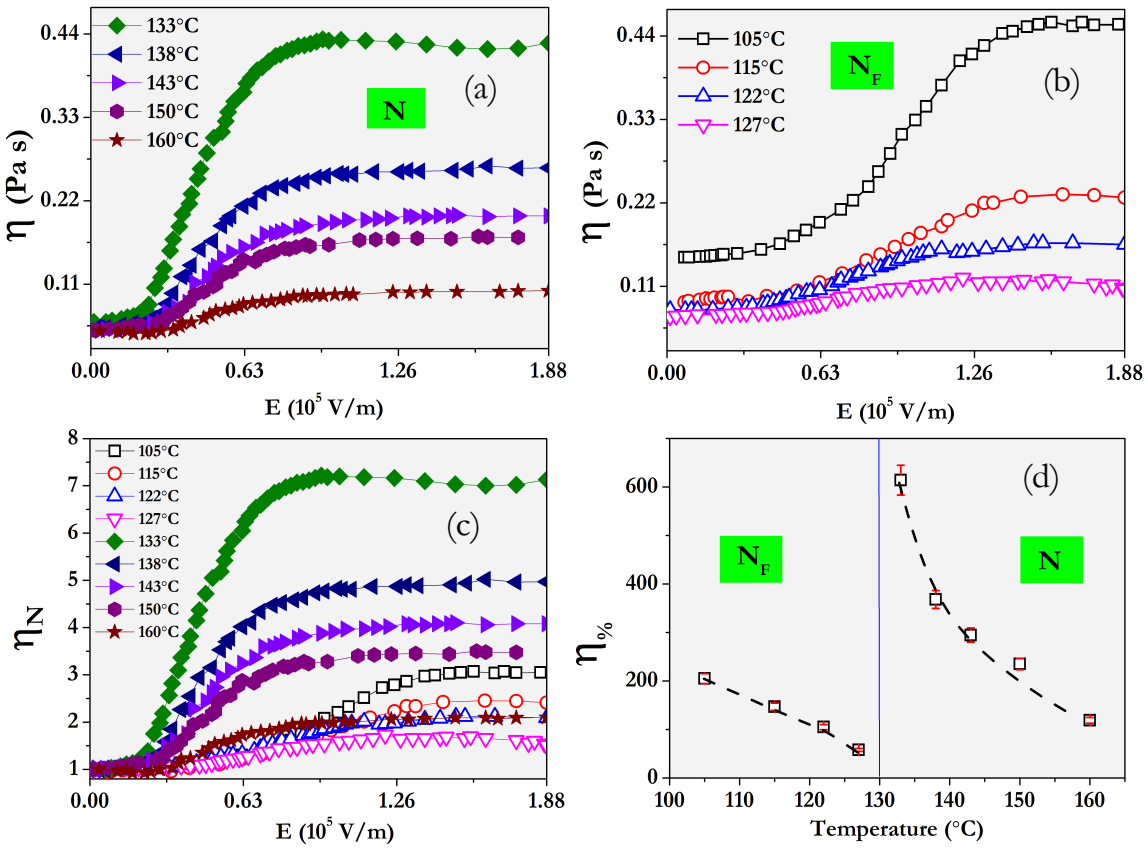

Figure 5.4: Change of apparent viscosity η with a.c electric field at different temperatures in the (a) N and (b) N_F phases. Measurements are made at a shear rate $\dot{\gamma} = 120$ s^{-1}. (c) Normalized viscosity, $\eta_N = \frac{\eta(E)}{\eta_0}$ in both phases, where η_0 is the constant viscosity in the absence of the electric field. (d) The percentage increment of viscosity, $\eta_{\%} = \frac{\eta(E=E_s)-\eta_0}{\eta_0} \times 100$, at different temperatures, where E_s is the field above which the viscosity is saturated. We chose 1.7×10^5 V/m. The vertical line indicates N-N_F phase transition temperature. Dashed line is a guide to the eye.

Figure 5.4(d) shows the relative enhancement of viscosity in terms of percentage, which can be written as $\eta_{\%} = \frac{\eta(E=E_s)-\eta_0}{\eta_0} \times 100$, where $\eta(E = E_s)$ is the saturated viscosity. The percentage increment of viscosity $\eta_{\%}$ increases rapidly as the N-N_F phase transition is approached and the pronounced effect is observed very close to the N-N_F transition temperature where the enhancement is about 600%. Below the phase transition, it drastically decreases to 50% (T= 127°C) and again gradually increases to 200% which will be discussed later.

We obtained the viscoelectric coefficient f at different temperatures using Eq.(5.1) which can be expressed as $\Delta\eta/\eta_0 = fE^2$, where $\Delta\eta = \eta(E) - \eta_0$. Figure 5.5(a) and (b) shows the variation of $\Delta\eta/\eta_0$ with E^2 in N and N_F phases, respectively. The coefficient f is obtained from the slope of the linear part of the curve in the low field region (below the onset of saturation) and shown in Fig.5.5 (c). In the N phase (e.g., T=160°C) $f = 0.4 \times 10^{-9}$ m^2V^{-2} and it increases rapidly as the N-N_F transition is approached. The maximum value is obtained ($f = 2.1 \times 10^{-9}$ m^2V^{-2}) near N-N_F transition temperature. This is about six orders of magnitude larger than that of ordinary liquids like water [27, 29] and the largest ever measured for a fluid.

In order to compare the same with ordinary NLCs with polar molecules we measured the viscoelectric coefficient of 5CB (pentyl cyanobiphenyl) liquid crystal. Figure 5.5(d)) shows a change in apparent viscosity with the electric field at a few temperatures and corresponding f of 5CB LC. The coefficient f ($\simeq 1.25 \times 10^{-11}$ m^2V^{-2}) is independent of temperature and almost two orders of magnitude smaller than RM-734 liquid crystal. The molecules of 5CB have an axial dipole moment of 4.8 D [42] which is almost two and a half times smaller than compound RM-734 (11.3 D) [6]. Thus, due to the large dipole moments and the resulting dipole-dipole correlation, the viscoelectric coefficient of RM-734 is expected to be much higher than nematics with nonpolar or weakly polar molecules. However, two orders of magnitude larger f of RM-734 and its rapid growth indicate the emergence of polar domains that grows rapidly as the N-N_F transition is approached.

In what follows, we have measured the temperature-dependent apparent viscosity η of a presheared sample. We fixed the shear rate $\dot{\gamma} = 120$ s^{-1}, and measured the viscos-

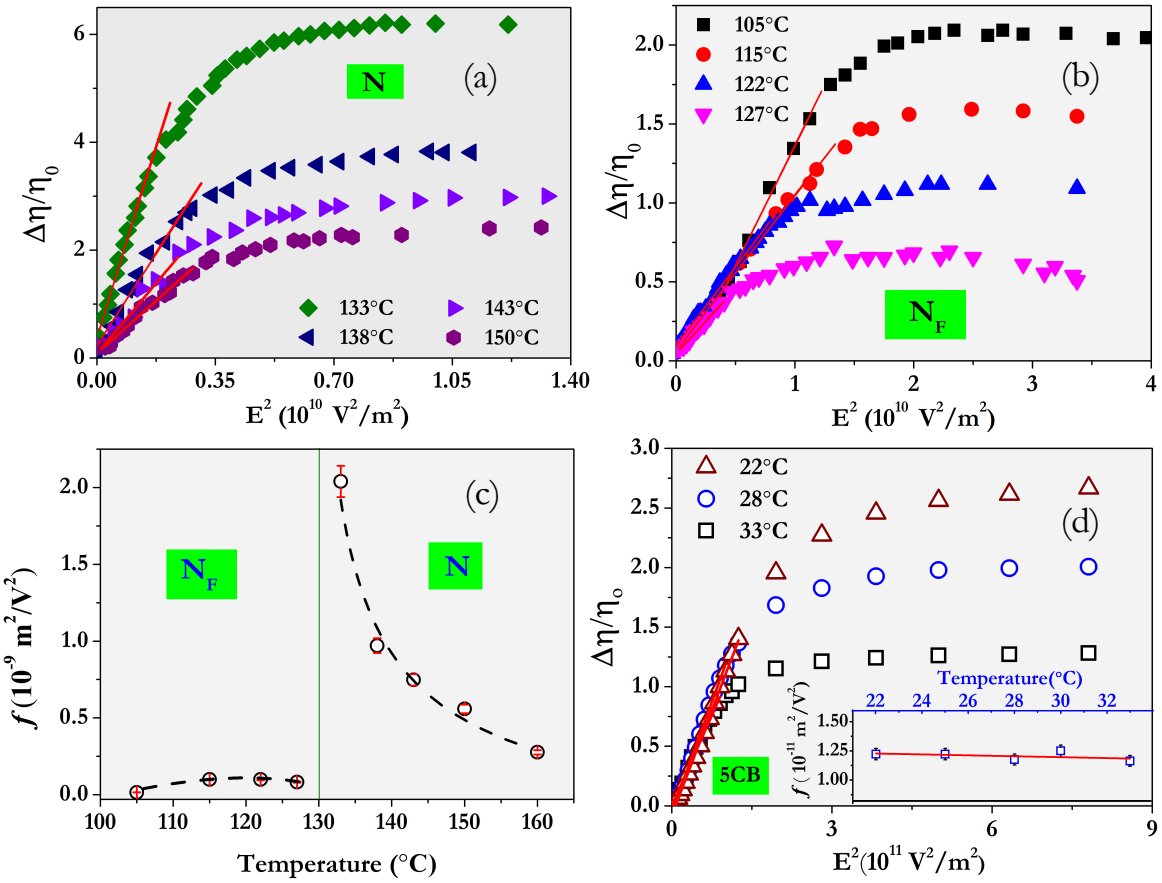

Figure 5.5: Variation of $\Delta\eta/\eta_0$ with E^2 at different temperatures in (a) N and (b) N_F phases. The red lines are best fit to the linear part of the curves. (c) Variation of viscoelastic coefficient f with temperature. The dashed line is a guide to the eye. The vertical line indicates N-N_F phase transition temperature. (d) Variation of $\Delta\eta/\eta_0$ with E^2 of 5CB at a few temperatures. Shear rate $\dot{\gamma} = 120$ s^{-1}. The inset shows the variation of f with a temperature of 5CB LC.

ity $\eta_{||}$ ($E << E_{th}$) and $\eta_{\perp}$ ($E >> E_{th}$) as a function of temperature (Fig.5.6(a)). The viscosity increases with decreasing temperature as expected. No significant change in $\eta_{||}$ is observed at the N-N_F transition temperature ($T = 130°C$). On the other hand $\eta_{\perp}$ increases much more rapidly with decreasing temperature and tends to diverge at the N-N_F transition temperature. It reaches a maximum of 900 mPas at the transition and the corresponding viscosity anisotropy $\delta\eta = \eta_{\perp} - \eta_{||} = 750$ mPas, which is nearly an order of magnitude larger than the ordinary NLCs [32, 35, 38] and largest viscosity anisotropy ever measured for any NLC. It is noted that $\eta_{\perp}$ changes slope below temperature T=150°C, at which the collective behaviour of the molecules starts to develop [7]. Below the N-N_F transition the viscosity drops down significantly to about 140 mPas from 900 mPas, showing $\eta_{\perp}$ of the N_F phase is reduced compared to the N phase although the orientational order parameter of the N_F phase is larger [4]. Such a drastic decrease of $\eta_{\perp}$ is consistent with the first-order nature of the N-N_F phase transition and it suggests that microscopically the structure of these two phases are different. Although the dielectric properties of this LC are quite complex [43–45] we could simultaneously measure an effective dielectric constant ϵ (Fig.5.6(b)) at a frequency of 600 Hz (see Appendix). Since the dielectric anisotropy is positive, $\epsilon \simeq \epsilon_{\perp}$ when $E << E_{th}$ and $\epsilon \simeq \epsilon_{||}$ when $E >> E_{th}$ (Fig.5.6(c)). It is noted that $\epsilon_{||}$ shows a nearly diverging trend followed by a small kink at the N-N_F phase transition temperature (Fig.5.6(a)). The diverging trend in $\epsilon_{||}$ is a signature of cooperative molecular motion possibly leading to polar domains which are basically dynamic clusters of parallel dipoles.

At high temperatures, due to thermal fluctuations, the size of the polar domains should be small, but as the temperature is decreased towards N-N_F transition, the domain size will grow. Higher electric field can enhance parallel correlation of dipoles and facilitate domain growth. Under these conditions, the viscosity is expected to increase, as seen in Fig.5.6(a) because larger stress will be needed to deform the polar domains. Thus, one does not expect a strong deviation between the measurements of viscosity done in the following two scenarios; (1) with the high field on at high temperature and then cooled to the lower temperature (referred to here as field cooled) and (2) first cooled at the required temperature and then apply the desired electric field (zero field-cooled) and measure the viscosity. In both these scenarios, the domain will

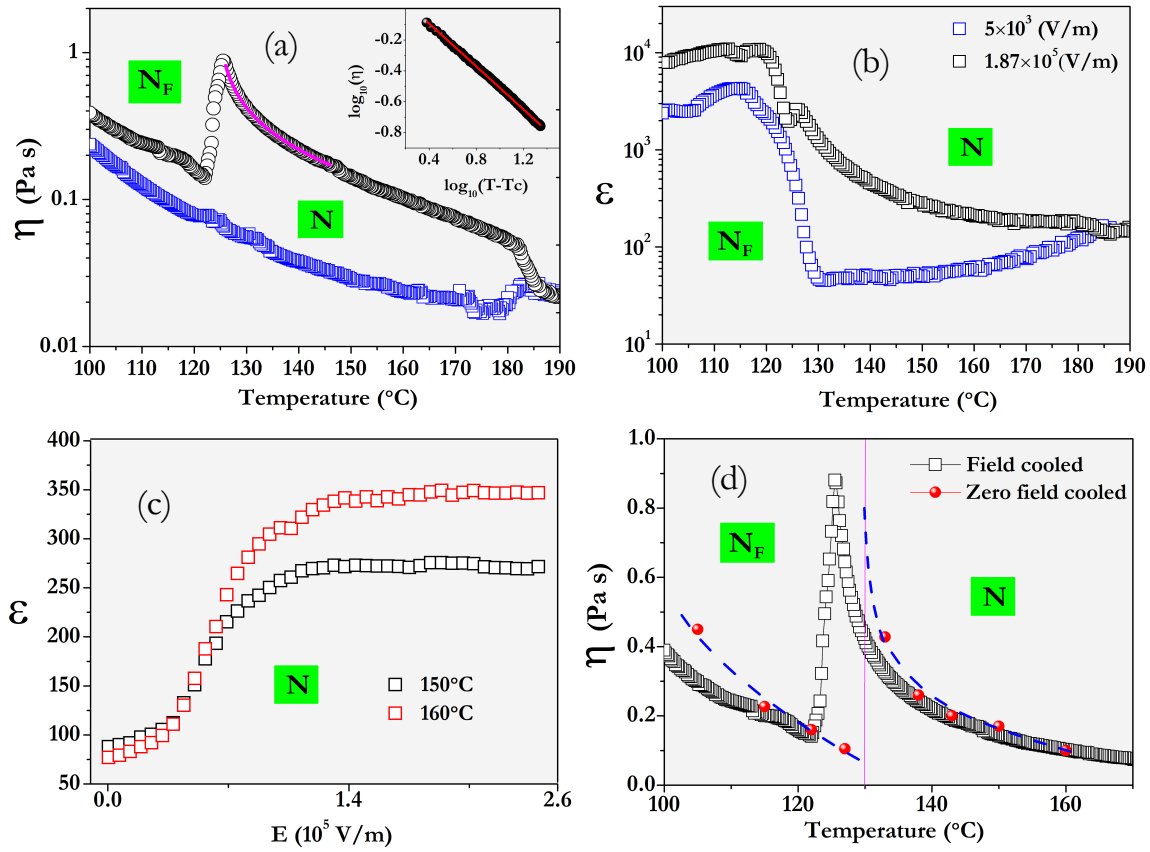

Figure 5.6: (a) Temperature dependence of apparent viscosity η measured at $\dot{\gamma} = 120$ s^{-1}, at two electric fields. Blue squares correspond to data measured at $E = 5 \times 10^3$ V/m ($<< E_{th}$) and black circles correspond to data measured at $E = 1.87 \times 10^5$ V/m ($>> E_{th}$). Inset shows a power-law fit to $\eta \sim (T - T_C)^{-0.7\pm0.05}$ to the diverging viscosity where $T_c = 124.13$°C. Magenta curve indicates the temperature range selected for fitting. (b) Temperature dependence of effective dielectric constant ϵ measured at $f = 600$ Hz. (c) Variation of ϵ with field at two temperatures in the N phase. (d) Growth of viscosity η as a function of temperature in two different conditions. One with the electric field E on. This is referred here as "field-cooled" (black squares, $E = 1.87 \times 10^5$ V/m) and the other set (red dots) are obtained from Fig.5.4(a,b) where the system is cooled to the lower temperature first and then the field is applied to measure the viscosity. Dashed blue line is a guide to the eye for zero-field cooled data. The vertical line indicates N-N_F transition temperature under zero-field.

grow when the electric field is applied in the N phase, so one expects the measurements to be very similar qualitatively and quantitatively. As shown in Fig.5.6(d), the data indeed suggest the same (see data for $T > T_c$).The results will be very different below the transition temperature simply because at zero field cooling conditions; the system will go through a sharp structural change due to N to N_F phase transition. On the other hand, in the field-cooled conditions, the polar domains in the N phase will not allow the system to immediately go to the N_F phase and the sharp phase transition will be rounded as evident from Fig.5.6(d). Although the scenario proposed seems to be quite likely the reason for the observation, we do not have direct proof of the growth of the polar domain with the applied field. Future computational studies on these systems can unearth the microscopic mechanisms for these experimental observations.

If we compare the temperature-dependent viscosity (Fig.5.6(a)) and dielectric constant (Fig.5.6(b)) measured at the high field and those at the low field then N-N_F transition temperature at high field is found to be decreased by about 4°C. This decrease is not due to the sample degradation under field (see Appendix). It can be rationalized as caused by the structural changes during the N-N_F phase transition following two possible scenarios. Firstly, the high field can suppress the pre-transitional splay fluctuations [6, 46] and favours domain growth with the polarity along the field and hence one would expect the N-N_F transition temperature to decrease if it is considered that the ferronematic phase can have domains with splay structure. Note that the largest applied field in this experiment is not sufficient to align all the molecules along the field direction in the N_F, otherwise, there will not be any phase transition. Secondly, the polar regions will grow in size but they can not span the entire sample as the nematic phase does not support the orientation of all the molecules in the same direction due to large dipole moments. With decreasing temperature, these polar regions grow in size and thus we see a power law change in the measured viscosity in the nematic phase in field-cooled condition. As the temperature is lowered below the equilibrium N-N_F transition, thermodynamically the N_F phase with opposite polarity domains will be favoured as observed in the experiment [9], but the already formed polar regions will oppose the formation of this N_F phase until at a lower temperature where the enthalpy will win over and the system will go to the N_F phase. The near equality of the viscosity data measured in the field-cooled and zero-field-cooled scenar-

ios below the N-N_F phase transition indeed supports this argument. Note that in the latter scenario, the splay structure is not essential to explain the observed decrease in the transition temperature.

Further, it is expected that there will be a growth of a length scale related to the formation of polar domains in the nematic phase and if we assume that the length scale shows a divergence at the transition temperature, T_c as $\xi \sim |T - T_c|^{-\nu}$ with ν being the correlation length exponent, then one can expect to see a similar power-law divergence of the viscosity within the dynamical scaling approximation [47] as $\eta \sim \xi^z \equiv |T - T_c|^{-\nu z}$ where z is the dynamical scaling exponent. The power-law fit to the viscosity date is shown in the inset of Fig.5.6 (a), and the fit is very nice to confirm such a possible power-law divergence of viscosity with an exponent $\nu z \sim 0.7$. Currently, we do not have an independent estimate of the exponent ν, so we can not compute the exponent z. On the other hand, the correlation length exponent in critical phenomena within mean field approximation is $\nu = \frac{1}{2}$, so if we assume the same exponent here, then the dynamical exponent $z \sim 1.4$. This suggests that the domains are probably more elongated (one-dimensional) in nature than spherical. Some of these conjectures can be tested via computer simulation studies which are in progress.

We would like to make a comment here. A one-dimensionally modulated splay structure of the ferroelectric nematic phase of compound RM-734 was proposed by Mertelj *et al.* [6] whereas a two-dimensionally modulated splay structure is proposed by the theory [15]. However, Chen *et al.* reported the occurrence of spontaneously polar domains of the opposite sign of polarisation separated by distinct domain boundaries [9]. Our explanation on the temperature-dependent electroviscosity does not rely on any particular structure of the ferroelectric nematic phase.

5.4 Conclusion

To summarise, ferroelectric nematic LCs exhibit giant electroviscous effects and the viscoelectric coefficient obtained is the largest ever measured for a fluid. The apparent viscosity under field-cooled condition shows a power-law divergence as the N-N_F transition is approached followed by a drastic decrease below the transition. Large

viscoelectric coefficient and pretransitional divergence of the electroviscosity indicate a strong polar correlation resulting in elongated domains that grow rapidly with decreasing temperature. We envisage that the pretransitional growth of polar domains and their dynamic response should be manifested in many other physical properties and effects. The synthetic route reported here is significant for large-scale production which is crucial for the application. These results obtained are important for most of the physical, electrooptical as well as the electrohydromechanical [10–13] effects in ferroelectric nematic liquid crystals. They may also be useful for applications in micro and nanofluidic electromechanical devices (MEMS/NEMS) based on ferroelectric nematic liquid crystals.

5.5 Appendix

5.5.0.1 Viscosity measurements

We heated the sample to the isotropic phase and cooled it down to the nematic phase. Then it was presheared with a fixed shear rate for 5 minutes as mentioned previously. At a fixed temperature we measured the viscosity of the presheared sample as a function of shear rate at two different electric fields. A representative result at T=140° C is shown in Fig.5.7. The viscosity of the presheared sample is independent of shear rate ($\dot{\gamma}$=10 s^{-1}). Then we step by step decreased the temperature and measured viscosity as a function of applied electric field. For all electric field-dependent viscosity measurements, we have chosen shear rate $\dot{\gamma}$=120 s^{-1}. For the temperature-dependent simultaneous viscosity and effective dielectric constant measurements, we kept the shear rate fixed as described in the text and measured the viscosity as well as the dielectric constant in steps of 0.1° C. The LCR meter was connected to the rheometer through the external trigger of the rheometer for measuring the dielectric constant.

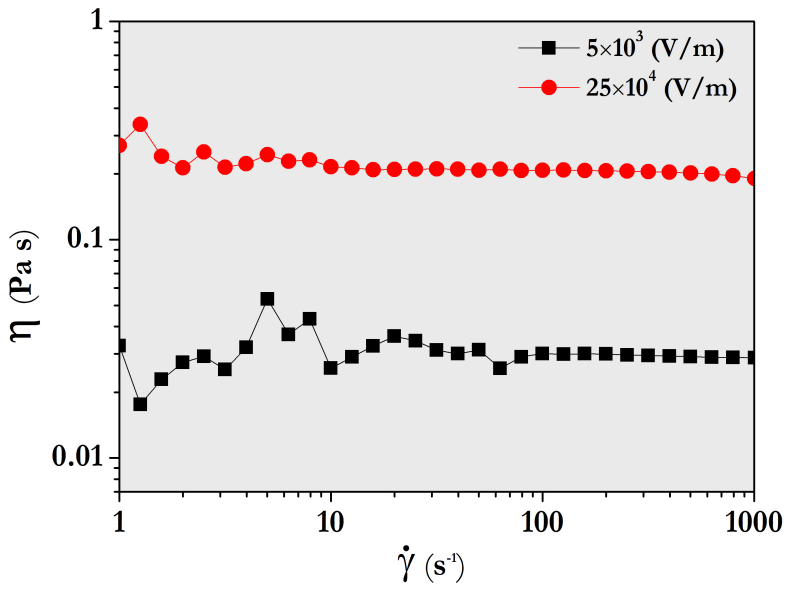

Figure 5.7: Flow curves of RM-734 at fixed temperature 140° C and two electric fields after preshearing at a shear rate $\dot{\gamma}$=120 s^{-1} for 5 minutes in nematic phase (N).

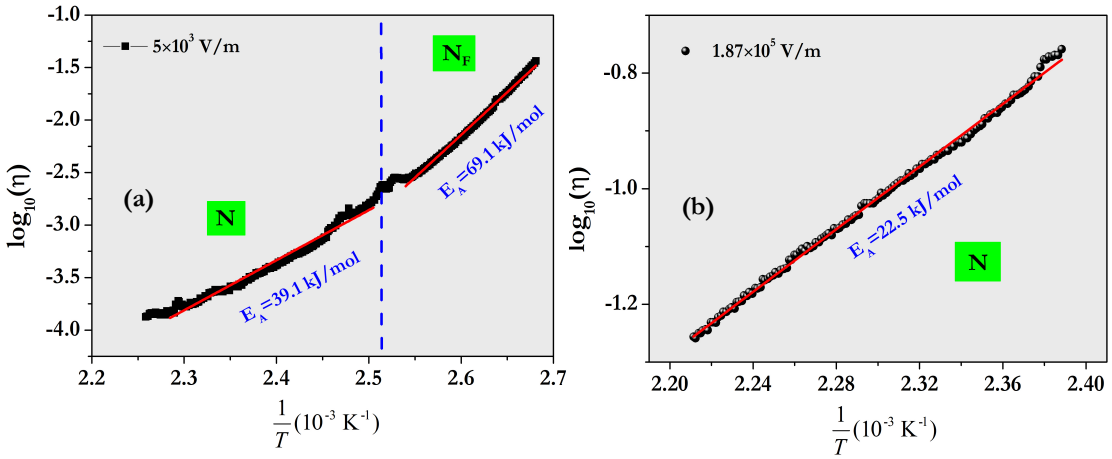

Figure 5.8: (a) Arrhenius plot of the viscosity measured at $E = 5 \times 10^3$V/m below and above the N-N_F phase transition temperature (indicated by dotted line). Red lines are the best fit to the data with activation energies as shown under the lines. (b) Arrhenius plot of the viscosity measured at $E = 1.87 \times 10^5$V/m in the temperature range of 180 to 150°C in the N phase.

References

[1] P. G. de Gennes, *The Physics of Liquid Crystals.* (Oxford University Press: Oxford, England 1974).

[2] M. Born. *About anisotropic liquids. Attempt at a theory of liquid crystals and the Kerr electric effect in liquids.* Sitzungsber Preuss Akad Wiss. 30, 614 (1916).

[3] R. J. Mandle, S. J. Cowling and J. W. Goodby. *Rational design of rod-like liquid crystals exhibiting two nematic phases.* Chem. A Eur. J. 23, 14554 (2017).

[4] R. J. Mandle and A. Mertelj. *Orientational order in the splay nematic ground state.* Phys. Chem. Chem. Phys. 21, 18769 (2019).

[5] H. Nishikawa, K. Shiroshita, H. Higuchi, Y. Okumura, Y. Haseba, I. Yamamoto, S. Koki, and H. Kikuchi. *A fluid liquid crystal material with highly polar order.* Adv. Mater. 29, 1702354 (2017).

[6] A. Mertelj, L. Cmok, N. Sebastián, J. Mandle, R. R. Parker, A. C. Whitwood, J. W. Goodby, and M. Čopič. *Splay Nematic Phase.* Phys. Rev. X. 8, 041025 (2018).

[7] A. Manabe, M. Bremer, and M. Kraska. *Ferroelectric nematic phase at and below room temperature.* Liq. Cryst. 48, 1079 (2021).

[8] N. Sebastián, L. Cmok, R. J. Mandle, M. R. de la Fuente, I. D. Olenik, M. Čopič, and A. Mertelj. *Ferroelectric-Ferroelastic phase transition in a nematic liquid crystal.* Phys. Rev. Lett. 124, 037801 (2020).

[9] X. Chen, E. Korblova, D. Dong, *et al. First-principles experimental demonstration of ferroelectricity in a thermotropic nematic liquid crystal: Polar domains and striking electro-optics.* Proc. Natl. Acad. Sci. USA. 117, 14021 (2020).

[10] M. T. Máthé, Á. Buka, A. Jákli, and P. Salamon. *Ferroelectric nematic liquid crystal thermomotor.* Phys. Rev. E. 105, L052701 (2020).

[11] R. Barboza, S. Marni, F. Ciciulla, F. A. Mir, G. Nava, F. Caimi, A. Zaltron, N. A. Clark, T. Bellini, and L. Lucchetti. *Explosive electrostatic instability of ferroelectric liquid droplets on ferroelectric solid surfaces.* Proc. Natl. Acad. Sci. USA. 119, e2207858119 (2022).

[12] M. T. Máthé, B. Farkas, L. Péter, Á. Buka, A. Jákli, and P. Salamon. *Electric field-induced interfacial instability in a ferroelectric nematic liquid crystal.* arXiv:2210.14329v1 (2022).

[13] L. Cmok, V. Coda, N. Sebastián, A. Mertelj, M. Zgonik, S. Aya, M. Huang, G. Montemezzani, and I. Drevenšek-Olenik. *Running streams of a ferroelectric nematic liquid crystal on a lithium niobate surface.* Liq. Cryst. 1, (2023).

[14] J. Yang, Y. Zou, W. Tang, J. Li, M. Huang, and S. Aya. *Spontaneous electric-polarization topology in confined ferroelectric nematics.* Nat. Commun. 13, 7806 (2022).

[15] M. P. Rosseto, and J. V. Selinger. *Theory of the splay nematic phase: single versus double splay.* Phys. Rev. E. 101, 052707 (2020).

[16] R. Saha, P. Nepal, C. Feng, M. S. Hossain, M. Fukuto, R. Li, J. T. Gleeson, S. Sprunt, R. J. Twieg, and A. Jákli. *Multiple ferroelectric nematic phases of a highly polar liquid crystal compound.* Liq. Cryst. 49, 1784 (2022).

[17] X. Chen, E. Korblova, M. A. Glaser, J. E. Maclennan, D. M. Walba, and N. A. Clark. *Polar in-plane surface orientation of a ferroelectric nematic liquid crystal: Polar monodomains and twisted state electro-optics.* Proc. Natl. Acad. Sci. USA. 118, e2104092118 (2021).

[18] N. Sebastián, R. J. Mandle, A. Petelin, A. Eremin, and A. Mertelj. *Electrooptics of mm-scale polar domains in the ferroelectric nematic phase.* Liq. Cryst. 48, 2055 (2021).

[19] O. D. Lavrentovich. *Ferroelectric nematic liquid crystal, a century in waiting.* Proc. Natl. Acad. Sci. USA. 117, 14629 (2020).

[20] S. Brown, E. Cruickshank, J. M. D. Storey, C. T. Imrie, D. Pociecha, M. Majewska, A. Makal, and E. Gorecka. *Multiple polar and non-polar nematic phases.* Chem. Phys. Chem. 22, 2506 (2021).

[21] H. Nishikawa, and F. Araoka. *A new class of chiral nematic phase with helical polar order.* Adv. Mater. 2101305 (2021).

[22] P. Rudquist. *Revealing the polar nature of a ferroelectric nematic by means of circular alignment.* Sci. Rep. 11, 24411 (2021).

[23] C. L. Folcia, J.Ortega, R. Vidal, T. Sierra, and J. Etxebarria. *The ferroelectric nematic phase: an optimum liquid crystal candidate for nonlinear optics.* Liq. Cryst. 49, 899 (2022).

[24] F. Caimi, G. Nava, R. Barboza, N. A. Clark, E. Korblova, D. M. Walba, T. Bellini, and L. Lucchetti. *Surface alignment of ferroelectric nematic liquid crystals.*, Soft Matter. 17, 8130 (2021).

[25] J. Li, H. Nishikawa, J. Kougo, J. Zhou, S. Dai, W. Tang, X. Zhao, Y. Hisai, M. Huang, and S. Aya. *Development of ferroelectric nematic fluids with giant-ε dielectricity and nonlinear optical properties.* Sci. Adv. 7, eabf5047 (2021).

[26] X. Zhao, J. Zhou, J. Li, J. Kougo, Z. Wan, M. Huang, and S. Aya. *Spontaneous helielectric nematic liquid crystals: Electric analog to helimagnets.* Proc. Natl. Acd. Sci. USA. 118, e2111101118 (2021).

[27] R. J. Hunter, and J. V. Leyendekkers. *Viscoelectric coefficient for water.* J. Chem. Soc. Faraday Trans. 1. 74, 450 (1978).

[28] E. N. D. C. Andrade, and C. Dodd. *The effect of an electric field on the viscosity of liquids.* Proc. Roy. Soc. A. 187, 296 (1946).

[29] D. Jin, Y. Hwang, L. Chai, N. Kampf, and J. Klein. *Direct measurement of the viscoelectric effect in water.* Proc. Natl. Acd. Sci. USA. 119, e2113690119 (2022).

[30] M. Miesowicz. *The three coefficients of viscosity of anisotropic liquids.* Nature. 158, 27 (1946).

[31] R. G. Larson. *The structure and rheology of complex fluids.* (Oxford University Press, New York 1999).

[32] A. G. Chmielewski. *Viscosity coefficients of some nematic liquid crystals.* Mol. Cryst. Liq. Cryst. 132, 339 (1986).

[33] H. Imura, and K. Okano. *Temperature dependence of the viscosity coefficients of liquid crystals.* Jpn. J. Appl. Phys. 11, 1440 (1972).

[34] S. Chandrasekhar. *Liquid Crystals* (Cambridge University Press, Cambridge, England 1992).

[35] J. Ananthaiah, R. Sahoo, M. V. Rasna, and S. Dhara. *Rheology of nematic liquid crystals with highly polar molecules.*, Phy. Rev. E. 89, 022510 (2014).

[36] M. T. Cidade, C. R. Leal, and P. Patricio. *An electro-rheological study of the nematic liquid crystal* 4-*n*-*heptyl*-4′-*cyanobiphenyl.* Liq. Cryst. 37, 1305 (2010).

[37] P. Patricio, C. R. Leal, L. F. V. Pinto, A. Boto, and M. T. Cidade. *Electro-rheology study of a series of liquid crystal cyanobiphenyls: experimental and theoretical treatment.* Liq. Cryst. 39, 25 (2012).

[38] K. Negita. *Electrorheological effect in the nematic phase of* 4-*n*-*pentyl*- 4′-*Cyanobiphenyl.* J. Chem. Phys. 105, 7837 (1996).

[39] J. J. Wysocki, J. Adams, and W. Haas. *Electroviscosity of a Cholesteric Liquid Crystal Mixture.* J. Appl. Phys. 40, 3865 (1969).

[40] J. Ananthaiah, M. Rajeswari, V. S. S. Sastry, R. Dabrowski, and S. Dhara. *Effect of electric field on the rheological and dielectric properties of a liquid crystal exhibiting nematic-to-smectic-A phase transition.* Eur. Phys. J. E. 34, 74 (2011).

[41] J. Ananthaiah, R. Sahoo, M. V. Rasna, and S. Dhara. *Rheology of nematic liquid crystals with highly polar molecules.* Phys. Rev. E. 89, 022510 (2014).

[42] D. A. Dunmur, M. R. Manterfield, W. H. Miller, and J. K. Dunleavy. *The dielectric and optical properties of the homologous series of cyano-alkyl-biphenyl liquid crystals.* Mol. Cryst. Liq. Cryst. 46, 127 (1978).

[43] N. Vaupotič, D. Pociecha, P. Rybak, J. Matraszek, M. Čepič, J. M. Wolska, and E. Gorecka. *Dielectric response of a ferroelectric nematic liquid crystalline phase in thin cells.* arXiv preprint arXiv:2210.04697 (2022).

[44] N. A. Clark, X. Chen, J. E. Maclennan, and M. A. Glaser. *Dielectric spectroscopy of ferroelectric nematic liquid crystals: Measuring the capacitance of insulating interfacial layers.* arXiv preprint arXiv:2208.09784(2022).

[45] R. J. Mandle, N. Sebastián, J. Martinez-Perdiguero, and A. Mertelj. *On the molecular origins of the ferroelectric splay nematic phase.* Nat. Commun. 12, 4962 (2021).

[46] A. Barthakur, J. Karcz, P. Kula, and S. Dhara. *Critical splay fluctuations and colossal flexoelectric effect above the nonpolar to polar nematic phase transition.* Phys. Rev. Materials. 7, 035603 (2023)

[47] P. C. Hohenberg, and B. I. Halperin. *Theory of dynamic critical phenomena.* Rev. Mod. Phys. 49, 435 (1977).

[48] D. Ziobro, J. Dziaduszek, M. Filipowicz, R. Dabrowski, J. Czub, and S. Urban. *Synthesis of fluoro substituted three ring esters and their dielectric properties.* Mol. Cryst. Liq. Cryst. 502, 258 (2009).

[49] D. G. Hall, in Boronic Acids, Wiley-VCH Verlag GmbH and Co. KGaA, Weinheim, Germany, 2011, pp. 1-133.

6

Effect of Sm-A short-range order on the activation energies of translational and rotational viscosities of nematic liquid crystals with highly polar molecules

6.1 Introduction

In the last three chapters, we studied the rheological properties of nematic liquid crystals with lower symmentry, namely the twist-bend and ferroelectric nematic phases. In this chapter, we investigate the flow viscosities of nematic liquid crystals made of small molecules with a large transverse dipole moment. As discussed in previous chapters the translational or the shear viscosity depends on the orientation of the director ($\hat{n}$) with respect to the shear and the velocity gradient directions. Miesowicz first defined and measured three flow viscosities, namely; η_1 ($\hat{n}||\nabla v$), η_2 ($\hat{n} \perp \nabla v$) and η_3 ($\hat{n} \perp v$ and , ∇v). Figure 6.1 schematically represents mutual orientation of the director, velocity (v) and the velocity gradient (∇v) directions leading to three viscosities. These viscosities can be expressed in terms of six Leslie coefficients α_i [4–6]. There are several studies on the effect of molecular structures on the viscosities and their temperature dependences [7–15]. The flow alignment angle of the director with respect to the shear direction is given by $\theta = tan^{-1}(\sqrt{\alpha_3/\alpha_2})$ [16]. In the vicinity of

the nematic-isotropic (N-I) transition, usually, both are negative, and the director is aligned along the flow direction with a small angle ($\theta \lesssim 5^{\circ}$).

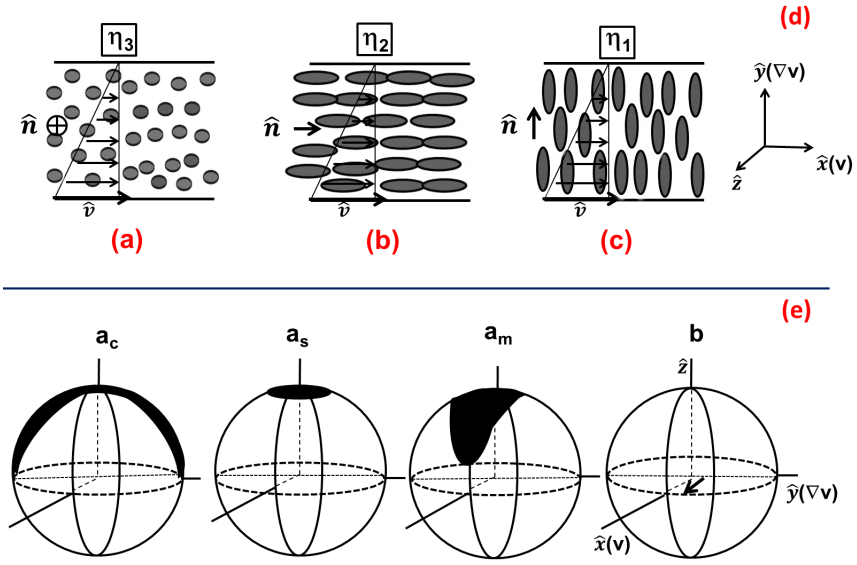

Figure 6.1: (a-c) Schematic diagrams are showing three different director orientations with respect to (d) shear and corresponding Miesowicz viscosities. (e) Schematic representation of different types of distribution of $\hat{n}$ on the unit sphere [16]. The first sphere from the right hand side represents the 'b' orientation corresponding to the viscosity η_2. The shaded regions on the subsequent unit spheres show the excursion of the director under shear in different distribution types.

Safinya *et al.* reported an interesting effect of critical slowing down of the SmA order fluctuations on the dynamics of nematic director of liquid crystals exhibiting N-SmA phase transition [16,17]. They showed that near the N-SmA transition, renormalised α_3 represented as α_3^R becomes positive due to the divergence of correlation length $\xi_{||}$ and the nematic director evolves through a precessional motion along the neutral direction, z (perpendicular to both the velocity and velocity gradient directions) which can be described by an equation of ellipse [16]: $n_x^2(t)/n_{x0}^2 + n_y^2(t)/n_{y0}^2 = 1$, where $n_x(t) = n_{x0}cos(\omega_0 t)$ and $n_y(t) = n_{y0}sin(\omega_0 t)$. The precessional frequency ω_0 depends on the shear rate $\dot{\gamma}$, the Leslie coefficients α_2 and α_3^R. Consequently, several steady states with different director distributions were observed as the N-SmA transition was approached depending on the relative amplitudes of the projected director components along x and y directions, respectively. A schematic representation of different distribution types

of $\hat{n}$ is shown with shaded areas covering the unit spheres in Fig.6.1(e). They are denoted as a_m, a_s, $a(b)$ and a_c [16]. In a_m type, $n_{x0} > n_{y0}$; in a_s type $n_{x0} \simeq n_{y0}$, in $a(b)$ type, $n_{x0} < n_{y0}$ (not shown in Fig.6.1(e)) and in a_c type $n_{x0} << n_{y0}$. The director dynamics presented in Fig.6.1 has been captured by three-dimensional nonuniform orientation simulations using Leslie-Ericksen equations by Han *et al.* [18, 19]. The effect of such distribution of director has also been investigated experimentally by non-equilibrium rheodielectric studies [20–22]. Rotational viscosity (γ_1) is another important property which is directly related to the electrooptical response time of the liquid crystal displays. There are several experimental studies on the measurement of rotational viscosity of NLCs [14, 15]. There are also some reports in which attempts were made to correlate flow and rotational viscosities [10, 11].

In this chapter, we report experimental studies on the temperature dependence of shear and rotational viscosities of a homologous series of cyanobiphenyl with longitudinal and cyanobicyclohexane liquid crystals with transverse dipole moments. We show that the activation energies in the nematic phase of both shear and rotational viscosities of compounds having N-SmA phase transition are much higher than that of compounds having no N-SmA phase transition in the homologous series. We discuss the effect of SmA short-range order on the rotational viscosity and the critical slowing down of the Sm-A order parameter fluctuations on the shear viscosity of cyanobicyclohexane and cyanobiphenyl compounds exhibiting N-SmA phase transition. Both effects are much stronger in liquid crystals with longitudinal dipole moments than in transversely polar molecules.

6.2 Experimental

We studied a few compounds from the homologous series of cyanobiphenyl (nCB) and cyanobicyclohexane (CCN-mn) liquid crystals. The cyano group (-CN) is oriented along the longitudinal and transverse directions for nCB and CCN-mn molecules, respectively. The phase transition temperatures and molecular structures of the compounds are shown in Table 6.1 and in Fig.6.2 respectively. The CCN-mn compounds have bicyclohexane core, hence exhibit very low birefringence ($\Delta n \simeq 0.03$) [23]. CCN-

35 exhibits only nematic -isotropic (N-I) phase transition. CCN-47 exhibits both N-I and N-SmA phase transitions. Compounds CCN-73 and CCN-55 exhibits both N-I and N-SmB phase transitions. The dielectric anisotropy of the compounds are large and negative ($\Delta\epsilon < 0$) due to the presence of transverse dipole moments (see Fig.6.2) [23–26]. The nCB compounds are well known. They exhibit a large positive dielectric anisotropy and larger birefringence then CCN-mn compounds.

Sample	Phase transitions (°C)	Nematic range (°C)
CCN35	Cry 38.4 N 49.3 I	10.9
CCN73	Cry 38.6 SmB 38 N 50.2 I	12.2
CCN47	Cry 25.6 SmA 28.2 N 57.3 I	29.1
CCN55	Cry 25 SmB 30 N 66.4 I	30.4

Table 6.1: Phase transition temperatures of CCN-35, CCN-73, CCN-47 and CCN-55 compounds.

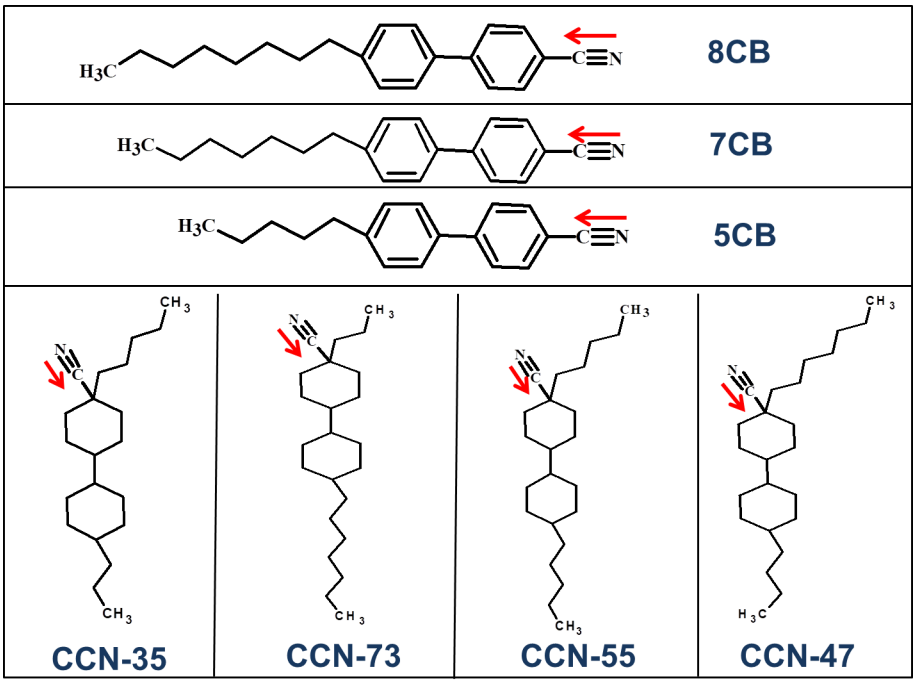

Figure 6.2: Chemical structure of cyanobiphenyl (nCB) and cyano bicyclohexane (CCN-mn) compounds. The red arrows show the directions of permanent dipole moments of -C≡N group.

In this work shear viscosity was measured using (Anton Paar MCR-501) rheometer

in cone-plate geometry with a plate diameter of 25 mm and cone angle of 1°. For measuring the dielectric constant, we used parallel plate configuration with a gap of 75 μm. The dielectric constant was measured as a function of temperature with the help of an LCR meter (Agilent E4980A) at an applied voltage of 0.5V and frequency of 4.11 kHz. The details of the rheodielectric setup are presented in chapter-2 (see Fig.2.4). The temperature of the sample was controlled with an accuracy of 0.1°C. All the measurements were made on cooling the samples from the isotropic phase.

Rotational viscosity of the CCN-mn compounds was measured in homeotropic cells by using-phase-decay time measurement technique [31]. The experimental setup consists of two Glan-Thompson polarisers, a He-Ne laser and a photomultiplier tube (Hamamatsu) (see Fig.2.8 in chapter-2). The nematic director was deformed by applying a small voltage above the Freedericksz threshold value. The director relaxes when the voltage is switched off at $t = 0$. The corresponding decay in the phase retardation is approximately expressed as $\delta(t) = \delta_0 \exp(-2t/\tau_0)$, where δ_0 is the total phase change of the cell and τ_0 is the relaxation time. The rotational viscosity is given by $\gamma_1 = \tau_0 K_{33}\pi^2/d^2$, where d is the cell gap and K_{33} is the bend elastic constant. In case δ_0 is close to $n\pi$, the retardation decays as: $\delta(t) = \delta_0 \exp(-4t/\tau_0)$. τ_0 is obtained from the slope of the linear plot of $ln[\delta_0/\delta(t)]$ with time t [13, 31].

6.3 Results and discussion

First, we performed rheodielectric measurements of nCB liquid crystals at a fixed shear rate ($\dot{\gamma} = 100\text{s}^{-1}$), and the results are shown in Fig.6.3(a). The effective shear viscosity (η_{eff}) of both 5CB and 7CB decreases discontinuously below the NI phase transition and then continues to increase as the temperature is reduced. The corresponding rheodielectric data suggests that in the nematic phase $\varepsilon_{eff} \simeq \varepsilon_{\perp}$. Hence the director gets 'b' orientation in the nematic phase as described in Fig.6.1(e) and consequently $\eta_{eff} \simeq \eta_2$. The rheodielectric data of 8CB looks very different in comparison to 5CB and 7CB, especially near the N-SmA phase transition (Fig.6.3(b)). A small discontinuity around $T_{NI} - T = 2.2$°C, indicates a change of director orientation from 'b' to an intermediate regime, labelled as '$a - b$'. A corresponding change is also

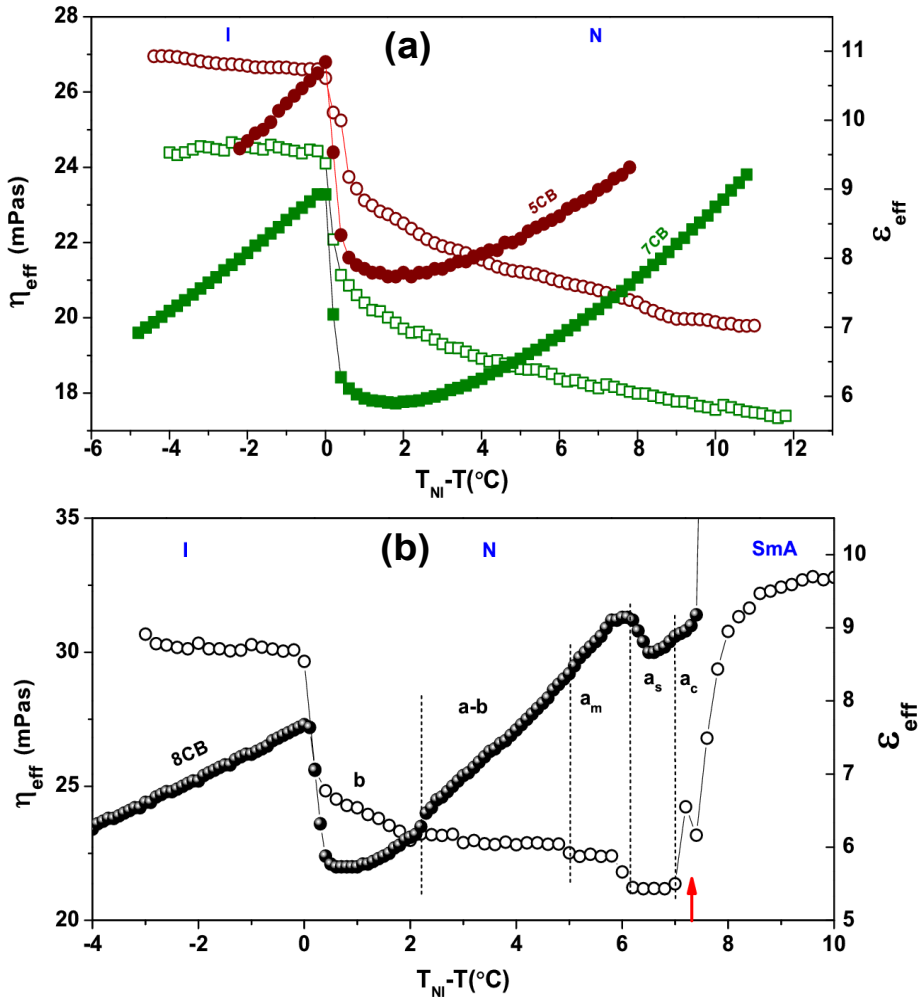

Figure 6.3: Temperature dependence of effective viscosity (η_{eff}) and the dielectric constant (ε_{eff}) as a function of temperature measured at a fixed shear rate $\dot{\gamma} = 100\text{s}^{-1}$ for (a) 5CB and 7CB and (b) 8CB. Solid and open symbols represent the viscosity and dielectric constant, respectively. The steady states with director distribution types 'a' , '$a-b$' (intermediate regime of'a' and 'b'), '$a(m)$', 'a_s' and 'a_c' are labelled in correlation to the shear induced distributions reported by Safinya *et al.* [16]. The red arrow in the bottom figure indicates N-SmA phase transition temperature.

reflected in the temperature variation of ε_{eff}. Below $T_{NI} - T = 5°C$, the average director orientation is changed along the neutral direction (z-direction). The temperature variation of dielectric constant reflects the effective orientation of the director with respect to the applied electric field under shear. While decreasing the temperature from the isotropic phase at a few temperatures, both the values and slopes of η_{eff} and ϵ_{eff} simultaneously change, indicating changes in the director distribution. These temperatures are marked by a vertically dotted line in Fig.6.3(b). Both η_{eff} and ϵ_{eff} increases discontinuously at the N-SmA phase transition ($T_{NI} - T \simeq 7.5°C$), which is marked by an upward arrow in Fig.6.3(b). This is because of the weak first order N-SmA phase transition of 8CB. The steady states with different director distributions, namely a_m, a_c and a_s are identified from the change of slope in ε_{eff} and in η_{eff} and they are consistent with the results of synchrotron x-ray studies reported by Safinya *et al.* [16]. They showed that there is an interplay of frictional and flow-induced fluctuation forces on the nematic director as the N-SmA transition is approached. Consequently several steady states as mentioned emerge due to the critical slowing down of the SmA order parameter fluctuations. This effect is clearly revealed in the rheodielectric data. Although Negita *et al.* reported rheodielectric measurements on 8CB [20] using a homemade concentric double cylinder type viscometer, our rheodielectric measurements using a cone-plate and parallel plate geometries of MCR 501 rheometer are able to capture for the first time, the fine structure of director distributions associated with different steady states. It may be mentioned that the transition temperatures of different steady states weekly depend on the applied shear-rates. To avoid this, we kept the low shear, i.e., $\dot{\gamma} = 100s^{-1}$ in our experiments.

There are several experimental studies on the anchoring transition of CCN-47 [32–34]. It was proposed that there exists a smectic short-range order in the nematic phase [35–37]. Inspired by this, we studied the rheodielectric properties of CCN-47 and also a few compounds of the homologous series. Figure 6.4 shows the temperature dependence of effective shear viscosity (η_{eff}) and effective dielectric constant (ε_{eff}). For all the compounds η_{eff}, decreases below the N-I phase transition and then increases as the temperature is decreased. It is observed that η_{eff}^{CCN-47} increases more rapidly in the nematic phase compared to the other homologues as the N-SmA transition is approached. For example, there is a small slope change at a temperature of

$T_{NI} - T = 7°C$, and we identify this as a change of orientation from steady state 'b' to an intermediate regime '$a - b$' type (Fig.6.4(a)). It has been shown that there is a SmA short-range order in the nematic phase of CCN-47 liquid crystal [35]. Hence it is legitimate to expect the occurrence of steady states due to the critical slowing down of the SmA order parameter fluctuations similar to that of 8CB. However, we do not see any distinct variation of effective viscosity (like we see in the case of 8CB) as the N-SmA transition is approached except another small slope change in the η_{eff} at $T_{NI} - T = 24°C$ (for CCN-47). This change is an indication of the change of director orientation and attributed to the onset of the appearance of other steady states 'a_m', 'a_s', '$a(b)$' and 'a_c'. Unlike 8CB, the steady states are not distinguishable in CCN-47.

The effective dielectric constant ε_{eff} measured at the same shear rate are shown in Fig.6.4(b). ε_{eff} increases discontinuously for all the compounds below the N-I phase transition temperature. This confirms that the steady state form is 'b' type since the dielectric anisotropy of all the compounds is negative. For CCN-47 above $T_{NI} - T = 24°C$, ε_{eff} tends to increase as indicated by a small vertical arrow in Fig.6.4(b). This is consistent with the viscosity data and is associated to the onset of subsequent steady states. However they can not be distinguished as clearly as we see in case of 8CB (see Fig.6.3). This means that the SmA order parameter fluctuations in CCN-47 are not as strong as that of 8CB. In other words, $\xi_{||}$ is much larger in 8CB than that of CCN-47, i.e., $\xi_{||}^{8CB} > \xi_{||}^{CCN-47}$. A schematic diagram of the fluctuating SmA cluster with correlation length $\xi_{||}$ is shown in Fig.6.5 when Deborah number $D = \dot{\gamma}\tau \simeq 1$, where $\dot{\gamma}$ is the shear rate and τ is the longest characteristic structural relaxation time [17]. These clusters are anisotropic and tend to get distorted due to the shear flow, which is energetically costly.

The effect of SmA short-range order fluctuations can be seen on the temperature dependence of $\xi_{||}$ hence we looked at the critical exponents in both these compounds, which can be obtained easily from the temperature dependence of bend elastic constant K_{33}. According to the mean field theory, the renormalised bend elastic constant varies as: $K_{33}^R \propto \xi_{||}(T)$. The correlation length diverges as: $\xi_{||}(T) \sim t^{-\nu}$, where $t = (T - T_{N-SmA})/T_{N-SmA}$, is the reduced temperature and ν is the critical exponent [17, 38]. From the temperature dependent measurement of bend elastic constant near N-SmA

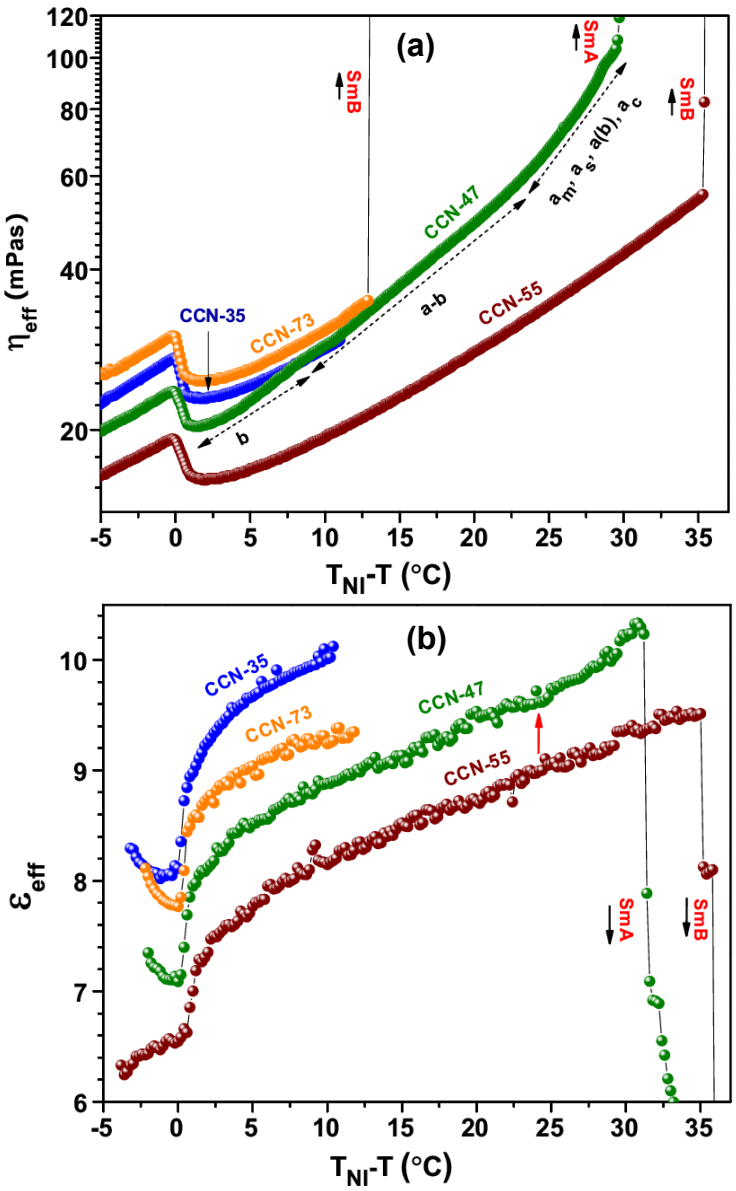

Figure 6.4: (a) Temperature variation of effective shear viscosity (η_{eff}) and (b) effective dielectric constant (ε_{eff}) of CCN-mn compounds measured under a fixed shear rate $\dot{\gamma} = 100\text{s}^{-1}$. The vertical solid lines and upward arrows in the viscosity data in the top figure indicate the viscosity increases discontinuously at the N-SmA or N-SmB phase transitions. The temperature range of steady states, b' and '$a-b$', '$a(m)$', 'a_s', '$a(b)$' and 'a_c' are labelled under the viscosity data of CCN-47 with dotted arrows. The vertical solid lines and downward arrows in the viscosity data in the bottom figure indicate the dielectric constant decreases discontinuously at the N-SmA or N-SmB phase transitions. The upward arrow below the dielectric data of CCN-47 indicates a small slope change due to the occurrence of steady states.

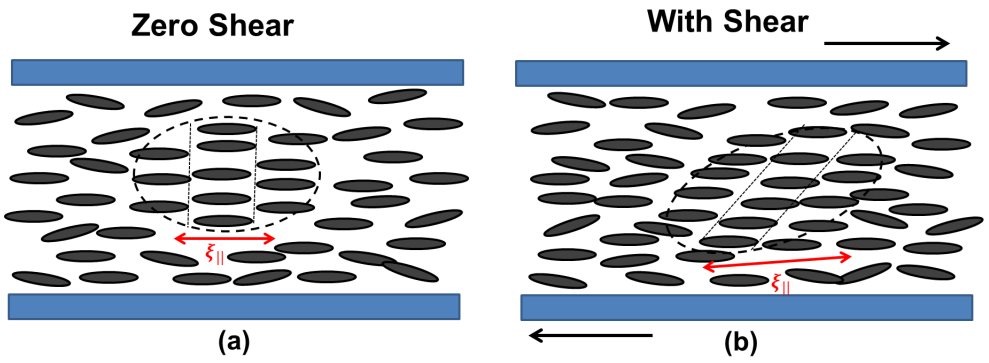

Figure 6.5: Schematics of a cluster with the nematic director along $\hat{y}$ (a) at rest and (b) under shear flow. The dotted ellipse indicates SmA type order with correlation length $\xi_{||}$ along the director.

phase transition, it was reported that in the case of 8CB, $\nu \simeq 1$ [39], whereas, for CCN-47, $\nu \simeq 0.3$, which is much smaller than that of 8CB [40], that indicates CCN-47 is a weaker SmA short-range order. Another significant difference in the physical properties of these two classes of homologous compounds is that the splay elastic constant of CCN-47 is much larger than the bend elastic constant, i.e., $K_{11} > K_{33}$ whereas in the case of 8CB $K_{11} < K_{33}$ [23, 40].

The temperature dependent linear part of the shear viscosity in the N phase of all the compounds are fitted to the Arrhenius equation: $\eta_{eff}(T) = \eta_0 exp(E_S/kT)$ to get the activation energy (E_s) of the translational viscosity. The fittings for CCN-mn compounds are shown in Fig.6.6. For nCB the fittings are performed on the data shown in Fig.6.3 but not shown here. The activation energies of shear viscosity in the nematic phase (E_S) of all the compounds are summarised in Table 6.2. This table brings out some interesting aspects of the activation energies of the nematic liquid crystals made of highly polar molecules with transverse and longitudinal dipole orientations. It is noticed that E_S of CCN-47 which exhibits N-SmA transition is larger than that of other homologues. For example, E_S of CCN-47 is about 66% larger than that of CCN-35 (shortest homologue). Similarly, in nCB compounds, 8CB has much larger E_S than 5CB or 7CB. For example, E_S of 8CB is 185% larger than that of the shortest homologue 5CB. Hence, the activation energy of translational viscosity

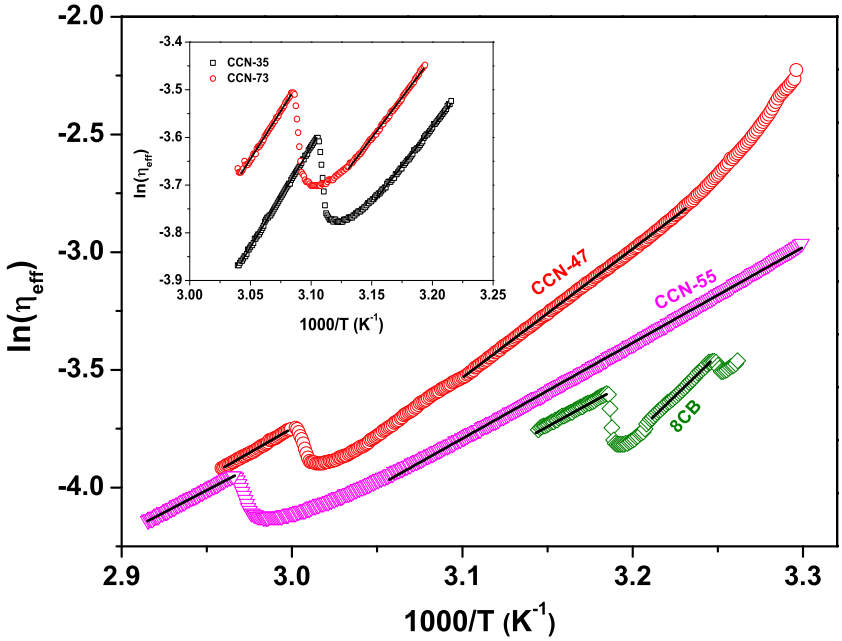

Figure 6.6: Estimation of activation energy of shear viscosity from the Arrhenius equation, $\eta_{eff}(T) = \eta_0 exp(E_S/kT)$. Variation of $ln(\eta_{eff})$ with $1000/T$. Solid lines represent the least square fits to the data. Due to shorter temperature range, CCN-35 and CCN-73 are shown separately in the inset.

in the nematic phase is significantly larger in polar compounds with longitudinal and transverse dipole moments which have SmA phase at lower temperatures.

We measured the rotational viscosity (γ_1) of the CCN-mn compounds as a function of temperature and presented in Fig.6.7(a). We notice that except very close to NI, γ_1 of CCN-47 is relatively larger than other homologues and also it increases much rapidly as the N-SmA phase transition is approached. This is expected as the smectic correlation length increases with decreasing temperature i.e., $\gamma_1 \propto \sqrt{\xi}$, where $\xi \sim (T/(T - T_{NA}))^{0.33}$ [43]. The rotational viscosity of the nematic is related to the Leslie coefficients and is given by $\gamma_1 = \alpha_3 - \alpha_2$ [10, 44]. The renormalised α_3^R due to the SmA short-range order fluctuations is proportional to η_2 ($\alpha_3^R \propto \eta_2$). Thus SmA short-range order is reflected in both the translational and rotational viscosities. The temperature dependence of rotational viscosity can be expressed as $\gamma_1(T) \sim Sexp(E_R/kT)$ [15], where S is the orientational order parameter and is pro-

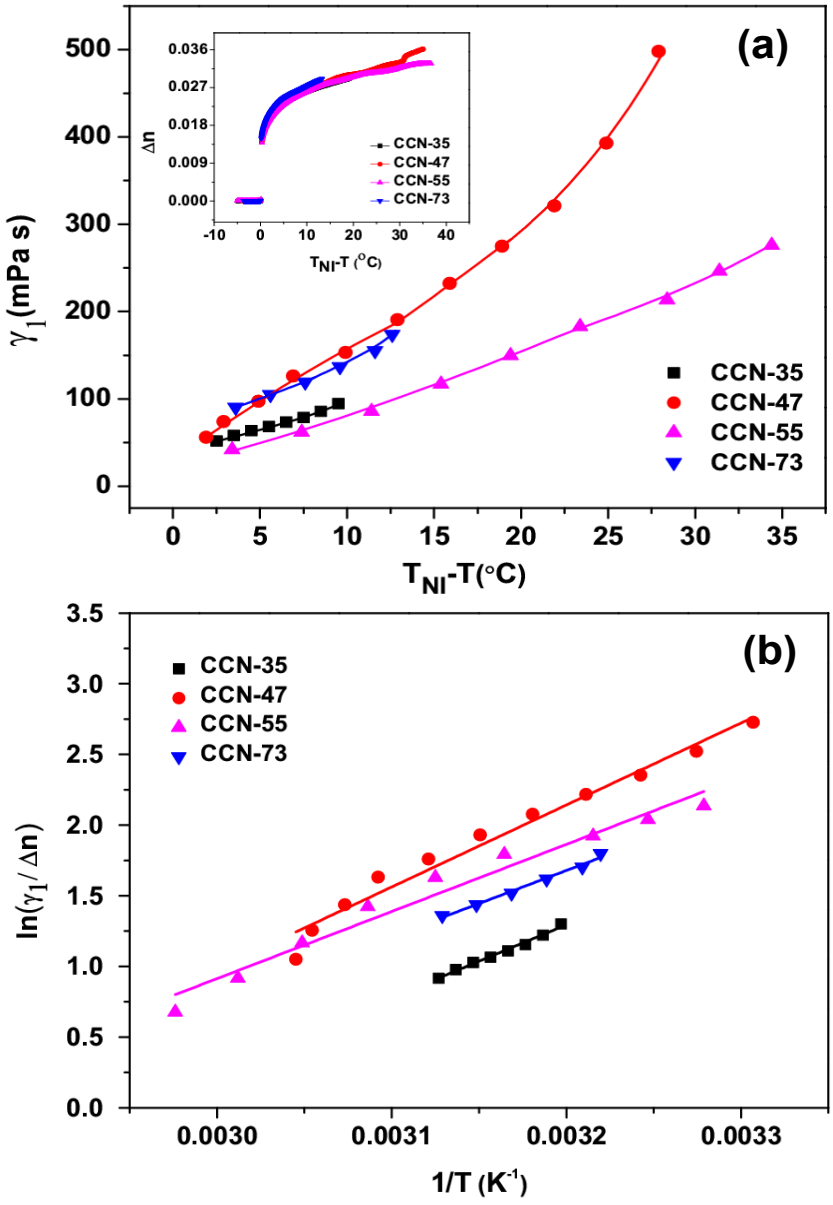

Figure 6.7: (a) Temperature dependence of rotational viscosity (γ_1) of CCN-mn compounds. (Inset) Birefringence (Δn) of the samples adapted from ref. [23]. (b) Inverse temperature dependence of $\ln(\gamma_1/\Delta n)$. Solid line represents the least square fits to the data.

Samples	E_S (N-phase, kJ/mole)	E_R (N-phase, kJ/mole)
CCN-35	27	42
CCN-73	26	39
CCN-47	45	48
CCN-55	31	39
5CB	20	27 [13]
7CB	30	37 [42]
8CB	57	71 [41]

Table 6.2: $E_S \rightarrow$Activation energy of shear viscosity in the nematic phase. $E_R \rightarrow$ Activation energy of the rotational viscosity in the nematic phase. E_R of 5CB, 7CB and 8CB were obtained from ref. [13], ref. [42] and ref. [41] respectively.

portional to the birefringence Δn, and E_R is the activation energy of the rotational viscosity. The temperature variation of Δn of the compounds is shown in the inset of Fig.6.7(a). In the nematic phase, it is almost the same for all the compounds. Figure.6.7(b) shows a linear variation of $ln(\gamma_1/\Delta n)$ with $1/T$. The activation energies obtained from the fitting are also presented in Table 6.2. The activation energies of rotational viscosities of nCB compounds were obtained from several references [13,41,42]. Activation energy of rotational viscosity (E_R) of CCN-47 which has SmA phase is also comparatively larger than that of other homologues. For example, E_R of CCN-47 is about 15% larger than the shortest homologue CCN-35. Similarly, in nCB homologous series, 8CB has much larger E_R than 5CB or 7CB. For example, E_R of 8CB is 163% larger compared to the shortest homologue 5CB. Hence the activation energy of rotational viscosity in the nematic phase is significantly larger in longitudinally polar compounds with SmA phase. This suggests that CCN-47 and 8CB have SmA short-range order, but it is comparatively weaker in CCN-47.

We present a simple physical model of molecular association that accounts for the smaller SmA short-range order and activation energies in the nematic phase of CCN-47 than that of 8CB. It is known that liquid crystal molecules with strong permanent

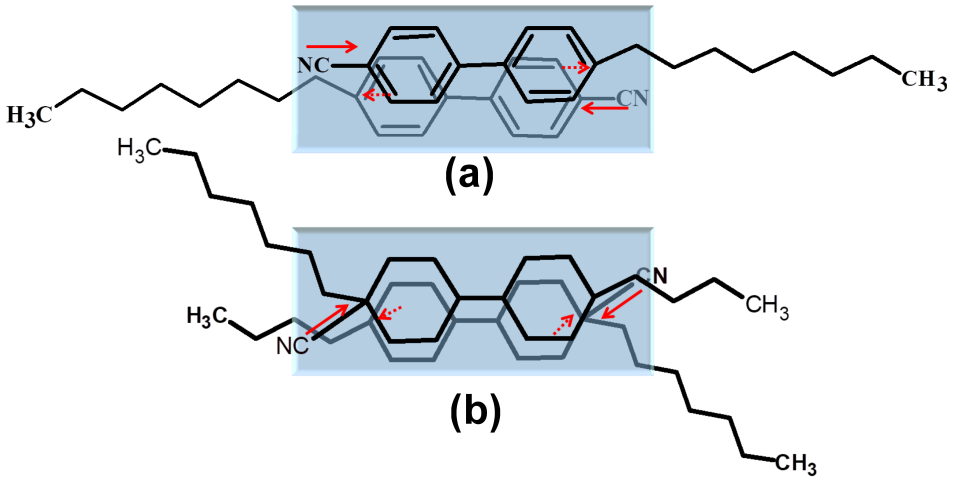

Figure 6.8: Schematic diagram showing the antiparallel configuration of (a) two 8CB molecules and (b) two CCN-47 molecules. The arrow with a solid red line represents the permanent dipole moment and the one with a dotted line, the induced one. The polar cyano group (-C≡N) is parallel and perpendicular to the long axes of 8CB and CCN-47 molecules, respectively.

dipole moments exhibit antiparallel associations between pairs of molecules. The interaction becomes strongest when the dispersion energy between the aromatic cores having high polarizabilities [45, 46]. The induced dipole moment by the cyano group of 8CB of a neighbour is parallel to the permanent dipole of the cyano group of the given dipole consequently, the effective dipole moment of each molecule is enhanced as shown in Fig.6.8 (a). The chain-chain dispersion interaction energy is negligible in this case. Compounds with such strong antiparallel correlation are found to exhibit strong SmA short-range order even if there is no long-range SmA order such as in 5CB or 7CB. In fact, in case of nCB the effective molecular length is enhanced due to antiparallel correlation. CCN-47 has a strong transverse dipole moment, and a possible molecular association is shown in Fig.6.8(b). Although in this case, the effective transverse dipole moment is enhanced, the interaction is not strong as the core is made of bicyclohexane which has very low polarisability ($\Delta n \simeq 0.03$ for CCN-47, see inset of Fig.6.7(a)) compared to the biphenyl moiety. The effective molecular length is also not enhanced. In this configuration, the SmA correlation length and hence the short-range order is expected to be much smaller than that of 8CB. The antiparallel

correlation of dipoles is usually reflected in the dielectric data across the *N*-*I* phase transition. It is known that the average dielectric constant $\bar{\varepsilon}$ $(= (\varepsilon_{||} + 2\varepsilon_{\perp})/3)$ of nCB is reduced in the nematic phase below the NI phase transition in highly polar (longitudinal) compounds due to the strong antiparallel correlation of dipoles [46, 47]. For CCN-47 and its homologous series, it has been found that $\bar{\varepsilon}$ remains unchanged across the *N*-*I* transition [24, 48]. This confirms that the antiparallel association of molecules and short-range order is smaller in CCN-47 than 8CB compound.

6.4 Conclusion

The short-range smectic order in the nematic phase enhances the activation energies of translational and rotational viscosities of highly polar compounds with both longitudinal and transverse dipole moments compared to the other homologues in the respective series. The enhancement is more significant in the case of 8CB than CCN-47. Although both 8CB and CCN-47 compounds have the same dipolar group but the activation energies of rotational and translational viscosities of 8CB are much larger than that of CCN-47 due to stronger SmA short-range order in the nematic phase. Using a simple physical model we showed that the SmA short-range order due to strong antiparallel correlation of longitudinal dipole moments of 8CB molecules, which enhances both the activation energies is expected to be larger in 8CB than in CCN-47. The director excursion due to the critical slowing down of the SmA order parameter fluctuations in CCN-47 is smaller compared to the 8CB liquid crystal, consequently, the steady states are not legibly observed. Computer simulations on nematic liquid crystals made of highly polar molecules in the framework of Leslie-Ericksen formalism can shed more light on the proposed mechanism. We emphasise that ours is the first experiment among the few rheodielectric studies, probing the effect of smectic short-range order and critical slowing down of the SmA order parameter fluctuation as the *N*-SmA transition is approached in highly polar compounds with both longitudinal and transverse dipole moments. Such studies also have important relevancy in our understanding of the phase transitions in liquid crystals away from equilibrium.

References

[1] PG de Gennes, *The Physics of Liquid Crystals*, 2nd ed. (Oxford University Press, Oxford, 1993).

[2] M. Miesowicz. *The Three Coefficients of Viscosity of Anisotropic Liquids.* Nature (London). 158, 27 (1946).

[3] M. Miesowicz. *Influence of a Magnetic Field on the Viscosity of Para-Azoxyanisol.* Nature (London). 136, 261 (1935).

[4] F. M. Leslie. *Some Constitutive Equations For Anisotropic Fluids.* J. Mech. Appl. Math. 19, 357 (1966).

[5] J. L. Ericksen. *Anisotropic fluids.* Arch. Ration. Mech. Anal. 4, 231 (1959).

[6] O. Parodi. *Stress tensor for a nematic liquid crystal.* J. Phys. (Paris). 31, 581 (1970).

[7] Ch. Gahwiller. *Temperature Dependence of Flow Alignment in Nematic Liquid Crystals.* Phys. Rev. Lett. 28, 1554 (1972).

[8] T. Carlsson, and K. Skarp. *The Stabilizing Effect of an Electric Field on the Shear Flow of Nematic Liquid Crystals When* $\alpha_3 > 0$*: Flow Alignment Regained.* Mol. Cryst. Liq. Cryst. 78, 157 (1981).

[9] H. Kneppe, F. Schneider, and N. K. Sharma. *A Comparative Study of the Viscosity Coefficients of Some Nematic Liquid Crystals.* Phys. Chem. 85, 784 (1981).

[10] F. J. Bock, H. Kneppe, and F. Schneider. *Rotational viscosity of nematic liquid crystals and their shear viscosity under flow alignment.* Liq. Cryst. 1, 239 (1986).

[11] A. G. Chmielewski. *Viscosity Coefficients of Some Nematic Liquid Crystals.* Mol. Cryst. Liq. Cryst. 132, 339 (1986).

[12] W. W. Beens, and W. H. de Jeu. *The flow alignment of some nematic liquid crystals.* J. Chem. Phys. 82, 3841 (1985).

[13] M. L. Dark, M. H. Moore, D. K. Shenoy, and R. Shashidhar. *Rotational viscosity and molecular structure of nematic liquid crystals.* Liq. Cryst. 33, 67 (2006).

[14] V. V. Belyaev, *Viscosity of Nematic Liquid Crystals.* 1st Indian ed. (Cambridge International Science Publishing, Cambridge, 2011).

[15] W. H. de Jeu, *Physical Properties of Liquid Crystal Materials.* (Gordon and Breach, New York, 1980).

[16] C. R. Safinya, E. B. Sirota, and R. J. Plano. *Nematic to smectic-A phase transition under shear flow: A nonequilibrium synchrotron X-ray study.* Phys. Rev. Lett. 66, 1986 (1991).

[17] R. F. Bruinsma, and C. R. Safinya. *Landau theory of the nematic–smectic-A phase transition under shear flow.* Phys. Rev. A. 43, 5377 (1991).

[18] W. H. Han, and A. D. Rey. *Simulation and validation of nonplanar nematorheology.* J. Rheol. 38, 1317 (1994).

[19] W. H. Han, and A. D. Rey. *Simulation and validation of temperature effects on the nematorheology of aligning and nonaligning liquid crystals.* J. Rheol. 39, 301 (1995).

[20] K. Negita, M. Inoue, and S. Kondo. *Dielectric study on the shear-induced structural changes in the nematic and the smectic-A phases of* 4-*n*-octyl-4′-cyanobiphenyl *(8CB).* Phys. Rev. E. 74, 051708 (2006).

[21] J. Ananthaiah, M. Rajeswari, V. S. S. Sastry, R. Dabrowski, and S. Dhara. *Effect of electric field on the rheological and dielectric properties of a liquid crystal exhibiting nematic-to-smectic-A phase transition.* Eur. Phys. J. E. 34, 74 (2011).

[22] J. Ananthaiah, R. Sahoo, N. V. Rasna and S. Dhara. *Rheology of nematic liquid crystals with highly polar molecules.* Phys. Rev. E. 89, 022510 (2014).

[23] D. V. Sai, K. P. Zuhail, R. Sarkar and S. Dhara. *Structure–property correlation of bicyclohexane nematic liquid crystals.* Liq. Cryst. 42, 328 (2015).

[24] S. Dhara and N. V. Madhusudana. *Physical characterisation of* $4'$*-butyl-4-heptyl-bicyclohexyl-4-carbonitrile.* Phase Trans. 81, 561 (2008).

[25] S. Dhara and N. V. Madhusudana. *Influence of director fluctuations on the electric-field phase diagrams of nematic liquid crystals.* Euro. Phys. Lett. 67, 411 (2004).

[26] S. Dhara and N. V. Madhusudana. *Enhancement of the orientational order parameter of nematic liquid crystals in thin cells.* Euro. Phys. J. E. 13, 401 (2004).

[27] R. Sahoo, O. Chojnowska, R. Dabrowski and S. Dhara. *Experimental studies on the rheology of cubic blue phases.* Soft Matter. 12, 1324 (2016).

[28] R. Sahoo, J. Ananthaiah, R. Dabrowski and S. Dhara. *Rheology of twist-grain-boundary- A liquid crystals.* Phys. Rev. E. 90, 012506 (2014).

[29] R. Sahoo and S. Dhara. *Rheological studies on liquid-crystal colloids prepared by dispersing spherical microparticles with homeotropic surface anchoring.* Liq. Cryst. 44, 1582 (2017).

[30] J. Ananthaiah, M. Rajeswari, V. S. S. Sastry, R. Dabrowski, and S. Dhara. *Rheological properties of a reentrant nematic liquid crystal.* Phys. Rev. E. 86, 011710 (2012).

[31] S. T. Wu and C. S. Wu. *Experimental confirmation of the Osipov-Terentjev theory on the viscosity of nematic liquid crystals.* Phys. Rev. A. 42, 2219 (1990).

[32] S. Dhara, J. K. Kim, S. M. Jeong, R. Kogo, F. Araoka, K. Ishikawa, and H. Takezoe. *Anchoring transitions of transversely polar liquid-crystal molecules on perfluoropolymer surfaces.* Phys. Rev. E. 79, 060701(R) (2009).

[33] M. V. Rasna, R. Manda, P. Paik, W. Haase, and S. Dhara. *Discontinuous anchoring transition and photothermal switching in composites of liquid crystals and conducting polymer nanofibers.* Phys. Rev. E. 89, 052503 (2014).

[34] T. Arun Kumar, P. Sathyanarayana, V. S. S. Sastry, H. Takezoe, N. V. Madhusudana, and S. Dhara. *Temperature- and electric-field-induced inverse Freedericksz transition in a nematogen with weak surface anchoring.* Phys. Rev. E. 82, 011701 (2010).

[35] D.V. Sai, T. Arun Kumar, W. Hasse, A. Roy and S. Dhara. *Effect of smectic short-range order on the discontinuous anchoring transition in nematic liquid crystals.* J. Chem. Phys. 141, 044706 (2014).

[36] S. Aya and F. Araoka. *Anomalous temperature-dependent anchoring in liquid crystals mediated by thermodynamic smectic wetting sheets.* Appl. Phys. Lett. 111, 201604 (2017).

[37] S. Aya, Y. Sasaki, H. Takezoe, K. Ishikawa, K. Ema, T. Hikima, M. Takata and F. Araoka. *Thermodynamically Anchoring-Frustrated Surface to Trigger Bulk Discontinuous Orientational Transition.* Langmuir. 32, 10545 (2016).

[38] P. G de Gennes. *An analogy between superconductors and smectics A.* Solid State Commun. 10, 753 (1972).

[39] S. W. Morris, P. Palffy and D.A. Balzarini. *Measurements of the Bend and Splay Elastic Constants of Octyl-Cyanobiphenyl.* Mol. Cryst. Liq. Cryst. 139, 263 (1986).

[40] K. P. Zuhail, P. Sathyanarayana, D. Seč, S. Čopar, M. Škarabot, I. Muševič, and S. Dhara. *Topological defect transformation and structural transition of two-dimensional colloidal crystals across the nematic to smectic-A phase transition* Phys. Rev. E. 91, 030501(R) (2015).

[41] S. Dasgupta, P. Chattopadhyay, and S. K. Roy. *Effect of a rigid nonpolar solute on the splay, bend elastic constants, and on rotational viscosity coefficient of* $4, 4' -$ n $-$ octyl $-$ cyanobiphenyl. Phys. Rev. E. 63, 041703 (2001).

[42] P. Oswald, G. Poy, F. Vittoz and V. Popa-Nita. *Experimental relationship between surface and bulk rotational viscosities in nematic liquid crystals.* Liq. Cryst. 40, 734 (2013).

[43] F. Jahnig and F. Brochard. *Critical elastic constants and viscosities above a nematic-smectic a transition of second order.* J. Phys. (Paris). 35, 301 (1974).

[44] R. G. Larson. *The Structure and Rheology of Complex Fluids*, Oxford University Press, New York (1999).

[45] N. V. Madhusudana, B. S. Srikanta and M. Subramanya Raj. *Comparative X-ray and Dielectric studies on some structurally related smectogenic compounds.* Mol. Cryst. Liq. Cryst. 108, 19 (1984).

[46] N. V. Madhusudana and S. Chandrasekhar. Proceedings of the International Liquid Crystals Conference, Bangalore, December, Pramana Supplement. 1, 57 (1973).

[47] M. Schadt. *Dielectric properties of some nematic liquid crystals with strong positive dielectric anisotropy.* J. Chem. Phys. 56, 1494 (1972).

[48] I. H. Ibrahim and W. Haase. *On the Molecular Polarizability of Nematic Liquid Crystals.* Mol. Cryst. Liq. Cryst. 66, 189 (1981).

Conclusion and Future scope

In the recent past, two new nematic liquid crystals, namely, twist-bend and splay nematic were discovered. It has created immense interest because of its potential applications and intriguing fundamental science. The splay nematic was later identified as a ferroelectric nematic liquid crystal which was envisaged by Max Born almost a century ago. These nematics have much lower symmetries than conventional nematic crystals made of rod-like molecules. Although several structural and physical studies have been reported, the rheological properties of these new phases were unexplored.

In this thesis, in chapters-3 and 4, we have mainly investigated the rheological properties of two new nematic liquid crystals. We showed that the flow properties of the twist-bend nematic LC are more like usual smectic-A liquid crystals. It means the pseudolayers (i.e., the layers without true mas density wave) respond similar way to true smectic layers. Using a simplified model, we estimated the temperature-dependence layer compressional elastic modulus of the pseudolayers which agrees well with the recent prediction of the coarse-grained model. The twist-bend phase's shear-induced dynamics are remarkably different from the conventional nematic of small molecules. Depending on the shear rate and temperature it shows three distinct flow regimes. In the intermediate regime, it shows periodic and quasi-periodic stress oscillations which are somewhat similar to those reported in warm-like micellar systems.

In chapter-5, we have investigated electrorheological properties of a ferroelectric nematic liquid crystal. We showed that the viscoelastic coefficient is two orders of magnitude larger than conventional nematics. This large value of the coefficient is due to the formation of polar domains, which grow as the nematic to polar nematic transition temperature is approached. The gigantic electroviscous effects demonstrated here are useful for emerging applications and understanding striking electrohydrome-

chanical effects in ferroelectric nematic liquid crystals. In the last chapter, we have shown that the activation energies of the shear and rotational viscosities of highly polar compounds exhibiting N-SmA phase transition are larger than those compounds without N-SmA transition. We demonstrated the effect of smectic short-range order fluctuations on both shear and rotational viscosities for the first time.

This thesis, for the first time, reports some interesting rheological properties of the twist-bend and ferroelectric nematic liquid crystals. We believe there are several scopes for further studies of these materials. For example, the origin of the stress fluctuations in the plateau region in chapter-4 is still unclear. The dynamical textural change under shear can be seen through rheomicroscopic investigations but for that, the transition temperatures should be reduced. In the case of ferroelectric nematic liquid crystal, it is important to ask and understand how the flow and the polarization are coupled. A modified Leslie-Ericksen theory may be needed to understand the details of the shear response.

Publications

Publications related to thesis

1. Effect of Sm-A short-range order on the activation energies of translational and rotational viscosities of nematic liquid crystals with highly polar molecules.
   M. Praveen Kumar, D. Venkata Sai and Surajit Dhara.
   Phys. Rev. E 98, 062701 (2018).
   DOI: 10.1103/PhysRevE.98.062701

2. Smectic like rheology and pseudolayer compression elastic constant of a twist-bend nematic liquid crystal.
   M. Praveen Kumar, P. Kula and Surajit Dhara.
   Phys. Rev. Materials 4, 115601 (2020).
   DOI: 10.1103/PhysRevMaterials.4.115601

3. Dynamics of a sheared twist-bend nematic liquid crystal.
   M. Praveen Kumar, J. Karcz, P. Kula and Surajit Dhara.
   Phys. Rev. Materials 5, 115605 (2021).
   DOI: 10.1103/PhysRevMaterials.5.115605

4. Giant electroviscous effects in a ferroelectric nematic liquid crystal.
   M. Praveen Kumar, J. Karcz, P. Kula, S. Karmakar and Surajit Dhara.
   Phys. Rev. Applied 19, 044082 (2023).
   DOI: 10.1103/PhysRevApplied.19.044082

Other Publications

1. Hierarchical self-assembly of colloidal nanoplatelets driven by evaporation.
   Ravi Kumar Pujala, **M. Praveen Kumar** and Surajit Dhara.
   J. Phys. D: Appl. Phys. 51, 304003 (2018).
   DOI: 10.1088/1361-6463/aacacd

2. Re-entrant direct hexagonal phases in a lyotropic system of surfactant induced by an ionic liquid.
   S. Mitra, R. Karri, **M. Praveen Kumar**, A. B. Dey, G. Bhattacharya, G. Roy, S. M. Kamil, Surajit Dhara, S. K. Sinha and S. K. Ghosh
   Liquid Crystals 46, 1327 (2019).
   DOI: 10.1080/02678292.2019.1566507

3. Rheological studies on homogeneous and inhomogeneous core dense colloidal PNIPAM microgels.
   B. V. R. Tata, M. V. Saisavadas, R. G. Joshi, **M. Praveen Kumar** and Surajit Dhara
   AIP Conference Proceedings 2269, 060001 (2020).
   DOI: 10.1063/5.0019582

Workshops/Conferences attended

1. Attended **"Soft and Active matter"** workshop conducted by School of Physics, University of Hyderabad on 11-17 February, 2018.

2. Attended 25th National Conference on Liquid Crystals (NCLC-2018) and presented a **poster** entitled "Effect of Sm-A short-range order on the activation energies of rotational and translational viscosities of nematic liquid crystals with highly polar molecules" held at Prayagraj, Uttar Pradesh and got **Best Poster Award**.

3. Attended International Complex Fluids Conference (CompFlu-2019) and presented a **poster** entitled "Rheological properties of twist bend nematic liquid crystals" held at IISER Bhopal, India.

4. Attended 27^{th} National Conference on Liquid Crystals (NCLC-2020 (online)) and presented an **oral talk** entitled "Smectic-like rheology and pseudo-layer compression elastic constant."

5. Attended International Complex Fluids Conference (CompFlu-2020 (online)) and presented a **poster/flash Talk** entitled "Smectic–like rheology and pseudolayer compression elastic constant."

6. Attended International Conference on Soft Materials (ICSM-2020 (online)) and presented an **oral talk** on "Smectic-like rheology and pseudo-layer compression elastic constant of a twist-bend nematic liquid crystal."

7. Attended 28^{th} National Conference on Liquid Crystals (NCLC-2021 (online)) and presented a **poster/flash talk** on "Dynamics of sheared twist bend nematic liquid crystal" held at Assam University, Silchar, India and got **Best Poster Award**.

8. Attended Frontiers in Physics (FIP-2023) conducted by School of physics, University of Hyderabad, India and presented an **oral talk** on "Giant electroviscous effects in a ferroelectric nematic liquid crystal."

Rheology of twist-bend and ferroelectric nematic liquid crystals

by M Praveen Kumar

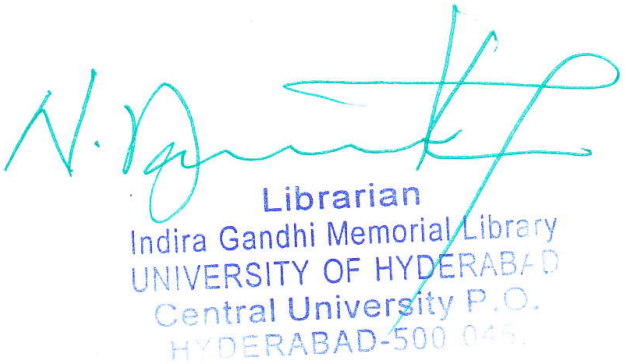

Submission date: 22-May-2023 05:07PM (UTC+0530)
Submission ID: 2099161303
File name: M_Praveen_Kumar.pdf (38.67M)
Word count: 22015
Character count: 109838

Rheology of twist-bend and ferroelectric nematic liquid crystals

ORIGINALITY REPORT

58%	10%	57%	3%
SIMILARITY INDEX	INTERNET SOURCES	PUBLICATIONS	STUDENT PAPERS

PRIMARY SOURCES

1	M. Praveen Kumar, D. Venkata Sai, Surajit Dhara. " Effect of Sm- short-range order on the activation energies of translational and rotational viscosities of nematic liquid crystals with highly polar molecules ", Physical Review E, 2018 Publication	15%
2	M. Praveen Kumar, Jakub Karcz, Przemyslaw Kula, Smarajit Karmakar, Surajit Dhara. "Giant Electroviscous Effects in a Ferroelectric Nematic Liquid Crystal", Physical Review Applied, 2023 Publication	13%
3	M. Praveen Kumar, Jakub Karcz, Przemyslaw Kula, Surajit Dhara. "Dynamics of a sheared twist-bend nematic liquid crystal", Physical Review Materials, 2021 Publication	11%
4	M. Praveen Kumar, P. Kula, Surajit Dhara. "Smecticlike rheology and pseudolayer compression elastic constant of a twist-bend	11%

nematic liquid crystal", Physical Review Materials, 2020
Publication

5	Submitted to University of Hyderabad, Hyderabad Student Paper	1 %
6	D. Demus, J. Goodby, G. W. Gray, H. - W. Spiess, V. Vill. "Handbook of Liquid Crystals Set", Wiley, 1998 Publication	1 %
7	ftp.aip.org Internet Source	1 %
8	Deng - Ke Yang, Shin - Tson Wu. "Fundamentals of Liquid Crystal Devices", Wiley, 2014 Publication	<1 %
9	www.researchgate.net Internet Source	<1 %
10	link.springer.com Internet Source	<1 %
11	Andrei A. Sonin. "Pierre-Gilles de Gennes and physics of liquid crystals", Liquid Crystals Reviews, 2018 Publication	<1 %
12	pubs.rsc.org Internet Source	<1 %

13	docksci.com Internet Source	<1 %
14	Nerea Sebastián, Martin Čopič, Alenka Mertelj. "Ferroelectric nematic liquid-crystalline phases", Physical Review E, 2022 Publication	<1 %
15	www.azom.com Internet Source	<1 %
16	www.nature.com Internet Source	<1 %
17	utpedia.utp.edu.my Internet Source	<1 %
18	Submitted to University of Bradford Student Paper	<1 %
19	NATO ASI Series, 1992. Publication	<1 %
20	flc2021.ijs.si Internet Source	<1 %
21	libstore.ugent.be Internet Source	<1 %
22	Broadband Dielectric Spectroscopy, 2003. Publication	<1 %
23	dspace.mit.edu Internet Source	<1 %

24	epdf.pub Internet Source	<1 %
25	Soft and Biological Matter, 2016. Publication	<1 %
26	V. R. Basker, David W. Martyny, Arthur L. Fricke, Oscar D. Crisalle. "Viscometers", Wiley, 1999 Publication	<1 %
27	wiki.anton-paar.com Internet Source	<1 %
28	J. Ananthaiah, M. Rajeswari, V. S. S. Sastry, R. Dabrowski, Surajit Dhara. "Rheological properties of a reentrant nematic liquid crystal", Physical Review E, 2012 Publication	<1 %
29	Submitted to Texas A&M University, College Station Student Paper	<1 %
30	onlinelibrary.wiley.com Internet Source	<1 %
31	Submitted to IIT Delhi Student Paper	<1 %
32	David Dunmur. "Liquid Crystals", Springer Handbook of Electronic and Photonic Materials, 2006 Publication	<1 %

33	Ken - Ichi Izumi, Toshihiko Nagamura, Hirotsugu Kikuchi. "Light diffraction studies on director arrangement in the polymer - pinned striped pattern obtained via the electric field - induced Fréedericksz transition of nematics", Liquid Crystals, 2006 Publication	<1 %
34	Massimiliano Grosso, Pier Luca. "Chapter 14 Fourier Transform Rheology: A New Tool to Characterize Material Properties", IntechOpen, 2011 Publication	<1 %
35	main.tu-jo.com Internet Source	<1 %
36	John M. Dealy, Kurt F. Wissbrun. "Melt Rheology and Its Role in Plastics Processing", Springer Nature, 1990 Publication	<1 %
37	espace.etsmtl.ca Internet Source	<1 %
38	F. Buiochi. "P3L-3 Viscosity Measurement of Newtonian Liquids Using The Complex Reflection Coefficient", 2006 IEEE Ultrasonics Symposium, 10/2006 Publication	<1 %
39	S. Chandrasekhar, N. V. Madhusudana. "Spectroscopy of Liquid Crystals", Applied	<1 %

	Spectroscopy Reviews, 1972 Publication	
40	api-depositonce.tu-berlin.de Internet Source	<1 %
41	pub.uni-bielefeld.de Internet Source	<1 %
42	Submitted to Indian Institute of Science, Bangalore Student Paper	<1 %
43	Submitted to North Eastern Regional Institute of Science and Technology Student Paper	<1 %
44	Urbicain, Martin, and Jorge Lozano. "Thermal and Rheological Properties of Foodstuffs", Handbook of Food Engineering Practice, 1997. Publication	<1 %
45	Abinash Barthakur, Jakub Karcz, Przemyslaw Kula, Surajit Dhara. "Critical splay fluctuations and colossal flexoelectric effect above the nonpolar to polar nematic phase transition", Physical Review Materials, 2023 Publication	<1 %

Exclude quotes	On	Exclude matches	< 14 words
Exclude bibliography	On		

Plagiarism-free statement

This is to certify that the thesis entitled "Rheology of twist-bend and ferroelectric nematic liquid crystals" has been screened by the Turnitin software at the Indira Gandhi Memorial Library of the University of Hyderabad. The software shows a 58% similarity index, of which 50% came from the candidate's own four research articles related to this thesis, which are already published and available online. Thus, the effective similarity index excluding his research articles is 58%-50% = 8%, which is lower than the 10% stipulated by the University guidelines. Therefore, the thesis is free from plagiarism

S Dhara

Prof. Surajit Dhara

Thesis Supervisor

School of Physics

University of Hyderabad

Date: 23/5/23

Dr. Surajit Dhara
Professor
School of Physics
University of Hyderabad
Hyderabad-500 046, INDIA.